Models of Magnetohydrodynamic Flow Instabilities with Applications to the Solar Atmosphere

Mihai Barbulescu

Professor Róbert Erdélyi,
Professor Michael S. Ruderman

University of Sheffield
School of Mathematics and Statistics

A thesis submitted in partial fulfilment of the requirements for the degree of

Doctor of Philosophy

July 2018

To Brîndușa

Acknowledgements

I would like to offer my thanks to the various people and institutions that have made the successful completion of this thesis possible.

First and foremost, I would like to thank my two supervisors, Professors Róbert Erdélyi and Michael S. Ruderman, for the guidance and insight they offered me throughout my PhD. I would also like to thank Professor Tom Van Doorsselaere for his contributions to the project that became Chapter 3 of this thesis, and for being a gracious host during my visit to KU Leuven.

I am deeply indebted to my partner, Brîndușa, who shared my enthusiasm about science and supported me through the most difficult parts of my PhD. You shared my highs and my lows, you gave me hope and things to look forward to. For this, and so much more, I dedicate this thesis to you.

I am equally indebted to my family, for their love and support through the years. Without you, none of this would have been possible.

I'd like to thank my friends and colleagues for all the help they gave me throughout my degree. Stevie, Freddie, Matt and Ellie for being there when the maths was confusing. Chris, Rahul, Norbi and Tamas for explaining time and again how the Sun works. Ben and Fin for introducing me to the fascinating world of MHD simulations. Stuart and Drew for all your help with coding. Thank you all.

I'd also like to thank my close friends (some of you again) for making the past few years a lovely experience. Thank you Ellie, Ben, Freddie, Hope, Alex, Comi and Reza, for letting me be a part of your lives and for putting up with my antics for so long. To the rest of my friends not mentioned here, I appreciate you all.

In order to give credit where credit is due, I offer my thanks to all the staff of Interval, The University Arms, The Washington, and all other establishments that I frequented throughout my PhD. Your service turned good times great and made bad times bearable.

Finally, I acknowledge the funding received from the UK's Science and Technologies Facilities Council (STFC) and the EU's Erasmus Programme that allowed me to undertake this degree.

Declaration of Authorship

I hereby declare that except where specific reference is made to the work of others, the contents of this dissertation are original and have not been submitted in whole or in part for consideration for any other degree or qualification in this, or any other university. This dissertation is my own work and contains nothing which is the outcome of work done in collaboration with others, except as specified in the text and Acknowledgements. This dissertation contains fewer than 80,000 words including appendices, bibliography, footnotes, tables and equations.

Mihai Barbulescu
July 2018

Abstract

Magnetoacoustic waves are ubiquitous in the solar atmosphere. The properties of their propagation, as well as the possibility that they may trigger magnetohydrodynamic instabilities must have a strong theoretical interpretation in order to better our understanding of solar phenomena. In this Thesis, we develop two new models of magnetoacoustic wave propagation and we study the conditions for the triggering of the Kelvin-Helmholtz instability in each case.

List of Publications

This Thesis is based on the following publications:

- Barbulescu, M., Erdélyi, R. (2018); Magnetoacoustic Waves and the Kelvin-Helmholtz Instability in a Steady Asymmetric Slab. I: The Effects of Varying Density Ratios, *Solar Phys.*, Volume 293, Issue 6
- Barbulescu, M., Ruderman, M.S., Van Doorsselaere, T., Erdélyi, R.; An Analytical Model of the Kelvin-Helmholtz Instability of Transverse Coronal Loop Oscillations, *Astrophys. J.*, submitted.

The following publication is not included in this Thesis:

- Barbulescu, M., Erdélyi, R. (2016); Propagation of Long-Wavelength Nonlinear Slow Sausage Waves in Stratified Magnetic Flux Tubes, *Solar Phys.*, Volume 291, Issue 5

Contents

List of Figures

CHAPTER 1

Introduction

1.1 Overview

The Sun has been an object of fascination and study for most of humanity's recorded history. It is the main source of energy and accounts for most of the mass in the solar system. The history of the Sun began approximately 4.6 billions years ago, with the gravitational collapse of a section of a massive molecular cloud (Bouvier and Wadhwa, 2010). This collapse created a protoplanetary disk with a protostar at its centre (Montmerle et al., 2006). The protostar was composed of hydrogen, helium and lithium, which together accounted for around 98% of its mass, while the other 2% were heavier elements formed in younger generations of stars (Zeilik and Gregory, 1998). For approximately 50 million years after the formation of the protostar, it underwent a slow contraction which increased the temperature and pressure at its core, until it was able to start fusing hydrogen (Yi et al., 2001). At that point the Sun became a main sequence star, which it will remain for at least another 5 billion years before becoming a red giant (Schröder and Connon Smith, 2008). It will subsequently become a red giant, and then a white dwarf, after having ejected nearly half of its mass (Schröder and Connon Smith, 2008). The ejected mass will form a planetary nebula, while the white dwarf will survive and may eventually become a hypothetical black dwarf (Bloecker, 1995).

The history of solar observations dates back to records of eclipses by Chinese astronomers as early as the year 2000 BCE (Priest, 2014). *Sunspots*, which are areas on the Sun's photosphere that are darker and cooler than their surroundings, have been recorded since at least 800 BCE by the Chinese, and 300 BCE by the ancient Greeks. The first mention of the *corona*, the high temperature atmosphere of the Sun, is attributed to the Byzantine scholar Leo Diaconus, as he observed the total eclipse of 22 December 968 from Constantinople, although people might have been aware of it as early as

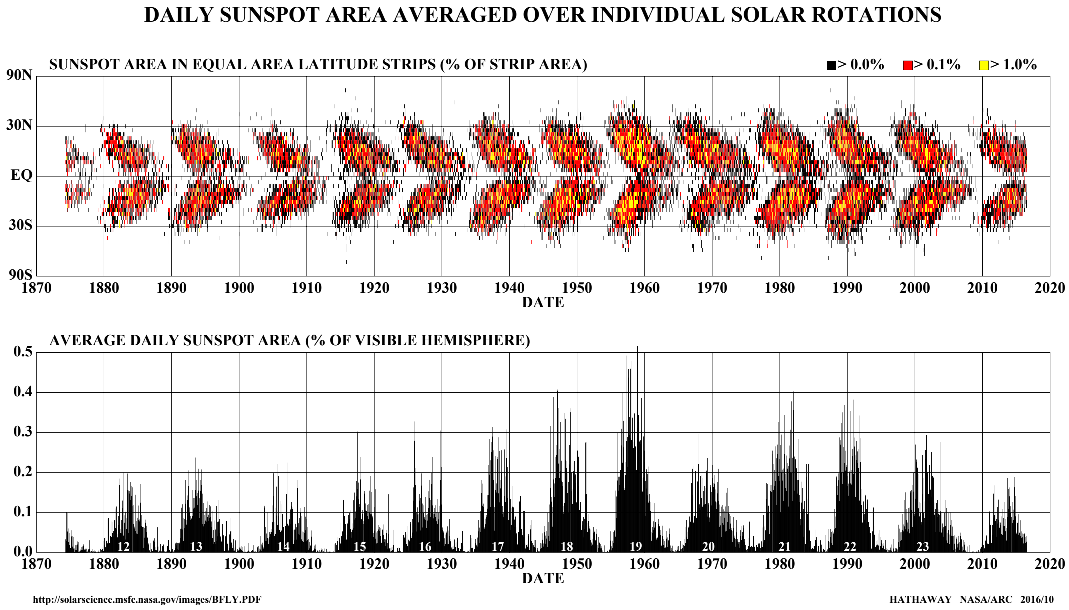

Figure 1.1: The so-called *butterfly diagram*, displaying the distribution of sunspots across latitudes over time. Sunspots are most commonly found further from the equator at the beginning of the 11 year cycle, and closer to the equator near its end. Credit: NASA Marshall Space Flight Center

the time of Plutarch. Solar *prominences* were first described in the Russian First Chronicle of Novgorod as “live embers” coming out of the Sun during the 1 May 1185 eclipse. For a detailed account of pre-telescope astronomy, see Hetherington (1996).

The advent of modern physics and astronomy led to great advances in solar physics in the past two centuries. Some of the important discoveries that occurred during the 19th century include the first description of the Sun’s spectral lines by Fraunhofer, the discovery of the 11 year sunspot cycle by Schwabe (see Figure 1.1), and the first observations of solar flares and spicules by Carrington and Secchi, respectively. The pace of discovery accelerated during the 20th century, as new instruments, such as the coronagraph, were created, and the theory of *magnetohydrodynamics* (MHD), which is used to describe many solar phenomena, was established. Other important discoveries include the first description of the solar wind (Parker, 1958) and the first observations of coronal mass ejections (CMEs). Finally, our modern view of the Sun has been shaped by the multitude of solar missions that have become operational since the 1990s, such as Yohkoh, TRACE and SDO. For a more detailed view of recent advances in solar physics, see, for example, Aschwanden (2004); Priest (2014).

1.2 Structure and Physical Properties of the Sun

The Sun is a highly inhomogeneous nearly perfect sphere of plasma. Its mean radius has been measured as being $R_\odot = 695.66$ Mm (Haberreiter et al., 2008), although the International Astronomical Union defines the nominal solar radius as $R_\odot^N = 695.7$ Mm (Mamajek et al., 2015). It has a mass of 1.99×10^{30} kg and loses around $1 - 1.5 \times 10^9$ $\mathrm{kg\,s^{-1}}$ due to the solar wind (Parker, 1958; Priest, 2014). The Sun is composed primarily of hydrogen (over 70% of the solar mass), and helium (around 27% of the solar mass), with only trace amounts of other elements, such as oxygen, carbon or nitrogen (Lodders, 2003). The mean distance between the Sun and the Earth is one astronomical unit, defined as 1 au = 149 597 870 700 m, or approximately 150×10^6 km (Capitaine et al., 2012).

In the following Subsections, we shall discuss the structure and physical properties of both the hidden solar interior, and of the visible atmosphere. According to the latest models, the solar interior consists of four regions: the core, the radiative zone, the tachocline, and the convective zone, listed here from the innermost to the outermost. The solar atmosphere is composed of the photosphere, chromosphere and corona. While the solar atmosphere is observable with optical telescopes, due to the high density of solar plasma beneath the photosphere, the solar interior is opaque. Our current knowledge of the interior is obtained through the mathematical models of helioseismology.

All of the structure described above, as well as some other phenomena that will be discussed later, has been visualised in Figure 1.2. The majority of the current section has been adapted from Priest (2014), and should be considered a reference, unless a different reference is stated.

1.2.1 The Solar Interior

The *solar core* extends from the center of the Sun to approximately 0.25 solar radii. Its temperature is of the order of 15 million K, and its density around 1.6×10^5 $\mathrm{kg\,m^{-3}}$, which is enough to enable nuclear fusion. The core contains approximately half the mass of the Sun in only 1/50 of its volume, and produces 99% of its energy. Most of this energy comes from two sets of fusion reactions: the proton-proton chain reaction and the CNO (carbon-nitrogen-oxygen) cycle. Both of these reactions have the same outcome: four protons (^{1}H) become fused into one helium-4 nucleus (^{4}He), while other atoms only act as catalysts. As a

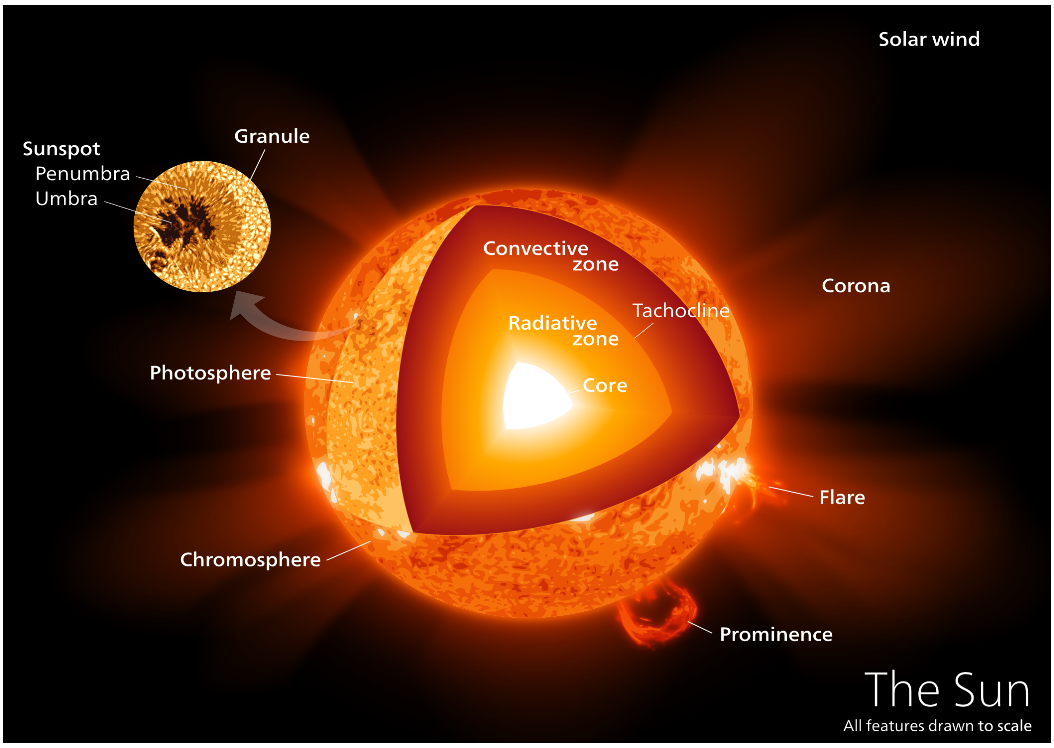

Figure 1.2: The structure of the Sun. The core, radiative zone, tachocline and convective zone form the opaque inner layers, while the photosphere, chromosphere and corona form the observable atmosphere. Various observable phenomena, including a flare, prominence and photospheric granulation are also presented. Adapted from Wikipedia.

result of the process of fusion, some of the mass is converted into energy, and escapes in the form of high-energy γ-rays and also electron neutrinos.

The *radiative zone* is the layer directly above the core, and extends from approximately $0.25R_\odot$ to $0.7R_\odot$. The plasma composing this layer is opaque enough that the mean free path of photons travelling through it is of the order of 10^{-4} m. If not for this opacity, photons would only take 2 s to cross the radiative zone, but instead they perform a random walk which lengthens their journey to 170 000 years. The numerous collisions that photons experience during this time have a major effect, that of increasing the wavelength of the high-energy γ-rays emerging from the core, to visible light at the solar surface.

In contrast to the radiative zone where energy is transported via radiative diffusion and thermal conduction, in the *convective zone* the convective instability is the main source of energy transport. These two sections are separated by a thin shear layer, called the *tachocline* (Spiegel and Zahn, 1992), which is likely significant in the generation of the global solar magnetic field. The convective zone is the last of the interior layers and extends from around $0.7R_\odot$

to $1R_\odot$.

1.2.2 The Solar Atmosphere

The solar atmosphere may be divided into four regions which have different physical characteristics (see Figure 1.2). The lowest of these, the *photosphere*, is the Sun's surface layer and is only around 500 km thick. It is where most of the Sun's visible light is emitted. Most of the photosphere is composed of granules with hot bright centres of rising plasma and cool dark boundaries. This granulation is caused by turbulent convective motion lifting hot plasma, which subsequently cools and falls, forming the granular boundaries, called intergranular lanes. Regions of strong magnetic flux may inhibit this convection, and form sunspots. Granules have diameters ranging from 0.3 to 2 Mm, and lifetimes of 1 to 20 minutes, with typical values of 5 to 8 minutes (Priest, 2014).

The *chromosphere* extends over the photosphere and exhibits various forms of structuring. The most common of these are spicules, which are dynamic jets that cover the solar surface and form a sort of canopy.

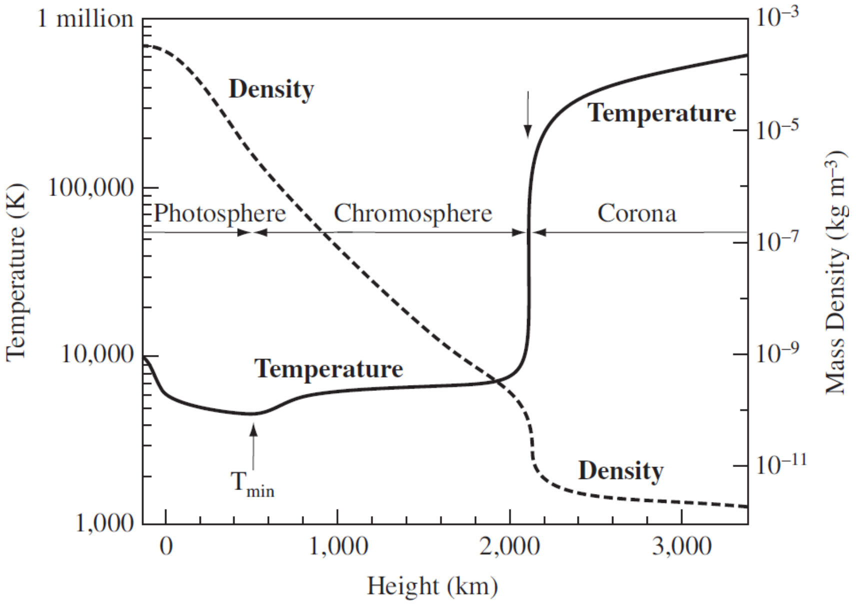

Figure 1.3: The mean variation of the density and temperature, as described by the VAL model. Image credit: Avrett and Loeser (2008).

The *corona* is the outermost regions of the Sun's atmosphere, separated from the chromosphere by a narrow *transition region*, and extends outwards into the solar wind. Significant structuring is present in the corona due to the intense magnetic fields that permeate it. Of particular interest in this Thesis are *coronal loops*. They are a common form of structuring, comprising of hot plasma (2 to 3 MK) frozen into the magnetic fields tied to the photosphere. Coronal loops are waveguides for MHD waves of various modes, an aspect which we examine in Chapter 3 of this Thesis. Other structures in the corona include coronal holes, X-ray bright points, and coronal streamers.

Coronal mass ejections are large-scale releases of solar plasma from the corona, often following solar flares or prominence eruptions. Their bulk speeds take a wide range of values, from less than 100 $\mathrm{km\,s^{-1}}$ to over 2000 $\mathrm{km\,s^{-1}}$. They account for approximately 5 to 10 per cent of the solar wind mass-loss. It is shown in Chapter 2 that the high bulk speed of CMEs makes them particularly prone to the Kelvin-Helmholtz instability.

The mean temperatures and densities of the regions introduced above are commonly described using the VAL (Vernazza-Avrett-Loeset) model (Vernazza et al., 1981; Avrett and Loeser, 2008). According to this model, the density suffers a decrease from approximately 10^{-4} $\mathrm{kg\,m^{-3}}$ at the base of the photosphere to around 10^{-10} $\mathrm{kg\,m^{-3}}$ at the transition region, and then falls steeply to almost 10^{-12} $\mathrm{kg\,m^{-3}}$ in the corona. The temperature also rises dramatically across the transition region, from a chromospheric value of 25 000 to over 1 MK in the corona. The mechanisms that cause this abrupt increase in temperature are still not well understood, and are a topic of ongoing study.

1.3 Equations of Magnetohydrodynamics

In Section 1.2 we described some of the main physical properties of the Sun, gave an overview of its large- and small-scale structure, and introduced a number of solar phenomena. In order to mathematically model this phenomena, we need to employ a suitable framework. Due to the fact that, in this Thesis, we are mainly concerned with phenomena in the corona, we considered the most appropriate framework the equations of *ideal magnetohydrodynamics* (MHD).

In this Section, we give a brief description of how the ideal MHD equations are obtained, and we motivate their use in modelling coronal phenomena. The MHD equations may be obtained using two different methods:

- Averaging the kinetic equations for plasmas;
- Combining Maxwell's equations for electric and magnetic fields with the fluid equations.

The first of these methods is mathematically more complicated and shall be omitted in this section. However, the relevant derivation may be found in classical works such as Braginskii (1965) or Chapman and Cowling (1970), or more modern introductions to MHD, such as Goossens (2003) or Goedbloed and Poedts (2004).

For the second, we require the equations of Maxwell, that describe the evolution of the electric field, $\mathbf{E}(\mathbf{r}, t)$ (measured in $\mathrm{V\,m^{-1}}$), and magnetic field $\mathbf{B}(\mathbf{r}, t)$ (measured in T), in response to the current density $\mathbf{j}(\mathbf{r}, t)$ (measured in $\mathrm{A\,m^{-2}}$) and the total electric charge density $\tau(\mathbf{r}, t)$ (measured in $\mathrm{C\,m^{-3}}$). Additionally, we require the equations of conservation of momentum, mass, and energy, which govern the dynamical evolution of the density, $\rho(\mathbf{r}, t)$ (measured in $\mathrm{kg\,m^{-3}}$), pressure $p(\mathbf{r}, t)$ (measured in $\mathrm{N\,m^{-2}}$), and velocity, $\mathbf{v}(\mathbf{r}, t)$ (measured in $\mathrm{m\,s^{-1}}$), of a fluid. Here, $\mathbf{r}$ is the position vector, and t is time (measured in s).

After making a number of simplifying assumptions, we combine these two systems of equations in order to eliminate, $\mathbf{E}, \mathbf{j}$, and τ, and obtain a system of coupled equations in terms of $\mathbf{v}, \mathbf{B}, \rho$, and p.

1.3.1 Assumptions of Ideal MHD

The MHD equations describe the macroscopic dynamics of magnetised plasmas. As such, we need to establish under what conditions kinetic effects, i.e. small scale effects, stop becoming significant, and the plasma may be treated as a bulk fluid. This Subsection is based on Goedbloed and Poedts (2004) and Priest (2014).

We begin by assuming that the model plasma is *electrically neutral*, which is true for most applications in the solar photosphere and corona. We define the number densities of positive and negative particles per unit volume, n_+ and n_-, respectively, and the total number density per unit volume, n. It follows that, for charge neutrality, we require $|n_+ - n_-| \ll n$. The absence of charge neutrality is called a *charge imbalance*, and such an imbalance produces an electric field with a spatial range of the *Debye length* (see, for example, Boyd and Sanderson, 2003),

$$\lambda_D = \sqrt{\frac{\varepsilon_0 k_B T}{nq}}. \tag{1.1}$$

The quantities in Equation (1.1) are defined as follows. The electric constant,

ε_0, also called the permittivity of free space, may be written as

$$\varepsilon_0 = \frac{1}{\mu_0 c^2} \approx 8.854187817... \times 10^{-12}\,\mathrm{F\,s^{-1}}, \tag{1.2}$$

where, μ_0 is the magnetic permeability of free space, defined as

$$\mu_0 = 4\pi \times 10^7\,\mathrm{N\,A^{-2}}, \tag{1.3}$$

and $c = 299\,792\,458\ \mathrm{m\,s^{-1}}$ is the speed of light. $k_B \approx 1.38 \times 10^{-23}\,\mathrm{J\,K^{-1}}$ is the Boltzmann constant, and q is the charge of a particle. We may now define a plasma as a collection of charge particles whose number density, n, is very large in a sphere of radius λ_D,

$$\frac{4}{3}\pi\lambda_D^3 n \gg 1. \tag{1.4}$$

Typical values of the Debye length are of the order of 10^{-3} m in the corona, 10^{-11} m in the solar core, and 10 m in the solar wind.

The second assumption we must make is that the plasma may be treated as a continuum. This is valid provided the length-scales of gradients in the plasma are much greater than characteristic plasma lengths, such as the gyroradius (also called the Larmor radius or cyclotron radius), which is defined as

$$r_g = \frac{m v_\perp}{|q|B}.$$

Here, m is the mass of the particle, $v_\perp$ is the component of the velocity perpendicular to the magnetic field, and q is the electric charge of the particle. Furthermore, we assume that the plasma is in thermodynamic equilibrium, such that its distribution function is close to Maxwellian. This assumption is true for time scales much greater than the collision times, and length scales much greater than the mean free path of the plasma. The mean free path in the ambient corona may be up to 1 km due to the low particle density of the plasma.

We also assume that we may treat the plasma as a single fluid. This is a good approximation for applications to the photosphere and corona, but may not be accurate for models of the chromosphere since interactions between ions and neutrals are significant in that region.

We also assume that the equations are formulated for an inertial frame, and that the typical plasma velocity is non-relativistic. We may write this second condition as $v_0 \ll c$, where v_0 is the typical speed of the plasma.

Note that, in this Thesis, we only consider adiabatic, inviscid, and ideal plasmas, so that we may neglect any terms related to heat transfer, viscosity and resistivity, when deriving the ideal MHD equations.

Finally, we note that all equations shall be considered in their differential form in m k s units.

1.3.2 Maxwell's Equations

We begin by considering the first of Maxwell's equations of classical electrodynamics, which is Gauss's law for the electric field,

$$\nabla \cdot \mathbf{E} = \frac{\tau}{\varepsilon_0}. \tag{1.5}$$

This states that the divergence of the electric field is equal to the total electric charge density divided by the electric constant, ε_0, defined in Equation (1.2).

The second equation is the condition that there exist no magnetic monopoles. This equation is also known as Gauss's law for magnetism, and may be written as

$$\nabla \cdot \mathbf{B} = 0. \tag{1.6}$$

Equation (1.6) states that magnetic fields must be solenoidal vector fields. As a consequence, point charges of magnetic field, analogous to electric charges, may not exist.

The third equation is the Maxwell-Faraday equation,

$$\nabla \times \mathbf{E} = -\frac{\partial \mathbf{B}}{\partial t}, \tag{1.7}$$

which states that any change of the magnetic field in time, will coincide with a spatially varying non-conservative electric field, and vice-versa. A straightforward example of this concept is that of the generation of electric current in a dynamo using a permanent magnet, such as a bar magnet. In such an instrument, a rotating magnet surrounded by coils of wire, creates electric current in the wires.

The final equation is known as Ampère's circuital law,

$$\nabla \times \mathbf{B} = \mu_0 \mathbf{j} + \frac{1}{c^2}\frac{\partial \mathbf{E}}{\partial t}, \tag{1.8}$$

which states that magnetic fields may be generated through both an induced electric current, and a change in the electric field. Only the first mechanism was originally included in Ampère's law, while the second mechanism is due to Maxwell. It follows from Equations (1.7) and (1.8) that time-varying electric and magnetic fields will generate spatially varying magnetic and electric fields, respectively.

1.3.3 Equations of Gas Dynamics

Having introduced Maxwell's equations, (1.5) – (1.8), we now wish to introduce the equations governing the dynamical evolution of the density, $\rho(\mathbf{r}, t)$, pressure $p(\mathbf{r}, t)$, and velocity $\mathbf{v}(\mathbf{r}, t)$ of a plasma. Before we proceed, we must introduce the Lagrangian time-derivative of a fluid,

$$\frac{\mathrm{D}}{\mathrm{D}t} = \frac{\partial}{\partial t} + \mathbf{v} \cdot \nabla \tag{1.9}$$

which is evaluated in the frame of reference of a moving fluid, and differs from the Eulerian time-derivative, $\partial/\partial t$, which is evaluated at a fixed point.

Since we are only concerned with ideal MHD, we only consider the equations of conservation of mass, momentum and energy of adiabatic and inviscid plasmas. The equation for the evolution of the density, most conveniently written

$$\frac{\mathrm{D}\rho}{\mathrm{D}t} + \rho \nabla \cdot \mathbf{v} = 0, \tag{1.10}$$

is called the mass continuity equation, and may also be written

$$\frac{\partial \rho}{\partial t} + \nabla \cdot (\rho \mathbf{v}) = 0. \tag{1.11}$$

In this form, we can see that it represents conservation of mass, since an increase in density at a point, represented by a positive $\partial\rho/\partial t$, is accompanied by mass flowing in, i.e. $\nabla \cdot (\rho \mathbf{v}) < 0$.

We introduce the energy equation, which may be written in terms of the internal energy per unit mass, e (measured in $\mathrm{J\,kg^{-1}}$),

$$\rho \frac{\mathrm{D}e}{\mathrm{D}t} - \frac{p}{\rho} \frac{\mathrm{D}\rho}{\mathrm{D}t} = -\mathcal{L}, \tag{1.12}$$

where $\mathcal{L}$ is the energy loss function (measured in $\mathrm{J\,m^{-3}\,s^{-1}}$). Since we are only considering adiabatic processes, the energy gains and losses balance, so that $\mathcal{L} \equiv 0$, and Equation (1.12) may be written as

$$\rho \frac{\mathrm{D}e}{\mathrm{D}t} - \frac{p}{\rho} \frac{\mathrm{D}\rho}{\mathrm{D}t} = 0, \tag{1.13}$$

such that energy is conserved. In order to further simplify Equation (1.13), we wish to eliminate the internal energy and obtain an equation relating the pressure and density. The plasma pressure is determined by an equation of state, which we assume to be the ideal gas law,

$$p = \frac{k_B}{m} \rho T, \tag{1.14}$$

where m is the mean mass (measured in kg) of the particles that make up the plasma, and T is the absolute temperature of the plasma (measured in K). For an ideal gas, the heat capacity is constant with temperature, and we may write the internal energy as

$$e = c_v T, \tag{1.15}$$

where c_v is the specific heat at constant volume. We define the specific heat at constant pressure as

$$c_p = c_v + \frac{k_B}{m}, \tag{1.16}$$

and the ratio of specific heats (also called the adiabatic index),

$$\gamma = \frac{c_v}{c_p}. \tag{1.17}$$

We may write the specific heat at constant volume as

$$c_v = \frac{1}{\gamma - 1}\frac{k_B}{m}, \tag{1.18}$$

and combine Equations (1.14), (1.15), and (1.18) to obtain

$$e = \frac{1}{\gamma - 1}\frac{p}{\rho}. \tag{1.19}$$

We substitute (1.19) into (1.13) to obtain the desired form of the energy equation,

$$\frac{\mathrm{D}p}{\mathrm{D}t} - \frac{\gamma p}{\rho}\frac{\mathrm{D}\rho}{\mathrm{D}t} = 0. \tag{1.20}$$

It is worth noting that, the adiabatic index is related to the number of degrees of freedom of a molecule by $\gamma = 1 + 2/f$, where f is the number of degrees of freedom. Since, in this Thesis, we are primarily concerned with fully ionised monoatomic plasmas characteristic of the solar corona, we may assume that $f = 3$, and $\gamma = 5/3$.

The final equation of gas dynamics is the equation of motion for a fluid element, which connects the equations of electrodynamics, described in Subsection 1.3.2, with the gas dynamics equations described in the current section. In order for conservation of momentum to be satisfied, we require

$$\rho\frac{\mathrm{D}\mathbf{v}}{\mathrm{D}t} = \mathbf{F}, \tag{1.21}$$

where $\mathbf{F}$ (measured in units of force density, $\mathrm{N\,m^{-3}}$) is given by

$$\mathbf{F} \equiv -\nabla p + \rho\mathbf{g} + \mathbf{j}\times\mathbf{B} + \tau\mathbf{E}. \tag{1.22}$$

1.3.4 The Equations of Ideal MHD

In order to connect the equations of electrodynamics, described in Subsection 1.3.2, with the equations of gas dynamics described in Subsection 1.3.3, we begin by introducing Ohm's law, which links the electric, magnetic and velocity fields via the current density, such that

$$\mathbf{E} + \mathbf{v} \times \mathbf{B} = \eta \mathbf{j}, \tag{1.23}$$

where η is the electrical resistivity (measured in $\Omega\,\mathrm{m}$). In this Thesis, we are not concerned with situations where non-ideal effects, such as resistivity, play an important role. As such, we may set $\eta = 0$, and Ohm's law reduces to

$$\mathbf{E} + \mathbf{v} \times \mathbf{B} = 0. \tag{1.24}$$

From Equation (1.24), we see that the typical scales of the magnitude of the electric field, E, and magnetic field, B, satisfy

$$E \sim -vB. \tag{1.25}$$

We now return to Equation (1.8), and find that

$$\frac{1}{c^2}\left|\frac{\partial \mathbf{E}}{\partial t}\right| \sim \frac{v}{c^2}\frac{B}{t_0} = \frac{v^2}{c^2}\frac{B}{l_0} = \mathcal{O}(v^2/c^2), \tag{1.26}$$

where t_0 and l_0 are the characteristic time and length scales. Here, $\mathcal{O}$, represents the order of a quantity, and is known as Big $\mathcal{O}$ notation. The quantity in Equation (1.26) is much smaller than the term on the LHS of Equation (1.8), which is $|\nabla \times \mathbf{B}| \sim B/l_0$. It follows that the term in Equation (1.26) may be neglected from Equation (1.8), and we recover the original form of Ampère's law,

$$\mathbf{j} = \frac{1}{\mu_0}\nabla \times \mathbf{B}. \tag{1.27}$$

The equation of motion, (1.21), is also simplified by the assumption of non-relativistic velocities. Using Equations (1.5) and (1.25), we find that the electrostatic acceleration satisfies

$$\tau|\mathbf{E}| \sim \frac{vB}{\mu_0 c^2 l_0} \times vB = \frac{v^2}{c^2}\frac{B^2}{\mu_0 l_0} = \mathcal{O}(v^2/c^2). \tag{1.28}$$

Using Equation (1.27), we find that $\tau|\mathbf{E}| \ll |\mathbf{j} \times \mathbf{B}| \sim B^2/\mu_0 l_0$. This means that the final term in Equation (1.22) may be neglected, and the equation of motion becomes

$$\rho\frac{\mathrm{D}\mathbf{v}}{\mathrm{D}t} = -\nabla p + \rho\mathbf{g} + \mathbf{j} \times \mathbf{B}, \tag{1.29}$$

Finally, we combine Equations (1.7) and (1.24) to obtain the induction equation,

$$\frac{\partial \mathbf{B}}{\partial t} - \nabla \times (\mathbf{v} \times \mathbf{B}) = 0. \tag{1.30}$$

We have, thus, obtained a system of 8 coupled partial differential equations, Equations (1.10), (1.20), (1.29), and (1.30), which constitute the system of ideal MHD equations. Equation (1.6), the condition that there are no magnetic monopoles, is also part of this system, but is always satisfied if it is satisfied as an initial condition. We can see this if we take the divergence, $\nabla \cdot$, of Equation (1.30).

1.3.5 Consequences of Ideal MHD

A first remark on the ideal MHD equations comes from the momentum equation, (1.29), where the term $\mathbf{j} \times \mathbf{B}$, called the *Lorentz force*, may be written as

$$\mathbf{j} \times \mathbf{B} = \frac{1}{\mu_0}(\nabla \times \mathbf{B}) \times \mathbf{B} = \frac{(\mathbf{B} \cdot \nabla)\mathbf{B}}{\mu_0} - \nabla \left(\frac{\mathbf{B}^2}{2\mu_0} \right). \tag{1.31}$$

The first term on the right-hand side is called the *magnetic tension* force, while the second is the *magnetic pressure* force. It may be shown that the magnetic tension results in a negative stress in a direction parallel to $\mathbf{B}$, while the magnetic pressure causes a positive stress normal to $\mathbf{B}$ (Goedbloed and Poedts, 2004).

A second result of note is Alfvén's frozen flux theorem, which states that, in ideal MHD, magnetic flux is conserved so that the magnetic field moves with the plasma. This is in addition to the quantities that we already know are conserved, from the Euler equations, namely mass, energy and momentum.

While the ideal MHD equations have various other properties, we restrict our discussion to the two above, as they are most relevant in this Thesis.

1.3.6 The Linear Ideal MHD Equations

The nonlinear form of the MHD Equations is difficult to treat analytically in most situations. For many applications, we may *linearise* Equations (1.10), (1.20), (1.29), and (1.30) in the following way. We assume that the dependent variables, $\mathbf{v}, \mathbf{B}, \rho$ and p, may be split into two distinct quantities: a *background* (or *equilibrium*) value, and a small *perturbation*. We write this as

$$\begin{aligned} \mathbf{v} &= \mathbf{v_0} + \mathbf{v}', \qquad & \mathbf{B} &= \mathbf{B_0} + \mathbf{b}', \\ \rho &= \rho_0 + \rho', \qquad & p &= p_0 + p', \end{aligned} \tag{1.32}$$

where the subscript 0 represents the background value, and the apostrophe denotes the perturbation. We assume that the perturbations of the magnetic field, density and pressure are much smaller than their equilibrium values, i.e.

$$|\mathbf{B_0}| \gg |\mathbf{b}'|, \qquad \rho_0 \gg \rho', \qquad p_0 \gg p'. \tag{1.33}$$

This assumption is not always applicable to the velocity perturbation since the background flow may be zero ($\mathbf{v_0} = \mathbf{0}$). In such cases, we say that the velocity perturbation is much smaller than some other characteristic speed of the system, such as the local speed of sound,

$$c_s = \sqrt{\gamma \frac{p_0}{\rho_0}}, \tag{1.34}$$

or Alfvén speed

$$v_A = \sqrt{\frac{B_0^2}{\mu_0 \rho}}. \tag{1.35}$$

It is worth noting that the background quantities may be inhomogeneous spatially and may evolve temporally.

We, now, insert Equations (1.32) into Equations (1.10), (1.20), (1.29), and (1.30), and neglect nonlinear coupling due to products of perturbations. This yields the system of linear ideal MHD equations

$$\frac{\mathrm{D}\rho'}{\mathrm{D}t} + \rho_0 \nabla \cdot \mathbf{v}' = 0, \tag{1.36}$$

$$\frac{\mathrm{D}p'}{\mathrm{D}t} = c_s^2 \frac{\mathrm{D}\rho'}{\mathrm{D}t}, \tag{1.37}$$

$$\rho_0 \frac{\mathrm{D}\mathbf{v}'}{\mathrm{D}t} = -\nabla p' + \frac{1}{\mu_0}(\nabla \times \mathbf{b}') \times \mathbf{B_0}, \tag{1.38}$$

$$\frac{\partial \mathbf{b}'}{\partial t} = \nabla \times (\mathbf{v_0} \times \mathbf{b}') + \nabla \times (\mathbf{v}' \times \mathbf{B_0}), \tag{1.39}$$

$$\nabla \cdot \mathbf{b}' = 0,$$

where the Lagrangian derivative is now defined as

$$\frac{\mathrm{D}}{\mathrm{D}t} = \frac{\partial}{\partial t} + \mathbf{v_0} \cdot \nabla, \tag{1.40}$$

and the apostrophe was dropped when writing the perturbations. In deriving Equations (1.36) - (1.39), we have neglected gravity, since the models we derive in this Thesis have applications to small-scale phenomena, where gravity does not have a strong effect. We also assumed that $\mathbf{B_0}, \rho_0$ and p_0 are spatially homogeneous in each layer, and do not evolve temporally (i.e. independent of $\mathbf{r}$ and t), and $\mathbf{v_0}$ is homogeneous in space in each layer (i.e. independent of $\mathbf{r}$). These assumptions are not true in general, but are sufficient for the analyses in this Thesis.

1.3.7 Equations of Incompressible Ideal MHD

A special form of the ideal MHD equations, which we will make use of later in this Thesis, assumes that all motion is incompressible. We define incompressibility as the property that density is constant in a fluid, such that the MHD Equations (neglecting gravity) are reduced to

$$\begin{aligned}
\frac{\mathrm{D}\mathbf{v}}{\mathrm{D}t} &= -\frac{1}{\rho}\nabla p_T + \frac{1}{\mu_0\rho}(\mathbf{B}\cdot\nabla)\mathbf{B}, && (1.41)\\
\frac{\mathrm{D}\mathbf{B}}{\mathrm{D}t} &= (\mathbf{B}\cdot\nabla)\mathbf{v}, && (1.42)\\
\nabla\cdot\mathbf{v} &= 0, && (1.43)\\
\nabla\cdot\mathbf{B} &= 0,
\end{aligned}$$

where p_T is the total (gas plus magnetic) pressure, and the Lagrangian derivative is given by Equation (1.9).

Following the method described in Subsection 1.3.6, we linearise Equations (1.41) - (1.43), and obtain

$$\begin{aligned}
\frac{\mathrm{D}\mathbf{v}'}{\mathrm{D}t} &= -\frac{1}{\rho_0}\nabla p_T' + \frac{1}{\mu_0\rho_0}(\mathbf{B_0}\cdot\nabla)\mathbf{b}', && (1.44)\\
\frac{\mathrm{D}\mathbf{b}'}{\mathrm{D}t} &= (\mathbf{B_0}\cdot\nabla)\mathbf{v}', && (1.45)\\
\nabla\cdot\mathbf{v}' &= 0, && (1.46)\\
\nabla\cdot\mathbf{b}' &= 0,
\end{aligned}$$

where p_T' is the perturbation of the total pressure, and the Lagrangian derivative is given by Equation (1.40). As in Subsection 1.3.6, we have assumed that the background quantities are spatially homogeneous, and $\mathbf{B_0}$ is also independent of t.

We now introduce the plasma displacement, $\boldsymbol{\xi}(\mathbf{r}, t)$, which is related to the velocity by

$$\mathbf{v}' = \frac{\mathrm{D}\boldsymbol{\xi}}{\mathrm{D}t} = \frac{\partial}{\partial t} + (\mathbf{v_0}\cdot\nabla)\boldsymbol{\xi}. \tag{1.47}$$

Substituting Equation (1.47) into Equation (1.46), we obtain

$$\frac{\mathrm{D}}{\mathrm{D}t}(\nabla\cdot\boldsymbol{\xi}) = 0, \tag{1.48}$$

since $\mathbf{v_0}$ is independent of $\mathbf{r}$, meaning that the operators $\mathrm{D}/\mathrm{D}t$ and $\nabla\cdot$ commute. The Lagrangian derivative cannot be zero since $\boldsymbol{\xi}$ is time-dependent, which implies that the displacement must also be divergence free, i.e.

$$\nabla\cdot\boldsymbol{\xi} = 0. \tag{1.49}$$

We will use Equation (1.49) in Chapter 3.

1.4 Magnetohydrodynamic Waves

A fundamental property of the system of linear MHD equations presented in Subsection 1.3.6 is that it allows for solutions in the form of waves. In the following Subsections, we shall give a brief analysis of wave motions in both homogeneous media, and in the presence of structuring. In this Thesis, we are primarily concerned with magnetoacoustic waves, and although Alfvén waves are mentioned, they will not receive a detailed description.

In Subsection 1.4.1, we derive the dispersion equation for the basic wave modes that may propagate in a homogeneous unbounded plasma governed by the ideal linear MHD equations. In the rest of the Section, we discuss the behaviour of the magnetoacoustic modes in the presence of three types of structuring: a plane Cartesian *interface* separating two media, two parallel interfaces which form a *slab*, and the *cylindrical flux tube*.

Our discussion of the magnetoacoustic modes in structured plasmas is largely based on the derivations included in Roberts (1981*a*,*b*); Edwin and Roberts (1982), as well as Goedbloed and Poedts (2004); Priest (2014). It is worth noting, though, that the study of magnetoacoustic waves in structured media has a longer history, with works such as Cram and Wilson (1975); Defouw (1976); Roberts and Webb (1978); Wilson (1978); Roberts and Webb (1979); Wentzel (1979); Wilson (1979); Spruit (1981) having set the foundations for the more structured approach of Roberts and Edwin.

1.4.1 Linear MHD Waves in a Homogeneous Medium

We begin by assuming that all background quantities are homogeneous, i.e. independent of $\mathbf{r}$ and t. Furthermore, we assume that the background medium is static ($\mathbf{v_0} = \mathbf{0}$), and the magnetic field is defined as $\mathbf{B_0} = (0, 0, B_0)$, without loss of generality. The assumption that $\mathbf{v_0} = \mathbf{0}$ is made in order to discuss only MHD waves, and not flow instabilities. The MHD Equations (1.36) - (1.39) may, therefore, be reduced to

$$\frac{\partial p'}{\partial t} = -c_s^2 \rho_0 \nabla \cdot \mathbf{v}', \tag{1.50}$$

$$\rho_0 \frac{\partial \mathbf{v}'}{\partial t} = -\nabla p' + \frac{1}{\mu_0}(\nabla \times \mathbf{b}') \times \mathbf{B_0}, \tag{1.51}$$

$$\frac{\partial \mathbf{b}'}{\partial t} = \nabla \times (\mathbf{v}' \times \mathbf{B_0}), \tag{1.52}$$

$$\nabla \cdot \mathbf{b}' = 0.$$

where we have combined the mass and energy equations. Once again, we make use of the displacement vector, first introduced in Equation (1.47). Since we have assumed no background flow, the displacement is now related to the velocity as

$$\mathbf{v}' = \frac{\partial \boldsymbol{\xi}}{\partial t}. \tag{1.53}$$

We introduce Equation (1.53) into Equations (1.50) and (1.52), and we may immediately integrate them with respect to time to obtain

$$p' = -c_s^2 \rho_0 \nabla \cdot \boldsymbol{\xi}, \tag{1.54}$$

$$\mathbf{b}' = \nabla \times (\boldsymbol{\xi} \times \mathbf{B_0}). \tag{1.55}$$

Substituting Equations (1.53), (1.54), and (1.55) into (1.51) yields

$$\frac{\partial^2 \boldsymbol{\xi}}{\partial t^2} = c_s^2 \nabla(\nabla \cdot \boldsymbol{\xi}) + \frac{1}{\mu_0 \rho_0} \mathbf{B_0} \times (\nabla \times \nabla \times (\mathbf{B_0} \times \boldsymbol{\xi})) \tag{1.56}$$

In deriving Equation (1.56), we have used the property that the cross product is anti-commutative.

We consider plane wave solutions of the form

$$\boldsymbol{\xi} = \hat{\boldsymbol{\xi}} \mathrm{e}^{i(\mathbf{k}\cdot\mathbf{r} - \omega t)}, \tag{1.57}$$

where $\mathbf{k} = (k_x, 0, k_z)$ is the wave vector, and ω is the angular frequency. The $\perp$ and $\|$ signs represent the components of the wave vector perpendicular and parallel to the magnetic field, respectively. The differential operators now turn into algebraic multiplication factors,

$$\nabla \to i\mathbf{k}, \qquad \frac{\partial}{\partial t} \to -i\omega, \tag{1.58}$$

and Equation (1.56) becomes

$$-\omega^2\hat{\boldsymbol{\xi}} = c_s^2\mathbf{k}(\mathbf{k}\cdot\hat{\boldsymbol{\xi}}) + \frac{1}{\mu_0\rho_0}\mathbf{B_0}\times(\mathbf{k}\times\mathbf{k}\times(\mathbf{B_0}\times\hat{\boldsymbol{\xi}})). \tag{1.59}$$

We now introduce the vectorial Alfvén speed,

$$\mathbf{v_A} = \frac{\mathbf{B_0}}{\sqrt{\mu_0\rho_0}} = (0, 0, v_A), \tag{1.60}$$

and, with the help of the vector identities in Goedbloed and Poedts (2004), we rewrite Equation (1.59) as

$$\left\{\left[\omega^2 - (\mathbf{k}\cdot\mathbf{v_A})^2\right]\mathbf{I} - (c_s^2 + v_A^2)\mathbf{kk} + \mathbf{k}\cdot\mathbf{v_A}(\mathbf{kv_A} + \mathbf{v_A k})\right\}\cdot\hat{\boldsymbol{\xi}} = 0, \tag{1.61}$$

where $\mathbf{I}$ is the unit tensor, and the lack of symbols between vectors, as in $\mathbf{kk}$, represents the dyadic product. Equation (1.61) may be written in matrix form as

$$\begin{pmatrix} \omega^2 - k_x^2(c_s^2 + v_A^2) - k_z^2 v_A^2 & 0 & -k_x k_z c_s^2 \\ 0 & \omega^2 - k_z^2 v_A^2 & 0 \\ -k_x k_z c_s^2 & 0 & \omega^2 - k_z^2 c_s^2 \end{pmatrix} \begin{pmatrix} \hat{\xi}_x \\ \hat{\xi}_y \\ \hat{\xi}_z \end{pmatrix} = \mathbf{0}. \tag{1.62}$$

In order for Equation (1.61) to have non-trivial solutions, we require that the determinant of the matrix in Equation (1.62) be zero. We calculate the determinant and obtain the dispersion relation for MHD waves in a homogeneous unbounded medium,

$$(\omega^2 - k_z^2 v_A^2)\left[\omega^4 - \omega^2 k^2(c_s^2 + v_A^2) + k_z^2 k^2 v_A^2 c_s^2\right] = 0, \tag{1.63}$$

where $k = |\mathbf{k}| = \sqrt{k_x^2 + k_z^2}$.

Before we analyse Equation (1.63), we note that, due to the fact that we obtained the dispersion relation from a description of the system in terms of the displacement, we omitted the entropy wave. This mode, corresponding to $\omega = 0$, is degenerate in the sense that it involves no perturbations of the flow, magnetic field or pressure. It constitutes a perturbation of the entropy of the system (density and internal energy) which would propagate if a background flow was present.

The first class of solutions of Equation (1.63) are obtained from the quadratic factor, and are called *Alfvén waves*. They propagate with frequency

$$\omega = \pm\omega_A = \pm k_z v_A = \pm k v_A \cos\phi, \tag{1.64}$$

where ϕ is the angle between $\mathbf{k}$ and $\mathbf{B_0}$, and ω_A is called the Alfvén frequency. The ± represents the two possible solutions: one propagating in the direction of

$\mathbf{B_0}$, and corresponding to the + sign, and the other propagating in the opposite direction, and corresponding to the − sign. These waves are incompressible and purely transverse.

The second category of solutions of Equation (1.63) we discuss are *magnetoacoustic* (or *magnetosonic*) *waves*, which are obtained from the quartic factor. They are split into two categories, slow modes and fast modes, which propagate with frequencies

$$\omega = \pm\omega_s, \qquad \omega = \pm\omega_f, \tag{1.65}$$

respectively. The slow and fast frequencies are defined as

$$\omega_{s,f} = \frac{1}{2}k^2(c_s^2 + v_A^2)\big(1 \pm \sqrt{1 - 4c_T^2\cos^2\phi}\big), \tag{1.66}$$

where

$$c_T = \frac{c_s v_A}{\sqrt{c_s^2 + v_A^2}}, \tag{1.67}$$

is called the tube speed (or cusp speed or slow speed). Similarly to the Alfvén wave solutions, the ± sign in Equation (1.65) corresponds to forward (+) and backward (−) propagating waves. The ± sign in Equation (1.66) corresponds to either the fast mode (+), or the slow mode (−).

1.4.2 Linear MHD Waves at a Tangential Interface

For the first case of inhomogeneous structuring, we utilise a Cartesian coordinate system as in the previous section, and introduce a tangential discontinuity in the yz-plane at $x = 0$. This interface separates regions of different homogeneous plasma density, temperature, pressure and magnetic field. We use the subscript 0 and 1 to denote background quantities for $x < 0$ and $x > 0$, respectively. The background magnetic field is assumed to be parallel to the z-axis on both sides of the interface.

Since the described system is inhomogeneous along the x-axis, we may no longer Fourier decompose the MHD Equations (1.36) - (1.39), with respect to x. Furthermore, we only wish to study magnetoacoustic waves propagating along the interface, which we accomplish by assuming that all variables are independent of y. This implies a decomposition of the form $f(\mathbf{r}, t) = \hat{f}(x)\exp i(k_z z - \omega t)$, where f stands for any of the dependent variables. We also drop the apostrophe from the perturbed quantities for ease of writing.

Our aim is to obtain governing equations for both sides of the interface, solve them, and match the solutions across the interface using appropriate boundary conditions. We save the derivation of the governing equations for Chapter 2, and present the equation directly,

$$\frac{\mathrm{d}^2\hat{v}_x}{\mathrm{d}x^2} - m_j^2\hat{v}_x = 0, \tag{1.68}$$

where

$$m_j^2 = k_z^2\frac{(c_j^2 - c_{ph}^2)(v_{Aj}^2 - c_{ph}^2)}{(c_j^2 - v_{Aj}^2)(c_{Tj}^2 - c_{ph}^2)}, \qquad j = 0, 1. \tag{1.69}$$

Here, $\hat{v}_x$ is the component of the velocity perturbation perpendicular to the boundary, c_j are the sound speeds, v_{Aj} are the Alfvén speeds, c_{Tj} are the tube speeds, and $c_{ph} = \omega/k_z$ is the phase speed. The parameter m_j is sometimes called the effective wavenumber. Note that the derivation for Equations (1.68) and (1.69) may also be found in Roberts (1981*a*), or in modern textbooks such as Goedbloed and Poedts (2004) or Priest (2014).

Equation (1.68) has two distinct classes of solutions: *trapped modes*, with $m_j^2 > 0$, which decay as $x \to \infty$ (see Figure 1.4a), and *leaky modes*, with $m_j^2 < 0$, which propagate towards infinity. We also note that there exists an unbound state propagating from infinity. We only consider trapped modes and solve Equation (1.68),

$$\hat{v}_x(x) = \begin{cases} C_0\mathrm{e}^{m_0 x}, & x < 0, \\ C_1\mathrm{e}^{-m_1 x}, & x > 0, \end{cases} \tag{1.70}$$

where C_0 and C_1 are arbitrary constants. The boundary conditions imposed at $x = 0$ are that of *continuity of displacement*, and *continuity of total pressure*. Since we are considering a static background ($\mathbf{v_0} = \mathbf{0}$), the first of these conditions is equivalent to continuity of $\hat{v}_x$. The total pressure is found to be

$$\hat{p}_T = \frac{i\rho_j}{\omega}(c_j^2 + v_{Aj}^2)\frac{c_{Tj}^2 - c_{ph}^2}{c_j^2 - c_{ph}^2}\frac{\mathrm{d}\hat{v}_x}{\mathrm{d}x}, \tag{1.71}$$

and the condition of continuity of total pressure yields the dispersion relation for waves propagating along an interface,

$$c_{ph}^2 = v_{A0}^2 - \frac{\rho_1 m_0}{\rho_1 m_0 + \rho_0 m_1}(v_{A0}^2 - v_{A1}^2). \tag{1.72}$$

1.4.3 Linear MHD Waves on a Slab in a Symmetric Environment

The *magnetic slab*, formed of two parallel interfaces in a non-magnetic environment, was considered by Roberts (1981*b*), and in a magnetic environment by

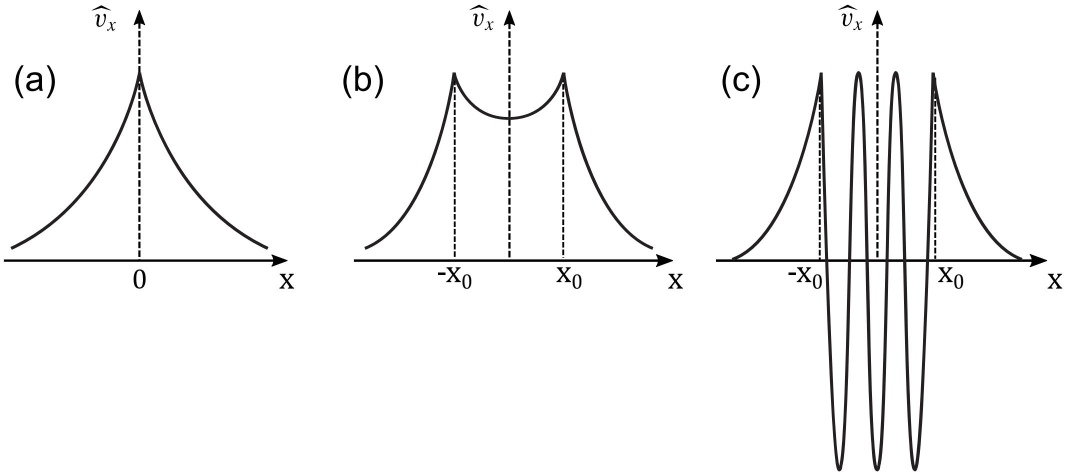

Figure 1.4: A schematic representation of the profile of the velocity amplitude for three different cases: (a) trapped waves on an interface; (b) surface waves in a slab; (c) body waves in a slab. Adapted from Priest (2014).

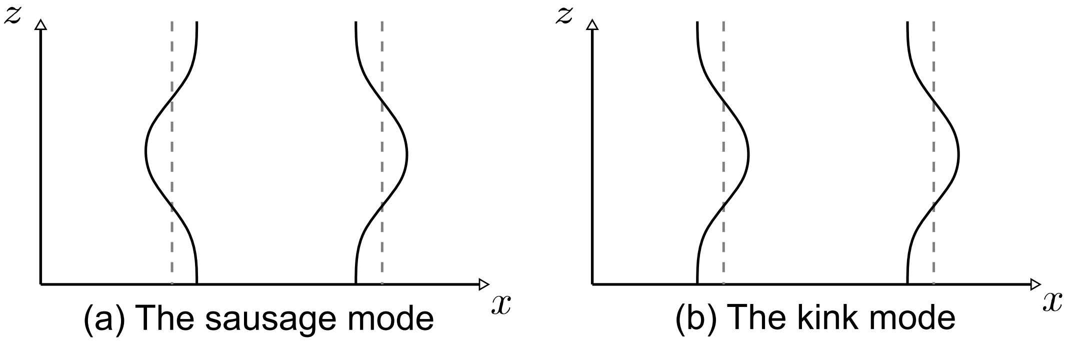

(a) The sausage mode

(b) The kink mode

Figure 1.5: A schematic representation of the two modes of oscillation of a magnetic slab.

Edwin and Roberts (1982). Here, we consider a slab with boundaries at $\pm x_0$ in a non-magnetised symmetric environment. Background quantities will be denoted by subscripts 0 and 1 in the regions $|x| < x_0$ and $|x| > x_0$, respectively. Equation (1.68) now has trapped solutions of the form

$$\hat{v}_x(x) = \begin{cases} C_{10}\mathrm{e}^{m_1(x+x_0)}, & x < -x_0, \\ C_{00}\cosh m_0x + C_{01}\sinh m_0x, & |x| \leq x_0, \\ C_{11}\mathrm{e}^{-m_1(x-x_0)}, & x > x_0, \end{cases} \tag{1.73}$$

where $C_{00}, C_{01}, C_{10}, C_{11}$ are constants. The sign of m_0^2 determines the nature of the waves within the slab. If $m_0^2 > 0$, the wave is evanescent inside the slab and is called a *surface* mode (Figure 1.4b), whereas if $m_0^2 < 0$, the wave is oscillatory inside the slab and is called a *body* mode (Figure 1.4c). Furthermore, if $C_{00} = 0$, then $\hat{v}_x(x)$ is an odd function, while if $C_{01} = 0$, then $\hat{v}_x$ is an even function.

The total pressure defined in (1.71) is used, and we apply the boundary conditions as for the interface to obtain the dispersion relation for waves propagating along a magnetic slab embedded in a symmetric magnetic environment. The dispersion relation is factorised into two separate equations,

$$\begin{aligned} \rho_1(v_{A1}^2 - c_{ph}^2)m_0\tanh(m_0x_0) + \rho_0(v_{A0}^2 - c_{ph}^2)m_1 = 0, \\ \rho_1(v_{A1}^2 - c_{ph}^2)m_0\coth(m_0x_0) + \rho_0(v_{A0}^2 - c_{ph}^2)m_1 = 0, \end{aligned} \tag{1.74}$$

where the equation containing tanh/coth corresponds to the sinh/cosh term in Equation (1.73). It follows that the tanh and coth equations describe modes of oscillation whose displacements are antisymmetric and symmetric around $x = 0$, respectively. These modes are called the *sausage* and *kink* modes, and are illustrated in Figure 1.5. Approximate analytical solutions, as well as general numerical solutions to Equations (1.74) may be found, for example in Edwin and Roberts (1982).

Solutions of Equations (1.74) are always neutrally stable since $\omega^2 > 0$. If $\omega^2 < 0$, the left hand side of Equations (1.74) would always be positive, and we would have a contradiction. Therefore, ω is real, and $\exp i(k_z z - \omega t)$ is always oscillatory. This also makes sense from a physical point of view since there are no effects that may cause the equilibrium to become unstable, such as gravity or shearing flows. We shall encounter dispersion relations with complex solutions in Chapter 2.

1.4.4 Linear MHD Waves in a Cylindrical Flux Tube

The final type of structuring that we need to address is the cylindrical flux tube. We now use the cylindrical coordinate system (r, ϕ, z) and assume that a cylindrical interface at $r = r_0$ separates an interior region, denoted with the subscript 0, from an exterior region, denoted by the subscript 1.

Similarly to Subsections 1.4.2 and 1.4.3, we write perturbations of the cylindrical interface as $f = \hat{f}\exp\{i(k_z z + m\phi - \omega t)\}$, where k_z and ϕ are the wavenumbers corresponding to the z- and ϕ-directions, respectively. The linear ideal MHD equations may now be reduced to the governing equation

$$\frac{\mathrm{d}^2\hat{p}_T}{\mathrm{d}t^2} + \frac{1}{r}\frac{\mathrm{d}\hat{p}_T}{\mathrm{d}r} + \left(\frac{m^2}{r^2} + m_j^2\right)\hat{p}_T = 0, \tag{1.75}$$

where m_j is defined in Equation (1.69), the total pressure is related to the radial component of the velocity as

$$\frac{\mathrm{d}\hat{p}_T}{\mathrm{d}r} = -i\omega\rho_0(\omega^2 - k_z^2 v_A^2)\hat{v}_r, \tag{1.76}$$

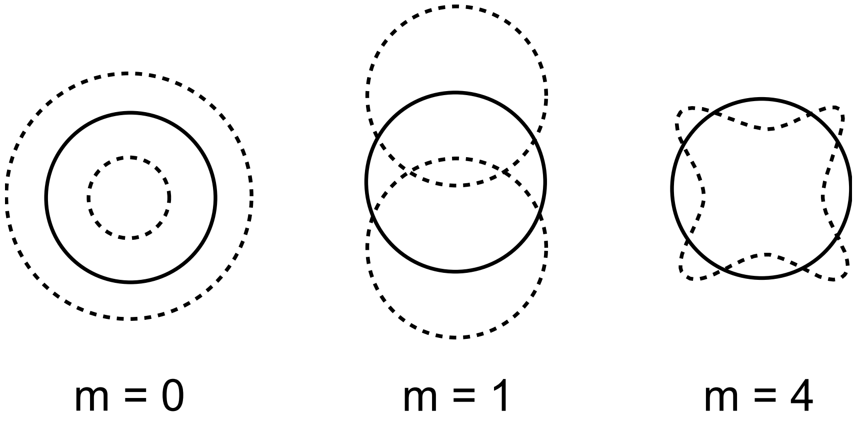

Figure 1.6: A schematic representation of a cut-through of a cylindrical flux tube undergoing a sausage oscillation ($m = 0$), kink oscillation ($m = 1$), and an $m = 4$ fluting oscillation. Adapted from Murdin (2001).

and m is an integer. The full derivation of Equations (1.75) and (1.76) are not included in this Thesis, and may be found in Edwin and Roberts (1983), or more recent works such as Goedbloed and Poedts (2004); Priest (2014).

The solutions to Equation (1.75) in the interior region ($r < r_0$) that are bounded on the axis of the cylinder, i.e. at $r = 0$, have the form

$$\hat{p}_T = C_0 \begin{cases} I_m(m_0 r), & m_0^2 > 0, \\ J_m(m_0 r), & n_0^2 = -m_0^2 > 0, \end{cases} \tag{1.77}$$

where C_0 is an arbitrary constant, and J_m and I_m are the Bessel function of the first kind of order m and modified Bessel function of the first kind of order m, respectively. The solution of Equation (1.75) in the exterior region ($r > r_0$) which is evanescent as $r \to \infty$ is

$$\hat{p}_T = C_1 K_m(m_1 r), \tag{1.78}$$

where C_1 is an arbitrary constant and K_m is the modified Bessel function of the second kind. Here m_0 and m_1 are defined as in Equation (1.69).

Using the boundary conditions of continuity of radial velocity and continuity of total pressure, we obtain the dispersion relation for surface modes

$$\rho_0(v_{Ai}^2 - c_{ph}^2) m_1 \frac{K'_m(m_1 r_0)}{K_m(m_1 r_0)} = \rho_1(v_{Ae}^2 - c_{ph}^2) m_0 \frac{I'_m(m_0 r_0)}{I_m(m_0 r_0)}, \tag{1.79}$$

where the dash represents the first derivative with respect to the argument. For body modes, the Bessel function I_m is replaced by J_m, and the effective wavenumber m_0 is replaced by n_0, where $n_0^2 = -m_0^2$.

Much like Equations (1.74), Equation (1.79) only has stable solutions ($\omega^2 > 0$). The main difference between the solutions of the dispersion relation of waves propagating along a slab and that of waves propagating along a cylinder, is that the cylindrical geometry supports additional modes of oscillation. The parameter m determines the wave mode, with $m = 0$ and $m = 1$ being the familiar sausage and kink modes, and $m > 1$ corresponding to the *fluting* modes (see Figure 1.6).

In deriving Equation (1.79) we assumed that the magnetic field is vertically straight both within and outside of the tube, which does not necessarily hold in applications to solar cylindrical magnetic waveguides. Several models of cylindrical flux tubes with twisted magnetic fields have been devised by, for example, Bennett et al. (1999); Erdélyi and Fedun (2006, 2007); Ruderman (2007); Erdélyi and Fedun (2010); Vasheghani Farahani et al. (2010); Ruderman (2015); Ruderman and Terradas (2015). These shall be important in the context of the Kelvin-Helmholtz instability of transversely (kink) oscillating flux tubes, in Chapter 3.

1.4.5 Coronal Loop Oscillations

In Subsections 1.4.2 - 1.4.4 we derived three of the most common theoretical models for magnetoacoustic waves in structured media relevant for solar applications. In this Subsection we wish to apply some of the theory discussed previously to one of the most fascinating objects of research in solar physics: coronal loops, first introduced in Subsection 1.2.2, and their modes of oscillation.

Coronal loops are most often modelled as straight magnetic cylinders, due to the fact that the curvature of the loop often plays little role on the properties of the oscillations (Van Doorsselaere et al., 2004). It follows that the loops would exhibit the modes of oscillation described in Subsection 1.4.4. Interpreting the observed modes in terms of the cylindrical model, as well as other models which we shall not discuss here, has led to the creation of the field of coronal seismology. It uses the properties of observed waves, in addition to knowledge of some background quantities, in order to determine parameters that are difficult to measure, such as the strength of the magnetic field.

While observations of sausage waves in coronal loops do exist (Nakariakov et al., 2003; Srivastava et al., 2008), by far the most common mode of oscillation is the fast kink mode. For reviews on the subject, see, for example, Nakariakov and Verwichte (2005); Ruderman and Erdélyi (2009); De Moortel and Nakariakov (2012).

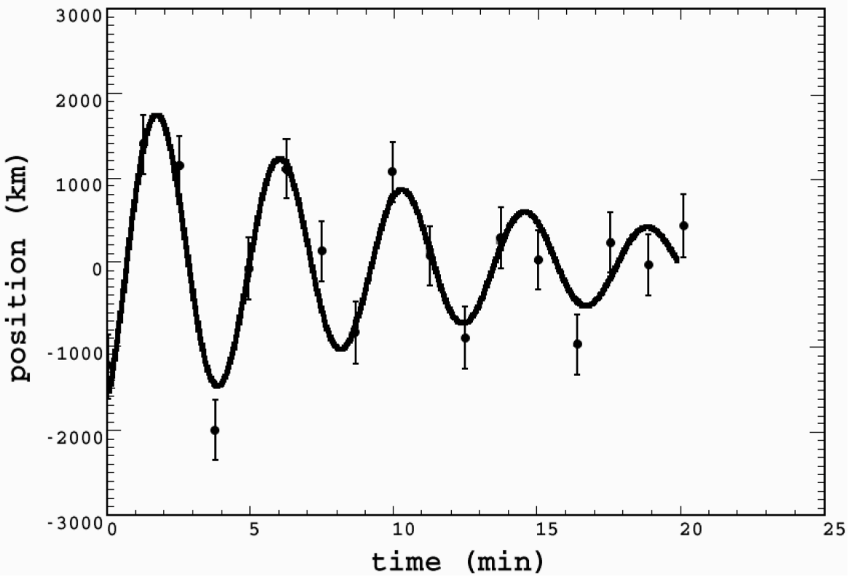

Figure 1.7: The temporal evolution of the displacement of the loop studied in Nakariakov et al. (1999), where the solid curve is the best fit function, and the error bars correspond to ±0.5 pixels.

Kink (or *transverse*) oscillations of coronal loops have been a subject of intensive study since their original observation on 14 July 1998 by the *Transition Region and Coronal Explorer* (TRACE) (Aschwanden et al., 1999; Nakariakov et al., 1999). A significant area of study has been their decay, which may be as fast as a single period, and up to around 5 periods (Goddard and Nakariakov, 2016), as may be seen in Figure 1.7. The leading theory meant to explain this phenomenon considers the fact that coronal loops should have a thin region where the high interior density decreases to a much lower value in the surrounding corona. Due to the effects of resonant absorption (Hollweg and Yang, 1988; Sakurai et al., 1991; Goossens et al., 2011) and phase mixing (Heyvaerts and Priest, 1983), energy is transferred from the transverse oscillation to the Alfvén mode (Ruderman and Roberts, 2002). It is worth noting that this phase mixed Alfvén mode may become Kelvin-Helmholtz unstable (Browning and Priest, 1984). This topic will be discussed further in Section 1.5, and Chapter 3.

Recently, several studies have found that there are also, so called, *decay-less transverse oscillations*. Nisticò et al. (2013); Anfinogentov et al. (2013, 2015) found that kink oscillations are commonly followed (and sometimes preceded) by a phase of, what appears to be, a low-amplitude transverse oscillation which does not decay. There are several theories as to the nature of this phenomenon (Hindman and Jain, 2014; Antolin et al., 2016; Duckenfield et al., 2018), some

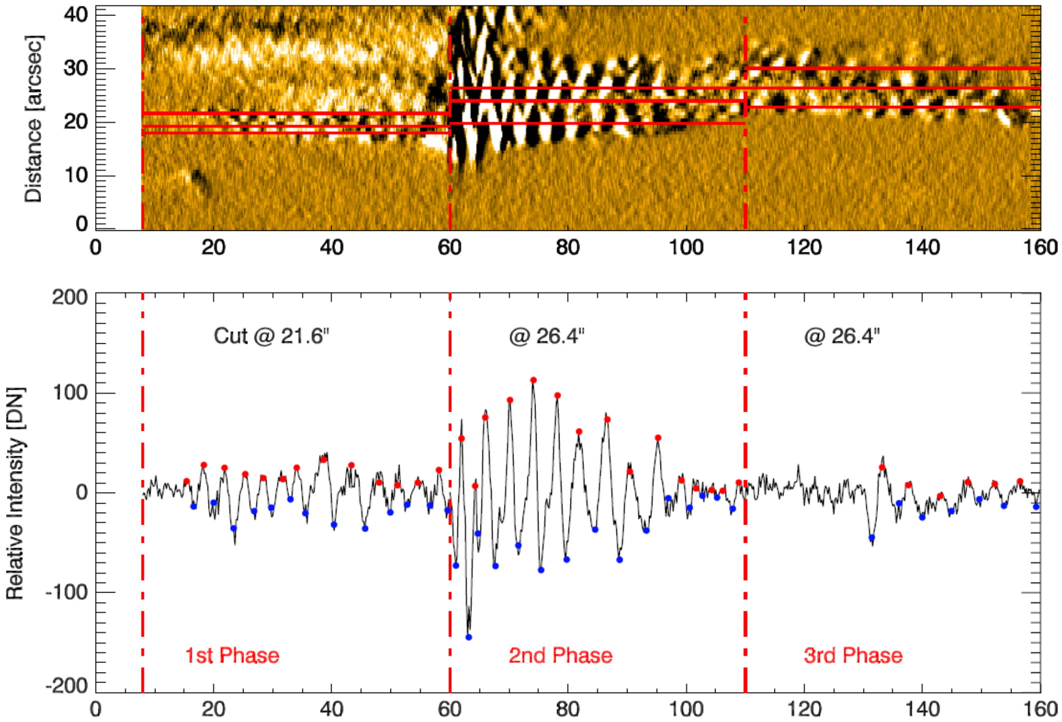

Figure 1.8: The temporal evolution of the displacement of the loop studied in Nisticò et al. (2013).

of which we shall discuss in Chapter 3.

Finally, we should note that it is likely that the magnetic fields of coronal loops exhibit at least some degree of twist (Klimchuk et al., 2000; Malanushenko et al., 2009, 2011). As such, it is important to consider this factor when studying the properties of oscillations and instabilities. This will be especially significant in Chapter 3.

1.5 The Kelvin-Helmholtz Instability

The *Kelvin-Helmholtz instability* (KHI), is a phenomenon resulting from shearing motions of fluids or plasmas, and is a fundamental example of transition from laminar to turbulent flow. It is named after the British and German physicists, William Thomson, 1st Baron Kelvin, and Hermann von Helmholtz, respectively, and was first described in von Helmholtz (1868) and Thomson (1871).

The KHI is present in both hydrodynamics and MHD. It may occur when there is velocity shear in a single fluid, or when there is a difference in velocities over an interface separating two fluids. In hydrodynamical systems, in the absence of surface tension, a boundary separating inviscid immiscible fluids in relative motion is always KH unstable. Introducing surface tension stabilises the boundary and imposes a critical value of the relative flow, below which the system is stable. Similarly, in MHD, the KH instability can develop on the interface separating two plasmas in relative motion. The effect of the magnetic field is potentially significant, and will be discussed in detail in Subsection 1.5.1.

The evolution of the KHI is as follows. When a boundary separating fluids in relative motion is subject to a small perturbation, the shear flow at the interface causes the perturbation to grow in time. The perturbation steepens and becomes nonlinear, and eventually rolls up into a vortex. This succession of phases is represented in Figure 1.9.

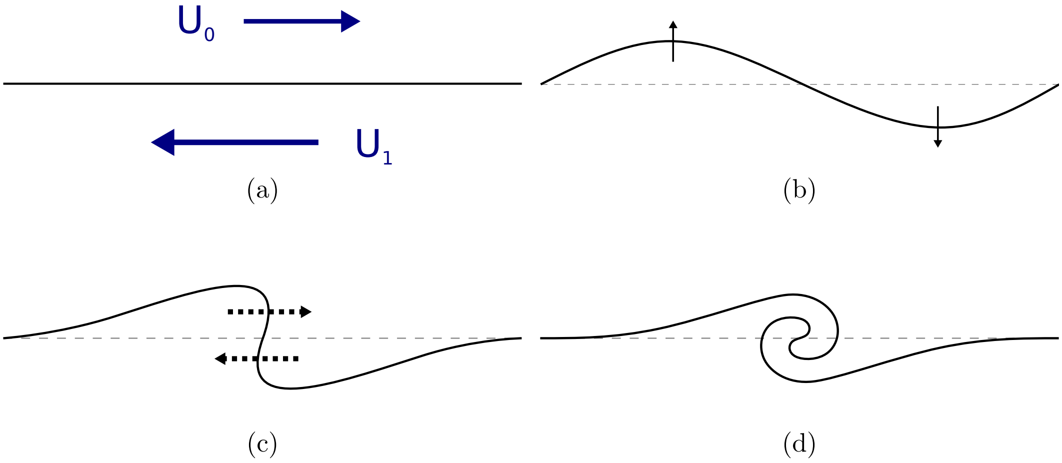

(a) (b)

(c) (d)

Figure 1.9: The stages of a KHI. Suppose that a magnetic interface (a) separating two regions with background flows in opposite directions is subject to a perturbation (b). As the system evolves in time, sufficiently strong flows will amplify the perturbation, causing nonlinear wave steepening (c), until vortex formation occurs (d). Further evolution typically renders the system turbulent.

The KHI may be found in nature in a variety of locations, including the Earth's atmosphere and oceans (Drazin, 2015; Smyth and Moum, 2012), planetary magnetospheres Hasegawa et al. (2004); Masters et al. (2010), interstellar clouds Vietri et al. (1997), supernova remnants Wang and Chevalier (2001), and superfluids (Blaauwgeers et al., 2002) On the Sun, the KHI has thus far been observed in some jets (Kuridze et al., 2016; Bogdanova et al., 2018; Zhelyazkov et al., 2018), and on the flanks of some CMEs (Ofman and Thompson, 2011; Foullon et al., 2011; Möstl et al., 2013). These observations are discussed in Subsection 1.5.2.

1.5.1 The KHI in MHD

Analytical studies of the KHI were performed soon after the formulation of the ideal MHD equations. The linear phase of the instability was analysed in the context of two different equilibrium configurations in Chandrasekhar (1961). In the first case, a tangential interface separates regions of different density, ρ_0 and ρ_1, magnetic field strength $\mathbf{B}_0$ and $\mathbf{B}_1$, and flow, $\mathbf{U}_0$ and $\mathbf{U}_1$. Here, the magnetic fields and flows are parallel to the interface, i.e. $\mathbf{B}_0 \parallel \mathbf{B}_1$, $\mathbf{B}_1 \parallel \mathbf{U}_0$, $\mathbf{U}_0 \parallel \mathbf{U}_1$. It may be shown that the KHI is only triggered if

$$\frac{B_0^2 + B_1^2}{\mu \rho_0 \rho_1}(\rho_0 + \rho_1) \leq (U_0 - U_1)^2. \tag{1.80}$$

This is because perturbations perpendicular to the interface cause the magnetic field parallel to the flow to stretch and produce a restoring force. This effect is similar to how surface tension in hydrodynamics introduces a critical velocity which the background flow needs to surpass in order for the boundary to become KH unstable.

In the second case, the magnetic field is perpendicular to the flows. It may be shown that, in this situation, the magnetic field has no effect and the boundary is immediately unstable to perturbations perpendicular to it. This is because perturbations may no longer stretch the field lines, and no restoring force exists.

In recent years, a multitude of analytical studies of the linear phase of the KHI have been performed to account for different geometries. Nakariakov and Roberts (1995) studied the KHI in the context of a slab embedded in a symmetric environment, and were able to derive the instability criterion in the incompressible limit, similar to Equation (1.80). The results of Nakariakov and Roberts (1995) will be of significance in Chapter 2 for comparison with our own results.

The KHI due to flows along a cylindrical flux tube was first studied by Somasundaram et al. (1999) and Terra-Homem et al. (2003). Subsequently, the KHI in cylindrical flux tubes has been studied analytically in a variety of contexts by Zaqarashvili et al. (2010); Soler et al. (2010); Zhelyazkov and Zaqarashvili (2012); Zaqarashvili, Vörös and Zhelyazkov (2014); Zaqarashvili, Vörös, Narita and Bruno (2014); Zaqarashvili et al. (2015). The studies cited above will be of some significance in Chapter 3 for comparison with our own model.

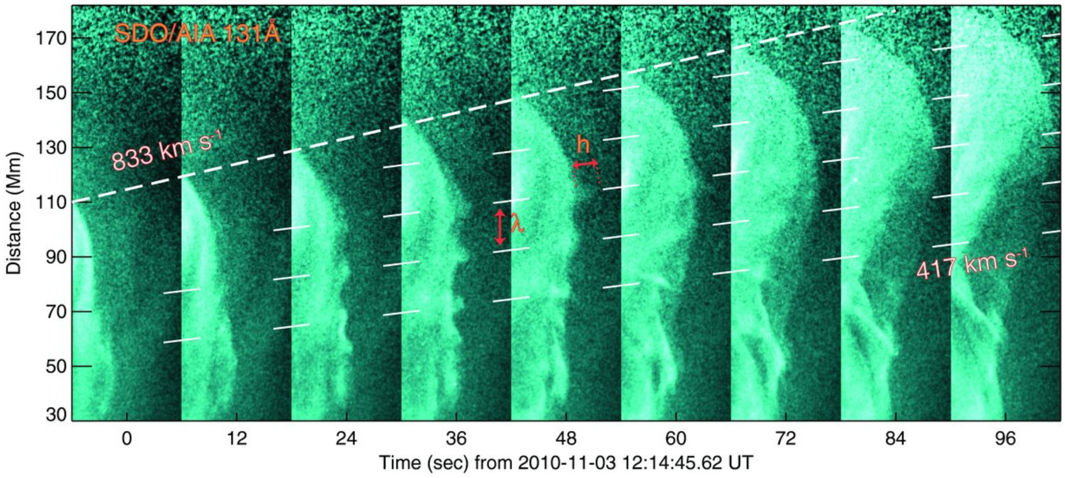

Figure 1.10: A time-distance plot of the KHI observed on the flank of a CME in Foullon et al. (2011). The parameters λ and h correspond to the distance between the KH vortices, and the maximum height of a vortex as measured from the flank, respectively.

1.5.2 The KHI on the Sun

The analytical studies mentioned in Subsection 1.5.2 have generally found that, due to the stabilising effect of a magnetic field parallel to a flow, the KHI is not a common occurrence on large scales in solar observations. Despite this fact, provided flow speeds are strong enough, some observations of the KHI in jets and CMEs have been made.

Of particular interest in this Thesis are the observations of the KHI on the flanks of CMEs (see Figure 1.10). It was suggested by Foullon et al. (2011) and Möstl et al. (2013), that the region on the CME flank where the instability occurs may be modelled as a thin slab in an asymmetric environment. Möstl et al. (2013) demonstrated that by increasing the strength of the magnetic field on one side of the slab, the KHI on that side is inhibited. This numerical study shows that exterior asymmetry is an important factor when considering the physics of magnetic slabs. The observations of Ofman and Thompson (2011); Foullon et al. (2011); Möstl et al. (2013) are further discussed in Chapter 2.

1.6 Outline of Thesis

In this Thesis, we study the stability of two MHD configurations subjected to shear flows, and discuss their applications to solar phenomena. In Chapter 2, we study the steady slab embedded in a static non-magnetic asymmetric environment. Our analysis starts with the derivation of the governing equations for each section of the system, which was omitted in our discussion of a slab in a symmetric environment in Section 1.4. We, then, obtain a dispersion relation for waves propagating along the slab, and some of its approximate solutions. We solve the dispersion relation numerically to obtain general wave solutions and determine the KHI threshold. Finally, we discuss how our model may be used for the seismology of KH unstable CMEs.

In Chapter 3, we study an interface separating time-periodic counter streaming flows. We find that the governing equation for perturbations perpendicular to the interface is Mathieu's equation, and we study its stability. We discuss our findings in the context of applications to the stability of transverse coronal loop oscillations.

CHAPTER 2

Magnetoacoustic Waves and the KHI in a Steady Slab Embedded in an Asymmetric Environment

Abstract

Recent observations have shown that bulk flow motions in structured solar plasmas, most evidently in coronal mass ejections (CMEs), may lead to the formation of Kelvin-Helmholtz instabilities (KHIs). Analytical models are thus essential in understanding both how the flows affect the propagation of magnetohydrodynamic (MHD) waves, and what the critical flow speed is for the formation of the KHI. We investigate both these aspects in a novel way: in a steady magnetic slab embedded in an asymmetric environment. The exterior of the slab is defined as having different equilibrium values of the background density, pressure and temperature on either side. A steady flow and constant magnetic field are present in the slab interior. Approximate solutions to the dispersion relation are obtained analytically and classified with respect to mode and speed. General solutions and the KHI thresholds are obtained numerically. It is shown that, generally, both the KHI critical value and the cut-off speeds for magnetoacoustic waves are lowered by the external asymmetry.

2.1 Introduction

The propagation of linear MHD waves along magnetic slabs has long been a topic of study in the context of solar physics (see Section 1.4). The presence of a steady flow in the equilibrium state of the system affects the propagation in

---

This chapter is based on the following refereed journal article:

- Barbulescu, M., Erdélyi, R. (2018); Magnetoacoustic Waves and the Kelvin-Helmholtz Instability in a Steady Asymmetric Slab. I: The Effects of Varying Density Ratios, *Solar Phys.*, Volume 293, Issue 6

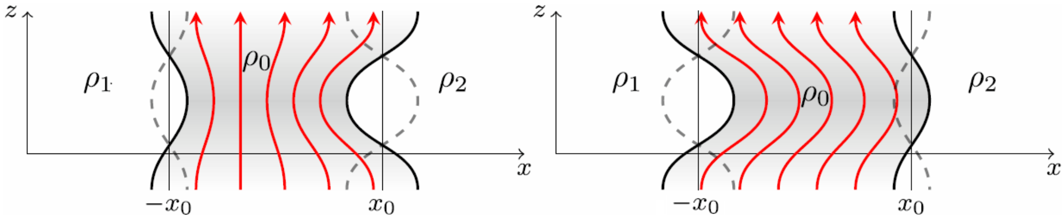

(a) Quasi-sausage (b) Quasi-kink

Figure 2.1: Schematic representation of the quasi-modes of a magnetic slab in an asymmetric non-magnetic environment, as depicted in Allcock and Erdélyi (2017). The densities satisfy $\rho_1 > \rho_2$, the solid red lines represent the perturbed magnetic field, the thick solid black lines represent the perturbed slab boundaries, and the dashed gray lines illustrate the position of the slab boundaries after half a period.

at least two important ways. First, perturbations may cause shearing motions in the flow, which then could lead to the KHI (see Section 1.5). Second, the phase speeds and the cut-off speeds of each mode of propagation are shifted proportional to the speed of the flow (Nakariakov and Roberts, 1995; Terra-Homem et al., 2003). Interactions between propagating waves and flows are not limited to these two instances though. Other areas of study include negative energy wave instabilities, if dissipative effects are taken into account (Cairns, 1979; Joarder et al., 1997), or resonant flow instabilities, if the dissipation is due to resonant absorption (see Tirry et al., 1998; Taroyan and Erdélyi, 2002). More information on the above topics may be found in Taroyan and Ruderman (2011) and Ryutova (2015).

The effects of steady flows have been investigated in a number of different waveguide geometries and magnetic topologies. Nakariakov and Roberts (1995) studied the effect of a steady flow in an infinite slab of magnetised plasma in a magnetic environment. Terra-Homem et al. (2003) then explored the effects that a steady flow has on the propagation of both linear and nonlinear waves in a straight infinite cylindrical flux tube. This latter work expanded on the analysis of Somasundaram et al. (1999). For a more general approach to analysing the stability of steady MHD flows see, for example, Goedbloed (2009*a*,*b*, 2018*a*,*b*).

More recently, Soler et al. (2010) described the effects of an azimuthally dependent flow on the stability of a straight flux tube, while Zaqarashvili, Vörös and Zhelyazkov (2014) investigated the stability of an incompressible, twisted cylindrical flux tube, subject to a straight flow, in a magnetic environment. Finally, Zaqarashvili et al. (2015) studied the stability of an incompressible, rotating, and twisted cylinder. The theoretical results of the latter two works were applied in Kuridze et al. (2016) to determine the stability of chromospheric jets, and to estimate the growth time of the KHI.

Recent observational results have reinforced the idea that plasma flows are present throughout the solar atmosphere. Berger et al. (2010) and Ryutova et al. (2010) uncovered details about mass flows and the formation of the KHI in solar prominences. KHI formation in the corona has also received considerable attention (see Foullon et al., 2011; Ofman and Thompson, 2011; Foullon et al., 2013). For a recent review, see Zhelyazkov (2015).

Of significant interest are the observations by Foullon et al. (2011) of a KHI on the flank of a CME. The authors interpret the system's configuration as consisting of three regions: the dense solar ejecta, the CME sheath, and the low density corona, with the KHI occurring in the region between the ejecta sheath and the corona. A similar three layer system is described by Möstl et al. (2013). By interpreting the CME boundary as a steady magnetic slab embedded in an asymmetric magnetic environment, the authors demonstrated that through increasing the magnetic field strength on only one side of the slab, it provided a stabilising effect there only. This numerical study shows that exterior asymmetry may be an important factor when considering the physics of magnetic slabs.

The magnetic slab embedded in an asymmetric environment, has recently been studied by a number of authors. Allcock and Erdélyi (2017) derived the dispersion relation of waves propagating along a magnetic slab embedded in a non-magnetic environment, in the absence of flows, while Allcock and Erdélyi (2018) showcased a number of applications of the model to helioseismology. Zsámberger et al. (2018) expanded upon the model of Allcock and Erdélyi (2017) by including asymmetric magnetic fields in the environment outside the slab. Finally, Barbulescu and Erdélyi (2018) derived the dispersion relation of waves propagating along a steady magnetic slab embedded in a non-magnetic environment and studied the impact of the density asymmetry upon the KHI threshold value. Also of significance is the finding of Allcock and Erdélyi (2017) that the modes of wave propagation along a magnetic slab in an asymmetric environment do not decouple into the well known sausage and kink modes. Rather, the modes are asymmetric and are better labelled as quasi-sausage and quasi-kink modes (see Figure 2.1).

In this Chapter, we expand upon the results in Barbulescu and Erdélyi (2018) concerning the effects that a steady flow within the slab has on the propagation of magnetoacoustic waves, and on how the asymmetry affects the KHI threshold values. In Section 2.2, we derive the dispersion relation for waves propagating along the slab from the ideal compressible MHD equations, and classify the modes in terms of the characteristic speeds of the system. In Section 2.3, we obtain approximate solutions to the dispersion relation using the thin slab approximation, wide slab approximation and incompressible limit. In Section 2.4, we obtain general numerical solutions to the dispersion relation, as well as values for the KHI threshold in different parameter regimes. Section 2.5 contains an application of the described model with regard to estimating the magnetic field strength in a CME. Finally, Section 2.6 contains a summary and discussion of the results in the previous Sections.

2.2 The Dispersion Relation

We introduce a slab of plasma bounded by two interfaces at $\pm x_0$, of density, pressure, and temperature ρ_0, p_0, and T_0 respectively, and magnetic field $\mathbf{B}_0 = (0, 0, B_0)$, which is subject to a steady flow $\mathbf{U}_0 = (0, 0, U_0)$. The slab is embedded in an asymmetric environment, defined as having density, pressure, and temperature ρ_1, p_1 and T_1 on the left side, and ρ_2, p_2, and T_2, on the right side, as illustrated in Figure 2.2. The exterior is neither subject to magnetic fields, nor to flows. It follows that the fluid in the interior region of the slab is governed by the ideal MHD equations, while the exterior regions are described using the gas equations.

2.2.1 Governing Equation for the Interior

We wish to obtain a governing equation describing the propagation of linear magnetoacoustic waves along the parallel interfaces. For this purpose, we employ the compressible ideal linear MHD equations, introduced in Subsection

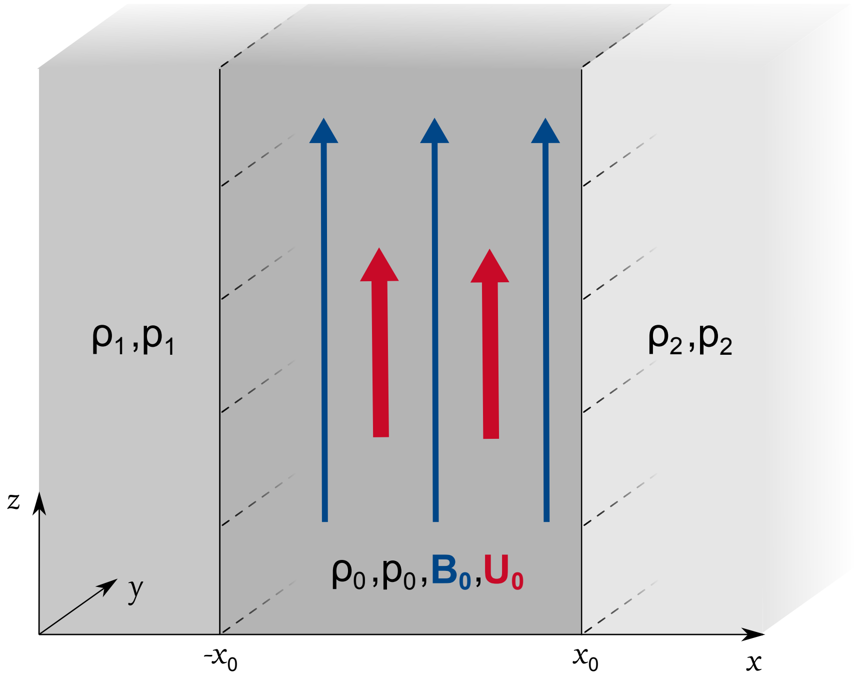

Figure 2.2: The steady magnetic slab embedded in a static asymmetric non-magnetic environment.

1.3.6, subject to the previously defined background conditions,

$$\frac{\mathrm{D}\rho}{\mathrm{D}t} + \rho_0 \nabla \cdot \mathbf{v} = 0, \tag{2.1}$$

$$\rho_0 \frac{\mathrm{D}\mathbf{v}}{\mathrm{D}t} = -\nabla\left(p + \frac{B_0}{\mu} b_z\right) + \frac{B_0}{\mu}\frac{\partial \mathbf{b}}{\partial z}, \tag{2.2}$$

$$\frac{\mathrm{D}p}{\mathrm{D}t} = c_0^2 \frac{\mathrm{D}\rho}{\mathrm{D}t}, \tag{2.3}$$

$$\frac{\mathrm{D}\mathbf{b}}{\mathrm{D}t} = -\mathbf{B}_0(\nabla \cdot \mathbf{v}) + B_0 \frac{\partial \mathbf{v}}{\partial z}, \tag{2.4}$$

$$\nabla \cdot \mathbf{b} = 0.$$

Here, $\rho, p, \mathbf{b} = (b_x, b_y, b_z)$, and $\mathbf{v} = (v_x, v_y, v_z)$ are small perturbations from the equilibrium, and

$$\frac{\mathrm{D}}{\mathrm{D}t} = \frac{\partial}{\partial t} + U_0 \frac{\partial}{\partial z}$$

is the material derivative, and the sound speed is defined as $c_0^2 = \gamma p_0/\rho_0$. Equations (2.1) - (2.4) are only valid for the interior of the slab.

Since we are only concerned with magnetoacoustic waves propagating along the slab, we may disregard all dependence on the y-component without loss of generality. Equations (2.1) - (2.4) may, thus, be written as

$$\rho_0 \frac{\mathrm{D}v_x}{\mathrm{D}t} = -\frac{\partial}{\partial x}\left(p + \frac{B_0}{\mu_0} b_z\right) + \frac{B_0}{\mu_0}\frac{\partial b_x}{\partial z}, \tag{2.5}$$

$$\rho_0 \frac{\mathrm{D}v_z}{\mathrm{D}t} = -\frac{\partial p}{\partial z}, \tag{2.6}$$

$$\frac{\mathrm{D}p}{\mathrm{D}t} = -c_0^2 \rho_0 \nabla \cdot \mathbf{v}, \tag{2.7}$$

$$\frac{\mathrm{D}b_x}{\mathrm{D}t} = B_0 \frac{\partial v_x}{\partial z}, \tag{2.8}$$

$$\frac{\mathrm{D}b_z}{\mathrm{D}t} = -B_0 \frac{\partial v_x}{\partial x}. \tag{2.9}$$

Here, Equations (2.5) and (2.6) are the $x-$ and $z-$components of the momentum equation, Equation (2.7) is the result of combining Equations (2.1) and (2.3), and Equations (2.8) and (2.9) are the $x-$ and $z-$components of the induction equation.

Let us Fourier decompose Equations (2.5) - (2.9) for waves propagating along the slab by assuming that $f(\mathbf{r}, t) = \hat{f}(x)\mathrm{e}^{i(kz-\omega t)}$, where f stands for any of the small perturbations, and $\hat{f}$ is the amplitude of each perturbation. Here, ω is the angular frequency, and k is the wavenumber in the z-direction. This procedure allows us to remove all differential terms in the linearised MHD equation, except for derivatives with respect to x, much like in Section 1.4. Equations (2.5) - (2.9) become

$$i\rho_0 \Omega \hat{v}_x = \frac{\mathrm{d}}{\mathrm{d}x}\left(\hat{p} + \frac{B_0}{\mu_0}\hat{b}_z\right) - ik\frac{B_0}{\mu_0}\hat{b}_x, \tag{2.10}$$

$$\rho_0 \Omega \hat{v}_z = k\hat{p}, \tag{2.11}$$

$$\Omega \hat{p} = c_0^2 \rho_0 (-i\frac{\mathrm{d}\hat{v}_x}{\mathrm{d}x} + k\hat{v}_z), \tag{2.12}$$

$$\Omega \hat{b}_x = -B_0 k \hat{v}_x, \tag{2.13}$$

$$i\Omega \hat{b}_z = B_0 \frac{\mathrm{d}\hat{v}_x}{\mathrm{d}x}, \tag{2.14}$$

where $\Omega = \omega - kU_0$ is the Doppler-shifted frequency.

In order to obtain a governing equation for the interior of the slab, we must combine Equations (2.10) - (2.14) so that we eliminate all but one dependent variable. While the governing equation may be written in terms of any of the dependent variables, we choose $\hat{v}_x(x)$ since it is most convenient. We begin by combining Equations (2.11) and (2.12) in order to eliminate $\hat{v}_z$, and obtain

$$\hat{p} = i\frac{\Omega c_0^2 \rho_0}{k^2 c_0^2 - \Omega^2}\frac{\mathrm{d}\hat{v}_x}{\mathrm{d}x}. \tag{2.15}$$

We then introduce Equation (2.13) into Equation (2.10), in order to eliminate $\hat{b}_x$,

$$(k^2 v_A^2 - \Omega^2)\hat{v}_x = -\frac{i\Omega}{\rho_0}\frac{\mathrm{d}}{\mathrm{d}x}\left(\hat{p} + \frac{B_0}{\mu_0}\hat{b}_z\right), \tag{2.16}$$

where the Alfvén speed, v_A, is defined as

$$v_A^2 = \frac{B_0^2}{\mu_0 \rho_0},$$

similar to Equation 1.35. Substituting Equation (2.14) into (2.16), we obtain

$$(k^2 v_A^2 - \Omega^2)\hat{v}_x = -\frac{i\Omega}{\rho_0}\frac{\mathrm{d}\hat{p}}{\mathrm{d}x} - v_A^2\frac{\mathrm{d}^2\hat{v}_x}{\mathrm{d}x^2}. \tag{2.17}$$

Finally, we combine Equations (2.15) and (2.17) such that, except for $\hat{v}_x$, all other perturbed quantities have been eliminated, leaving us with the governing equation for the velocity amplitude:

$$\frac{\mathrm{d}^2\hat{v}_x}{\mathrm{d}x^2} - m_0^2\hat{v}_x = 0, \tag{2.18}$$

where

$$m_0^2 = \frac{(k^2 v_A^2 - \Omega^2)(k^2 c_0^2 - \Omega^2)}{(c_0^2 + v_A^2)(k^2 c_T^2 - \Omega^2)}, \tag{2.19}$$

and the tube speed, c_T, is defined as

$$c_T^2 = \frac{c_0^2 v_A^2}{c_0^2 + v_A^2}.$$

similar to Equation (1.67)

2.2.2 Governing Equations for the Exterior

The same scheme that was used in Subsection 2.2.1 may be applied to the exterior layers, with the consideration that, in both semi-infinite layers, there are no magnetic fields or flows present. These regions are, therefore, governed by the gas equations,

$$\frac{\partial \rho}{\partial t} + \rho_j \nabla \cdot \mathbf{v} = 0, \tag{2.20}$$

$$\rho_j \frac{\partial \mathbf{v}}{\partial t} = -\nabla p, \tag{2.21}$$

$$\frac{\partial p}{\partial t} = c_j^2 \frac{\partial \rho}{\partial t}, \tag{2.22}$$

where the subscript j is either 1, for $x < -x_0$, or 2, for $x > x_0$, and the exterior sound speeds are defined as $c_j^2 = \gamma p_j/\rho_j$. Substituting Equation (2.20) into (2.22) yields

$$\frac{\partial p}{\partial t} = -c_j^2 \rho_j \nabla \cdot \mathbf{v}. \tag{2.23}$$

We differentiate Equation (2.20) with respect to t, and combine it with Equation (2.23), such that

$$\frac{\partial^2 \mathbf{v}}{\partial t^2} - c_j^2 \nabla(\nabla \cdot \mathbf{v}) = 0. \tag{2.24}$$

Equation (2.24) may be written in component form

$$\frac{\partial^2 v_x}{\partial t^2} - c_j^2 \left(\frac{\partial^2 v_x}{\partial x^2} + \frac{\partial^2 v_z}{\partial x \partial z} \right) = 0, \tag{2.25}$$

$$\frac{\partial^2 v_z}{\partial t^2} - c_j^2 \left(\frac{\partial^2 v_x}{\partial x \partial z} + \frac{\partial^2 v_z}{\partial z^2} \right) = 0, \tag{2.26}$$

and Fourier decomposed $\sim \mathrm{e}^{i(kz-\omega t)}$,

$$\omega^2 \hat{v}_x + c_j^2 \left(\frac{\mathrm{d}^2 \hat{v}_x}{\mathrm{d}x^2} + ik \frac{\mathrm{d}\hat{v}_z}{\mathrm{d}x} \right) = 0, \tag{2.27}$$

$$\omega^2 \hat{v}_z + c_j^2 \left(ik \frac{\mathrm{d}\hat{v}_x}{\mathrm{d}x} - k^2 \hat{v}_z \right) = 0. \tag{2.28}$$

By rearranging Equation (2.28) as

$$\hat{v}_z = -\frac{ikc_j^2}{\omega^2 - k^2 c_j^2} \frac{\mathrm{d}\hat{v}_x}{\mathrm{d}x}, \tag{2.29}$$

and substituting Equation (2.29) into Equation (2.27), the governing equations for the outer layers is obtained,

$$\frac{\mathrm{d}^2 \hat{v}_x}{\mathrm{d}x^2} - m_j^2 \hat{v}_x = 0, \tag{2.30}$$

where

$$m_j^2 = k^2 - \frac{\omega^2}{c_j^2}. \tag{2.31}$$

Equations (2.18) and (2.30) are analogous, as are Equations (2.19) and (2.31). By removing all terms dependent on the magnetic field from Equations (2.18) and (2.19), we obtain Equations of the form of (2.30) and (2.31), respectively.

Fourier decomposing Equation (2.23) yields

$$i\omega \hat{p} = c_j^2 \rho_j \left(\frac{\mathrm{d}\hat{v}_x}{\mathrm{d}x} + ik\hat{v}_z \right), \tag{2.32}$$

which, after substituting Equation (2.29) into Equation (2.32), becomes

$$\hat{p} = i\frac{\omega\rho_j}{m_j^2}\frac{\mathrm{d}\hat{v}_x}{\mathrm{d}x}. \tag{2.33}$$

Equation (2.33) relates the exterior gas pressure perturbation amplitude to the velocity perturbation amplitude perpendicular to the interface, and will be of use later in the derivation.

2.2.3 Boundary Conditions and Dispersion Relation

In order to find trapped wave solutions to Equations (2.18) and (2.30), we require that solutions to Equations (2.30) be evanescent, i.e. that all perturbations vanish at $\pm\infty$. This implies that $m_j^2 > 0$ is required for $j = 1, 2$. The solutions to Equations (2.18) and (2.30) may, therefore, be written as

$$\hat{v}_{xj}(x) = \begin{cases} A(\cosh m_1 x + \sinh m_1 x), & x < -x_0, \\ B\cosh m_0 x + C\sinh m_0 x, & |x| \leq x_0, \\ D(\cosh m_2 x - \sinh m_2 x), & x > x_0, \end{cases} \tag{2.34}$$

where A, B, C, and D are arbitrary constants. By inspection, we establish that two wave modes are allowed to propagate under the given constraints: one that is evanescent towards the center of the slab (for $m_0^2 > 0$), and one that is spatially oscillatory throughout the slab (for $m_0^2 < 0$). These modes of propagation are the so-called surface and body modes, respectively, which were introduced in Section 1.4.

Equation (2.34) is subject to boundary conditions at the interfaces, namely, the continuity of the Lagrangian displacement, and the continuity of total pressure:

$$\begin{aligned} \frac{\hat{v}_{x1}(x=-x_0)}{\omega} &= \frac{\hat{v}_{x0}(x=-x_0)}{\Omega}, \\ \frac{\hat{v}_{x2}(x=x_0)}{\omega} &= \frac{\hat{v}_{x0}(x=x_0)}{\Omega}, \\ [p_T]_{x=-x_0} &= 0, \\ [p_T]_{x=x_0} &= 0. \end{aligned} \tag{2.35}$$

Here, the total pressure is the sum of the gas and magnetic pressures, where the gas pressures are defined in Equations (2.15), and (2.33). Since there is no magnetic field in the exterior regions, the total pressure is simply the gas pressure. In order to calculate the magnetic pressure within the slab, we make use of its definition from Equation (1.31). Since the quantities in Equation (1.31) are nonlinear, we first linearise them, and obtain

$$\begin{aligned} p_m = \frac{\mathbf{B}^2}{2\mu} &= \frac{1}{2\mu_0}(\mathbf{B}_0^2 + 2\mathbf{B}_0 \cdot \mathbf{b} + \mathbf{b}^2) \\ &\approx \frac{\mathbf{B}_0 \cdot \mathbf{b}}{\mu_0} = \frac{B_0 b_z}{\mu_0}, \end{aligned} \tag{2.36}$$

where p_m is the magnetic pressure. The terms $\mathbf{B}_0^2$ and $\mathbf{b}^2$ in Equation (2.36) vanish since we only keep the terms of order of the perturbations, i.e. p_m and $\mathbf{B}_0 \cdot \mathbf{b}$. We Fourier decompose Equation (2.36),

$$\hat{p}_m = \frac{B_0 \hat{b}_z}{\mu_0}, \tag{2.37}$$

and substitute Equation (2.14) into Equation (2.37) to obtain

$$\hat{p}_m = -i\frac{v_A^2 \rho_0}{\Omega}\frac{\mathrm{d}\hat{v}_x}{\mathrm{d}x}. \tag{2.38}$$

Combining Equations (2.15), (2.33), and (2.38), we find that the total pressure is

$$\hat{p}_T(x) = \frac{\mathrm{d}\hat{v}_x}{\mathrm{d}x} \begin{cases} \dfrac{i\rho_1\omega}{m_1^2}, & x < -x_0, \\ -\dfrac{i\rho_0(k^2 v_A^2 - \Omega^2)}{m_0^2 \Omega}, & |x| \leq x_0, \\ \dfrac{i\rho_2\omega}{m_2^2}, & x > x_0. \end{cases} \tag{2.39}$$

Using Equations (2.34) and (2.39), we may write the boundary conditions, (2.35), as a system of four simultaneous homogeneous algebraic equations,

$$\begin{aligned} A(\cosh m_1 x_0 - \sinh m_1 x_0) - B\frac{\omega}{\Omega}\cosh m_0 x_0 + C\frac{\omega}{\Omega}\sinh m_0 x_0 &= 0, \\ B\frac{\omega}{\Omega}\cosh m_0 x_0 + C\frac{\omega}{\Omega}\sinh m_0 x_0 + D(\sinh m_2 x_0 - \cosh m_2 x_0) &= 0, \\ A\Lambda_1(\cosh m_1 x_0 - \sinh m_1 x_0) - B\Lambda_0 \sinh m_0 x_0 + C\Lambda_0 \cosh m_0 x_0 &= 0, \\ -B\Lambda_0 \sinh m_0 x_0 - C\Lambda_0 \cosh m_0 x_0 + D\Lambda_2(\cosh m_2 x_0 - \sinh m_2 x_0) &= 0, \end{aligned} \tag{2.40}$$

where

$$\begin{aligned}\Lambda_0 &= \frac{i\rho_0\left(k^2v_A^2-\Omega^2\right)}{m_0\Omega},\\ \Lambda_1 &= \frac{i\rho_1\omega}{m_1},\\ \Lambda_2 &= \frac{i\rho_2\omega}{m_2}.\end{aligned}\tag{2.41}$$

Equations (2.40) may be written in matrix form as

$$\begin{pmatrix} c_1-s_1 & -\frac{\omega}{\Omega}c_0 & \frac{\omega}{\Omega}s_0 & 0\\ 0 & \frac{\omega}{\Omega}c_0 & \frac{\omega}{\Omega}s_0 & s_2-c_2\\ \Lambda_1(c_1-s_1) & -\Lambda_0s_0 & \Lambda_0c_0 & 0\\ 0 & -\Lambda_0s_0 & -\Lambda_0c_0 & \Lambda_2(c_2-s_2)\end{pmatrix}\begin{pmatrix}A\\B\\C\\D\end{pmatrix}=\begin{pmatrix}0\\0\\0\\0\end{pmatrix},\tag{2.42}$$

where, for brevity, we introduced $c_j = \cosh m_jx_0$, $s_j = \sinh m_jx_0$, for $j = 0,1,2$. We denote the matrix in Equation (2.42) as M_0 and row reduce it to obtain

$$M_1=\begin{pmatrix} c_1-s_1 & -\frac{\omega}{\Omega}c_0 & \frac{\omega}{\Omega}s_0 & 0\\ 0 & \frac{\omega}{\Omega}c_0 & \frac{\omega}{\Omega}s_0 & s_2-c_2\\ 0 & -\Lambda_0s_0+\Lambda_1\frac{\omega}{\Omega}c_0 & \Lambda_0c_0-\Lambda_1\frac{\omega}{\Omega}s_0 & 0\\ 0 & 0 & \Lambda & 0\end{pmatrix},\tag{2.43}$$

where

$$\begin{aligned}\Lambda = {}&\left(\Lambda_0s_0-\Lambda_1c_0\omega/\Omega\right)\left(\Lambda_0c_0-\Lambda_2s_0\omega/\Omega\right)\\ &+\left(\Lambda_0c_0-\Lambda_1s_0\omega/\Omega\right)\left(\Lambda_0s_0-\Lambda_2c_0\omega/\Omega\right).\end{aligned}\tag{2.44}$$

For the system of Equations (2.40) to have non-trivial solutions, we require the determinant of M_0 to be equal to zero. We may write the determinant of M_0 as

$$\begin{aligned}\det M_0 &= \left(-\Lambda_0s_0+\Lambda_1c_0\omega/\Omega\right)^{-1}\det M_1\\ &= (c_1-s_1)(s_2-c_2)\Lambda.\end{aligned}\tag{2.45}$$

It follows that the system of Equations (2.40) has non-trivial solutions if $\Lambda = 0$. Explicitly, this may be written as

$$\begin{aligned}&\left(\Lambda_0s_0-\Lambda_1c_0\omega/\Omega\right)\left(\Lambda_0c_0-\Lambda_2s_0\omega/\Omega\right)+\\ &\left(\Lambda_0c_0-\Lambda_1s_0\omega/\Omega\right)\left(\Lambda_0s_0-\Lambda_2c_0\omega/\Omega\right)=0,\end{aligned}\tag{2.46}$$

which, after some algebra, becomes

$$2\left(\Lambda_0^2+\Lambda_1\Lambda_2\frac{\omega^2}{\Omega^2}\right)-\Lambda_0(\Lambda_1+\Lambda_2)\frac{\omega}{\Omega}(\tanh m_0x_0+\coth m_0x_0)=0. \tag{2.47}$$

Substituting Equation (2.41) into Equation (2.47) yields

$$\begin{aligned} m_0^2\omega^4 &+ \frac{\rho_0}{\rho_1}m_1\frac{\rho_0}{\rho_2}m_2(k^2v_A^2-\Omega^2)^2 \\ &- \frac{1}{2}m_0\omega^2(k^2v_A^2-\Omega^2)\left(\frac{\rho_0}{\rho_1}m_1+\frac{\rho_0}{\rho_2}m_2\right)(\tanh m_0x_0+\coth m_0x_0)=0. \end{aligned} \tag{2.48}$$

Equation (2.48) is the dispersion relation for the propagation of magnetoacoustic waves in a steady magnetic slab embedded in an asymmetric non-magnetic environment. It is a generalization of the dispersion relation for waves propagating along a static slab in a non-magnetic asymmetric environment (Allcock and Erdélyi, 2017). The dispersion relation of Allcock and Erdélyi (2017) may be immediately recovered by removing the background flow, i.e. setting $U_0=0$. Equation (2.48) is also related to the dispersion relation found in Nakariakov and Roberts (1995) for the propagation of waves in a steady slab embedded in a magnetic environment. If we consider the model of Nakariakov and Roberts (1995) with no exterior magnetic field, we obtain the same result as when considering Equation (2.48) with equal exterior densities.

2.2.4 Comparison with Previous Models

Due to the fact that the properties of magnetoacoustic waves propagating along a slab in a symmetric environment are qualitatively different from those propagating along a slab in an asymmetric environment, it is useful to compare Equation (2.48) to the dispersion relations of other similar models.

The dispersion relation for magnetoacoustic waves propagating along a slab in a symmetric environment, Equation (1.74), was described in the previous Chapter. Equation (1.74) has two sets of solutions: oscillations which are symmetric about $x=0$ (called sausage modes), and oscillations which are anti-symmetric about $x=0$ (called kink modes). The sausage modes are described by the tanh variant of Equation (1.74), while the kink modes are described by the coth variant.

In contrast, Equation (2.48) describes two modes of oscillation which are not fully independent. Equation (2.48) does not factorise into an equation containing tanh and one containing coth, rather each hyperbolic function has a contribution in determining the solution.

It may be shown that, if the exterior densities only differ by a constant $\alpha \ll 1$, Equation (2.47) factorizes into two equations, one describing the quasi-kink mode and one the quasi-sausage. We first note that, since the total pressure must be continuous at the boundaries, the exterior pressures are equal, i.e. $p_1 = p_2$. It follows that, if $\rho_2 = \rho_1 + \alpha$, then

$$m_2^2 = m_1^2 - \frac{\omega^2}{c_1^2 \rho_1}\alpha, \tag{2.49}$$

and

$$\Lambda_2 = \Lambda_1 + i\omega \frac{c_2^2 + \omega^2/m_2^2}{c_2^2 m_2^2}\alpha. \tag{2.50}$$

We introduce $\epsilon \ll 1$, such that $\Lambda_2 = \Lambda_1 + \epsilon$ and we introduce the fraction

$$\begin{aligned} \frac{(\Lambda_1+\Lambda_2)^2}{4\Lambda_1\Lambda_2} &= \frac{(2\Lambda_1+\epsilon)^2}{\Lambda_1^2(1+\epsilon/\Lambda_1)} \\ &= \frac{1}{4\Lambda_1^2}(4\Lambda_1^2 + 4\epsilon\Lambda_1 + \epsilon^2)(1 - \epsilon/\Lambda_1 + \mathcal{O}(\epsilon^2)) \\ &= \frac{1}{4\Lambda_1^2}(4\Lambda_1^2 + 4\epsilon\Lambda_1 - 4\epsilon\Lambda_1 + \mathcal{O}(\epsilon^2)). \end{aligned} \tag{2.51}$$

Discarding terms of $\mathcal{O}(\epsilon^2)$ and higher in Equation (2.51), we obtain

$$\frac{(\Lambda_1+\Lambda_2)^2}{4\Lambda_1\Lambda_2} \approx 1. \tag{2.52}$$

This allows us to write Equation (2.47) as

$$2\left(\Lambda_0^2 \frac{(\Lambda_1+\Lambda_2)^2}{4\Lambda_1\Lambda_2} + \Lambda_1\Lambda_2\frac{\omega^2}{\Omega^2}\right) - \Lambda_0(\Lambda_1+\Lambda_2)\frac{\omega}{\Omega}(\tanh m_0x_0 + \coth m_0x_0) = 0. \tag{2.53}$$

Multiply Equation (2.53) by $\Lambda_1\Lambda_2$ and factorise it such that we obtain two equations,

$$\begin{aligned} \Lambda_0(\Lambda_1+\Lambda_2) + 2\Lambda_1\Lambda_2 \tanh m_0x_0 &= 0, \\ \Lambda_0(\Lambda_1+\Lambda_2) + 2\Lambda_1\Lambda_2 \coth m_0x_0 &= 0, \end{aligned} \tag{2.54}$$

or, using a more familiar format,

$$\begin{aligned} \rho_0(k^2v_A^2 - \omega^2)\left(\frac{m_1}{\rho_1} + \frac{m_2}{\rho_2}\right) + 2m_0\omega\Omega \tanh m_0x_0 &= 0, \\ \rho_0(k^2v_A^2 - \omega^2)\left(\frac{m_1}{\rho_1} + \frac{m_2}{\rho_2}\right) + 2m_0\omega\Omega \coth m_0x_0 &= 0. \end{aligned} \tag{2.55}$$

Equations (2.55) are a generalization of the factorised dispersion relation of waves propagating along a static slab in a non-magnetic asymmetric environment, first described in Allcock and Erdélyi (2017).

2.2.5 Mode Classification

Information about the nature of the wave solutions may be obtained from the parameters of the dispersion relation, Equation (2.48). We have already established that in order for waves to be trapped, the exterior parameters m_1^2 and m_2^2 must be positive. Modes that do not meet this condition are referred to as leaky and are excluded from the analysis in the present work. As in Chapter 1, we operate in terms of the phase speed, $c_{ph} = \omega/k$, and deduce that for modes to be trapped they must satisfy

$$\max(-c_1, -c_2) < c_{ph} < \min(c_1, c_2). \tag{2.56}$$

It is also worth noting that the sign of the phase speed, c_{ph}, determines whether modes are forward or backward propagating, a positive sign corresponding to the former, and a negative to the latter.

The parameter m_0^2 offers a means of classifying the general solutions to Equation (2.48), which will later be obtained numerically. We have already established that surface modes satisfy the condition $m_0^2 > 0$, while body modes require $m_0^2 < 0$. We may therefore categorize all solutions to equation (2.48) with respect to the signs of c_{ph}, m_0^2, m_1^2, and m_2^2. Solutions that satisfy

$$\max(c_0, v_A) < |c_{ph} - U_0| < \min(c_1 - U_0, c_2 - U_0) \tag{2.57}$$

are fast surface or body modes, depending on the sign of m_0^2, which is determined by the ordering of the characteristic speeds. Slow body and surface modes have phase speeds within the interval

$$c_T < |c_{ph} - U_0| < \min(c_0, v_A), \tag{2.58}$$

and

$$|c_{ph} - U_0| < c_T, \tag{2.59}$$

respectively.

2.3 Approximate Analytical Solutions

The dispersion relation, Equation (2.48) is insoluble analytically (to the best of our knowledge), without the use of simplifying approximations. In this Section, we use a number of analytical approximations to obtain explicit solutions to Equation (2.48). We consider the *thin-slab*, *wide-slab*, and *incompressible* approximations. These approximate analytical solutions will be used to confirm that the numerical solutions obtained in section 2.4 are correct, while also helping to interpret the results in 2.5.

2.3.1 Incompressible Limit

We consider the dispersion relation, Equation (2.48), in the incompressible limit, where $\gamma \to \infty$. Using this approximation, the sound speeds in all sections of the system are unbounded, and the tube speed behaves like $c_T \to v_A$. The effective wavenumbers satisfy $m_j \to k$ for $j = 0, 1, 2$, so that Equation (2.48) reduces to

$$\begin{aligned} \omega^4 + \frac{\rho_0^2}{\rho_1\rho_2}(k^2v_A^2 - \Omega^2)^2 \\ - \frac{1}{2}\omega^2(k^2v_A^2 - \Omega^2)\left(\frac{\rho_0}{\rho_1} + \frac{\rho_0}{\rho_2}\right)(\tanh kx_0 + \coth kx_0) = 0. \end{aligned} \tag{2.60}$$

Since Equation (2.60) is still insoluble analytically, we require an additional approximation. We introduce the phase speed normalised with respect to the Alfvén speed

$$\bar{c}_{ph} = \frac{c_{ph}}{v_A}, \tag{2.61}$$

and the Alfvén Mach number,

$$M_A = \frac{U_0}{v_A}, \tag{2.62}$$

and assume that $c_{ph} \gg U_0$, or equivalently, $\bar{c}_{ph} \gg M_A$. Equation (2.60) becomes a quadratic equation in $\bar{c}_{ph}$,

$$\bar{c}_{ph}^4 + \frac{\rho_0^2}{\rho_1\rho_2}(1 - \bar{c}_{ph}^2)^2 - \frac{1}{2}\bar{c}_{ph}^2(1 - \bar{c}_{ph}^2)\left(\frac{\rho_0}{\rho_1} + \frac{\rho_0}{\rho_2}\right)(\tanh kx_0 + \coth kx_0) = 0. \tag{2.63}$$

Equation (2.63) has solutions given by

$$\begin{aligned} \bar{c}_{ph}^2 &= \frac{2 + \sigma \pm \sqrt{\sigma^2 - \dfrac{4\rho_1\rho_2}{\rho_0^2}}}{2\left(1 + \sigma + \dfrac{\rho_1\rho_2}{\rho_0^2}\right)}, \\ \sigma &= \frac{1}{2}\left(\frac{\rho_1}{\rho_0} + \frac{\rho_2}{\rho_0}\right)(\tanh kx_0 + \coth kx_0). \end{aligned} \tag{2.64}$$

An equation analogous to Equation (2.64) was previously obtained by Allcock and Erdélyi (2017) in the context of a model of a static slab embedded in an asymmetric non-magnetic environment.

2.3.2 Thin-slab Approximation

We assume that the wavelength of the propagating wave solution is much longer than the width of the slab, i.e. that $kx_0 \ll 1$. This is called the long-wavelength approximation, or thin-slab approximation. For surface modes, we may assume that $m_0 x_0 \to 0$ as $kx_0 \to 0$ and, hence, that

$$\tanh m_0 x_0 \approx m_0 x_0, \qquad \coth m_0 x_0 \approx \frac{1}{m_0 x_0}, \tag{2.65}$$

for $kx_0 \ll 1$. This assumption may be verified *a posteriori*, and was proved in several works including Roberts (1981*b*) and Allcock and Erdélyi (2017). The dispersion relation, Equation (2.48), may then be written as

$$\begin{aligned} m_0^2\omega^4 &+ \frac{\rho_0}{\rho_1}m_1\frac{\rho_0}{\rho_2}m_2(k^2v_A^2-\Omega^2)^2 \\ &- \frac{1}{2}m_0\omega^2(k^2v_A^2-\Omega^2)\left(\frac{\rho_0}{\rho_1}m_1+\frac{\rho_0}{\rho_2}m_2\right)\left(m_0x_0+\frac{1}{m_0x_0}\right)=0. \end{aligned} \tag{2.66}$$

In order to find approximate solutions, we also assume that the densities on either side of the slab are of the same order such that Equation (2.66) may be factorised into two equations, one for the sausage mode

$$\rho_0(k^2v_A^2-\omega^2)\left(\frac{m_1}{\rho_1}+\frac{m_2}{\rho_2}\right)+2m_0^2x_0\omega\Omega=0, \tag{2.67}$$

and one for the kink mode

$$\rho_0x_0(k^2v_A^2-\omega^2)\left(\frac{m_1}{\rho_1}+\frac{m_2}{\rho_2}\right)+2\omega\Omega=0. \tag{2.68}$$

In order to find sausage wave solutions, we rewrite Equation (2.67) as

$$(k^2c_T^2-\Omega^2)\left(\frac{m_1}{\rho_1}+\frac{m_2}{\rho_2}\right)=-2\frac{(k^2c_0^2-\Omega^2)x_0\omega\Omega}{\rho_0(c_0^2+v_A^2)}, \tag{2.69}$$

and we look for surface mode solutions to the form

$$\omega=\omega_0+kx_0\omega_1+\mathcal{O}(k^2x_0^2). \tag{2.70}$$

We find that

$$\omega_0=k(c_T+U_0), \tag{2.71}$$

for forward propagating waves, and by taking the terms of order kx_0 in Equation (2.69), we find the first order terms in the perturbation expansion, and hence obtain the approximate solution with $\Omega^2 \approx k^2c_T^2$:

$$\Omega^2 \approx k^2c_T^2\left(1-\frac{2kx_0(c_0^2-c_T^2)(c_T+U_0)^2}{(c_0^2+v_A^2)c_T^2\left[\frac{\rho_0}{\rho_1}\frac{(c_1^2-(c_T+U_0)^2)^{1/2}}{c_1}+\frac{\rho_0}{\rho_2}\frac{(c_2^2-(c_T+U_0)^2)^{1/2}}{c_2}\right]}\right). \tag{2.72}$$

Equation (2.72) reduces to Equation (31) in Allcock and Erdélyi (2017) if $U_0 = 0$. From Equation (2.68) we see that there is a solution with $\omega_0 = 0$, and so the quasi-kink mode with $\omega^2 \to 0$ as $kx_0 \to 0$ is

$$\omega^2 \approx kx_0 \frac{2\rho_0}{\rho_1 + \rho_2}(k^2 v_A^2 - k^2 U_0^2). \tag{2.73}$$

Equation (2.73) simplifies to Equation (33) in Allcock and Erdélyi (2017) if $U_0 = 0$. Roberts (1981*b*) also found a surface sausage mode solution with $\omega^2 \approx k^2 c_e^2$, however, this solution no longer exists unless a single exterior sound speed $c_1 = c_2 = c_e$ exists.

The solutions obtained above do not constitute the full set of solutions for a thin slab since we assumed that $m_0 x_0 \to 0$ as $kx_0 \to 0$. We now wish to find solutions for which $m_0 x_0$ is non-zero and finite as kx_0 tends to zero. This only occurs if $|m_0^2| \to \infty$ as $kx_0 \to 0$, and consequently, $\Omega \to k^2 c_T^2$ as $kx_0 \to 0$. We see that in this case $m_0^2 < 0$ such that all solutions are body modes, and we introduce $n_0^2 = -m_0^2$. For these solutions to exist, we require that $n_0 \tan(n_0 x_0)$ and $n_0 \cot(n_0 x_0)$ in Equations (2.55) are finite. For this to be the case, we require $n_0 x_0 \to \pi n$ for sausage modes, and $n_0 x_0 \to \pi(n - 1/2)$ for kink modes, where n is an integer.

$$\Omega^2 \approx k^2 c_T^2 \left(1 + k^2 x_0^2 \frac{(v_A^2 - (c_T - U_0)^2)(c_0^2 - (c_T - U_0)^2)}{c_0^2 v_A^2 \pi^2 n^2}\right), \tag{2.74}$$

and one describing the set of quasi-kink modes

$$\Omega^2 \approx k^2 c_T^2 \left(1 + k^2 x_0^2 \frac{(v_A^2 - (c_T - U_0)^2)(c_0^2 - (c_T - U_0)^2)}{c_0^2 v_A^2 \pi^2 (n - \frac{1}{2})^2}\right), \tag{2.75}$$

where $n = 1, 2, 3 \dots$.

2.3.3 Wide-slab Approximation

In the case of a wide slab, when the slab width is much larger than the wavelength, we demonstrate that the two interfaces that define the slab cease interacting. We begin by taking $kx_0 \gg 1$, which implies that, for surface modes, $m_0 x_0 \gg 1$ (verified by Roberts, 1981*b*). In this approximation, $\tanh m_0 x_0 \approx \coth m_0 x_0 \approx 1$, which, when applied to Equation (2.48), allows us to factorise the dispersion relation into two equations,

$$\frac{\rho_0 m_j}{\rho_j m_0}\left(k^2 v_A^2 - \Omega^2\right) - \omega^2 = 0, \tag{2.76}$$

for $j = 1, 2$. Equation (2.76) may be rearranged as

$$(R+1)c_{ph}^2 - 2U_0 c_{ph} + U_0^2 - v_A^2 = 0, \tag{2.77}$$

where $c_{ph} = \omega/k$ is the phase speed, as introduced in Chapter 1, and

$$R = \frac{\rho_1 m_0}{\rho_0 m_1}. \tag{2.78}$$

Since R depends on c_{ph} we may not immediately solve Equation (2.77). However, taking the incompressible limit, we obtain $R \to \rho_1/\rho_0$, and

$$c_{ph} = \frac{\rho_0}{\rho_0 + \rho_j} U_0 \pm \sqrt{\frac{\rho_0 + \rho_j}{\rho_0} v_A^2 - \frac{\rho_j}{\rho_0} U_0^2}. \tag{2.79}$$

Using Equation (2.79), we recover the KHI criterion, Equation (1.80), where only one side of the interface is magnetic,

$$U_0^2 > \frac{\rho_0 + \rho_j}{\rho_j} v_A^2. \tag{2.80}$$

We, therefore, see that when a surface wave propagates along a wide slab, it behaves identically to two waves propagating on two independent interfaces. As a consequence, the KHI threshold is unchanged. Equation (2.80) will be employed in Section 2.4 to compare the analytical and numerical solutions to the dispersion relation.

Body wave solutions in a wide slab also exist and are qualitatively different from surface waves. Since the velocity amplitude of the wave does not decay within the slab, but rather oscillates, the two interfaces that constitute the slab may not be independent. Allcock and Erdélyi (2017) obtained formulas for the body mode solutions in a static slab in an asymmetric environment, which would only be changed by a Doppler-shift term in a steady slab.

2.4 General Numerical Solutions

2.4.1 Method

Let us find the general solutions to the dispersion relation, Equation (2.48). Since, to the best of our knowledge, the general solutions cannot be obtained analytically, we employ a numerical scheme. We begin by nondimensionalising all quantities with respect to the Alfvén speed and, beside using the already defined Alfvén Mach number $M_A = U_0/v_A$, and normalised phase speed $\bar{c}_{ph} = c_{ph}/v_A$, we also introduce the normalised sound speeds $\bar{c}_j = \sqrt{c_j^2/v_A^2}$ (for j = 0, 1, 2), and normalised tube speed $\bar{c}_T = \sqrt{c_T^2/v_A^2}$.

In order to obtain general solutions to Equation (2.48) we write it in nondimensional form by introducing the parameters defined above. The dispersion relation may then be written as

$$
\begin{aligned}
&R_1R_2M_1M_2\bar{c}_{ph}^4 + \left[1-(\bar{c}_{ph}-M_A)^2\right]^2 \\
&-\frac{1}{2}\bar{c}_{ph}^2\left[1-(\bar{c}_{ph}-M_A)^2\right](R_1M_1+R_2M_2)\left[\tanh(M_0K)+\coth(M_0K)\right]=0
\end{aligned}
\tag{2.81}
$$

where $R_1=\rho_1/\rho_0$, $R_2=\rho_2/\rho_0$, $K=kx_0$, and

$$
\begin{aligned}
M_0^2 &= \frac{\left[1-(\bar{c}_{ph}-M_A)^2\right]\left[\bar{c}_0^2-(\bar{c}_{ph}-M_A)^2\right]}{(1+\bar{c}_0^2)\left[\bar{c}_T^2-(\bar{c}_{ph}-M_A)^2\right]} \\
M_j^2 &= \frac{m_0^2}{m_j^2} = \frac{\bar{c}_j^2\left[1-(\bar{c}_{ph}-M_A)^2\right]\left[\bar{c}_0^2-(\bar{c}_{ph}-M_A)^2\right]}{(\bar{c}_j^2-\bar{c}_{ph})(1+\bar{c}_0^2)\left[\bar{c}_T^2-(\bar{c}_{ph}-M_A)^2\right]},
\end{aligned}
\tag{2.82}
$$

for $j=1,2$.

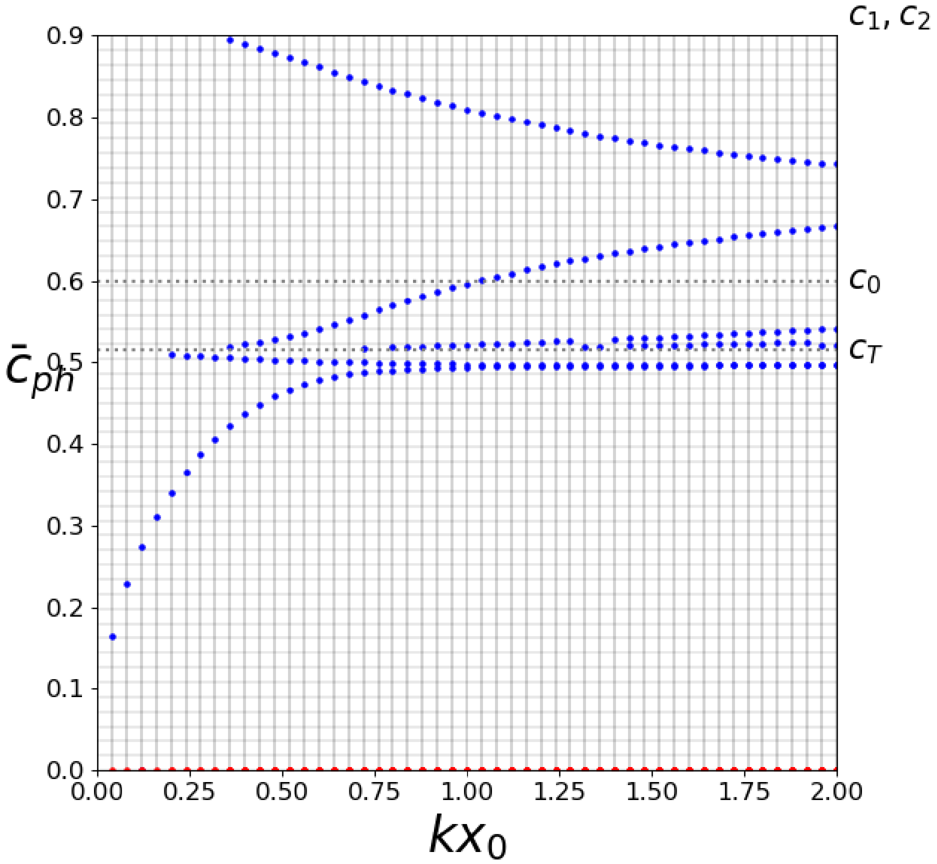

Figure 2.3: Example for finding solutions in terms of $K=kx_0$, for $M_A=0$, $R_1=R_2=1.4$, and $\bar{c}_0=0.6$.

We wish to solve Equation (2.81) for $\bar{c}_{ph}$ with respect to the parameters K, M_A, R_1, R_2, $\bar{c}_0$. Note that $\bar{c}_T$, $\bar{c}_1$ and $\bar{c}_2$ are defined in terms of the parameters R_1, R_2, and $\bar{c}_0$. For the purposes of this Thesis, we will solve Equation (2.81) for $\bar{c}_{ph}$ in terms of arbitrary K or M_A, while keeping the other variable, as well as R_1, R_2, $\bar{c}_0$, fixed.

Suppose we wish to find solutions to Equation (2.81) for arbitrary K. Our method is as follows. We begin by defining two sets,

$$\begin{aligned} X &= \left\{K^{(0)}, K^{(1)}, \ldots, K^{(\hat{x})}\right\}, \\ Y &= \left\{\bar{c}_{ph}^{(0)}, \bar{c}_{ph}^{(1)}, \ldots, \bar{c}_{ph}^{(\hat{y})}\right\}, \end{aligned} \tag{2.83}$$

such that their Cartesian product,

$$X \times Y = \left\{(K, \bar{c}_{ph}) | K \in X, \bar{c}_{ph} \in Y\right\}, \tag{2.84}$$

forms a grid in the $K\bar{c}_{ph}$-plane. We use Newton's method to solve Equation (2.81) with $\bar{c}_{ph} \in Y$ as starting points, and $K \in X$ constant. Note that this method may be used with any of the other parameters, M_A, R_1, R_2, $\bar{c}_0$, instead of K.

Figure 2.3 is a rudimentary dispersion diagram of Equation (2.81) which illustrates the method described above. We defined a 51×51 point grid, with $K^{(0)} = 0$, $K^{(50)} = 2$, $\bar{c}_{ph}^{(0)} = 0$ and $\bar{c}_{ph}^{(50)} = 0.9$, which appears in solid gray lines in the background of the figure. We define $M_A = 0$, $R_1 = R_2 = 1.4$, and $\bar{c}_0 = 0.6$ and apply our numerical scheme to find the solutions, which appear as blue dots.

In order to obtain more elegant dispersion diagrams, we also employ the technique known as *numerical continuation*. Using the method described above, we obtain a set of solutions, S, of Equation (2.81). We, then, select individual points, $(K, \bar{c}_{ph}) \in S$, and use Newton's method to find solutions for $(K + \delta K, \bar{c}_{ph} + \delta\bar{c}_{ph})$. Here, δK and $\delta\bar{c}_{ph}$ are small quantities, typically at least one order of magnitude smaller than K and $\bar{c}_{ph}$, respectively. Employing this procedure allows us to obtain a line in the $K\bar{c}_{ph}$-plane, which represents the solution to Equation (2.81) for variable K and, although discrete, may be represented as a continuous line. We use this technique to obtain Figures 2.4 to 2.12.

2.4.2 Numerical Results

Dispersion diagrams displaying general solutions to Equation (2.48) may be found in Figures 2.4 to 2.12. They illustrate the behaviour of surface and body, quasi-sausage and quasi-kink modes, under the effect of a number of different values of kx_0 and M_A. Figures 2.4 to 2.11 contain four types of equilibrium conditions. Figures 2.4 to 2.7, represent the case where $c_T < c_0 < v_A$ and the interior of the slab is denser than the exterior, while Figures 2.8 to 2.11 represent the case where $v_A < c_T < c_0$ and the exterior densities are greater than or equal to the interior. In order to better visualise the differences between the symmetric and asymmetric environments, we have included side-by-side phase diagrams that illustrate the change in behaviour due to the break in symmetry. Thus, the four types of equilibria are defined by the density of the interior of the slab as compared to the exterior regions (dense/sparse), and the symmetry of the exterior (symmetric/asymmetric).

The imaginary part of the solutions to Equation (2.48) is displayed in the dispersion diagrams where flow is present ($M_A \neq 0$) in order to make a distinction between stable and unstable modes. Stable modes correspond to purely real solutions, while unstable modes will have a non-zero imaginary component which will act as a growth factor since we assumed that all perturbations are proportional to $\mathrm{e}^{-i(\omega t - kz)}$.

In Figure 2.4a, we have recreated the dispersion diagram from Roberts (1981*b*) for the slab in a symmetric environment with $c_T < c_0 < v_A$, while in Figure 2.4b we introduced a density asymmetry. As established in Subsection 2.2.5, slow surface modes have phase speed in the range $(0, c_T)$, slow body modes have phase speed in (c_T, c_0), and fast surface modes propagate with phase speed in $(c_0, \min(c_1, c_2))$. Due to the asymmetry, the fast sausage mode is pushed into the hatched region and is not present in 2.4b.

Figures 2.5 illustrates how a background flow of $M_A = 0.4$ affects the phase diagrams for both the symmetric and asymmetric exteriors. We observe that this flow speed has broken the symmetry between forward and backward propagating solutions in both cases. Because of this, the set of forward propagating modes has been reduced to just the slow surface waves, but backward-propagating fast body modes now exist. Note that in 2.5b, the asymmetry is not large enough for the forward propagating slow surface quasi-sausage mode to not be trapped.

Figures 2.6 display the effects of a background flow of $M_A = 0.6$. This flow strength is strong enough to cause the slow body modes, which would have been backward propagating for lesser speeds, to now become forward propagating. We notice that the behaviour is identical in the two panels, meaning that the asymmetry in the equilibrium profiles does not affect the change in direction with increasing M_A.

Figures 2.7 illustrate the behaviour of the system subject to a flow of $M_A = 0.9$, which is strong enough for the KHI to occur. We see that in the case of symmetric equilibrium profiles, the instability is restricted to a short range of values of kx_0 around 0.5. However, if the exterior parameters are asymmetric, the mode which was previously unstable in only that small interval, is now unstable for any value of kx_0 greater than the instability onset value.

In Figure 2.8a, we have recreated the dispersion diagram from Roberts (1981*b*) for the slab in a symmetric environment with $v_A < c_T < c_0$, while in Figure 2.8b we introduced a density asymmetry. As established in Subsection 2.2.5, slow surface modes have phase speed in the range $(0, c_T)$, slow body modes have phase speed in (c_T, v_A), and fast body modes propagate with phase speed in $(c_0, \min(c_1, c_2))$. In order for the fast body modes to no longer be trapped in the asymmetric system, we would require $\min(c_1, c_2) < c_0$.

Figures 2.9 to 2.11 showcase the effects of a non-zero flow on the symmetric and asymmetric system for $v_A < c_T < c_0$. In order for the backward propagating slow body modes to become forward propagating, we require $M_A > 1$, as may be seen in Figure 2.10. Figure 2.11 illustrates the fact that the slow kink mode is unstable for any value of kx_0 in the case of an asymmetric density profile.

In Figures 2.12, the phase speed has been plotted with respect to M_A, for $kx_0 = 0.5$ and two different density ratios. Panel (a) represents a symmetric density profile, panel (b) an asymmetric one, and both satisfy $c_T < c_0 < v_A$. Comparing the two panels, it is immediately apparent that by increasing ρ_2, both the cut-off at $\bar{c}_2$ and the KHI threshold are lowered. Furthermore, the lowered cut-off introduces the possibility that modes are no longer trapped for some ranges of M_A. It is also worth noting that modes with $c_{ph} > \min(c_1, c_2)$ may exist as long as they are unstable since they satisfy the condition that $c_{ph}^2 > \min(c_1^2, c_2^2)$ and are thus trapped. The behaviour of the system is not qualitatively different if the characteristic speeds are ordered as $v_A < c_T < c_0$.

Figures 2.13 showcase the effect of having an asymmetric density profile on the KHI threshold value. Throughout the panels, the green and red curves (plotted for $\rho_1 = \rho_2 = \rho_0$ and $\rho_1 = \rho_2 = 2\rho_0$, respectively) represent the symmetric density profiles. In the left panel, the blue curve also represents a symmetric density profile, corresponding to a lower density ratio of $\rho_1 = \rho_2 = 0.5\rho_0$. This panel illustrates how, for symmetric density profiles, the

KHI threshold increases, both with increasing values of kx_0, but also with decreasing values of the density ratios. As suggested by Equation (2.76), the threshold value for a wide slab tends to that of a single interface. The middle and right panels illustrate the effect of increasing asymmetry in the density ratios. Due to the lack of interaction between the interface when $kx_0 \gg 1$, the greater density ratio will determine the threshold value. However, if $kx_0 \lessapprox 1$, the densities on either side will play a role.

Figure 2.14 compares the effects of increasing density ratios in the case of symmetric (left) and asymmetric slabs (centre). In both cases, three slab widths are considered: a thin slab (red), with $kx_0 = 0.1$, an "intermediate" value of $kx_0 = 1$ (green), and a wide slab (blue), with $kx_0 = 10$. In the left panel, the exterior densities are assumed to be equal ($\rho_1 = \rho_2 = \rho_e$), while in the centre, we only assumed that $\rho_2/\rho_0 = 2$. The effect of the asymmetry is most intense for small kx_0, when there is most interaction between the interfaces. The panel on the right illustrates how the wide asymmetric slab becomes unstable when the interface corresponding to the highest density ratio becomes unstable. For $\rho_1 < \rho_2$, the threshold corresponds to the interface with the constant density ratio (represented by the horizontal dotted line), while for $\rho_1 > \rho_2$, the threshold values tend to that of the interface with variable density ratio (represented by the dot-dashed curve).

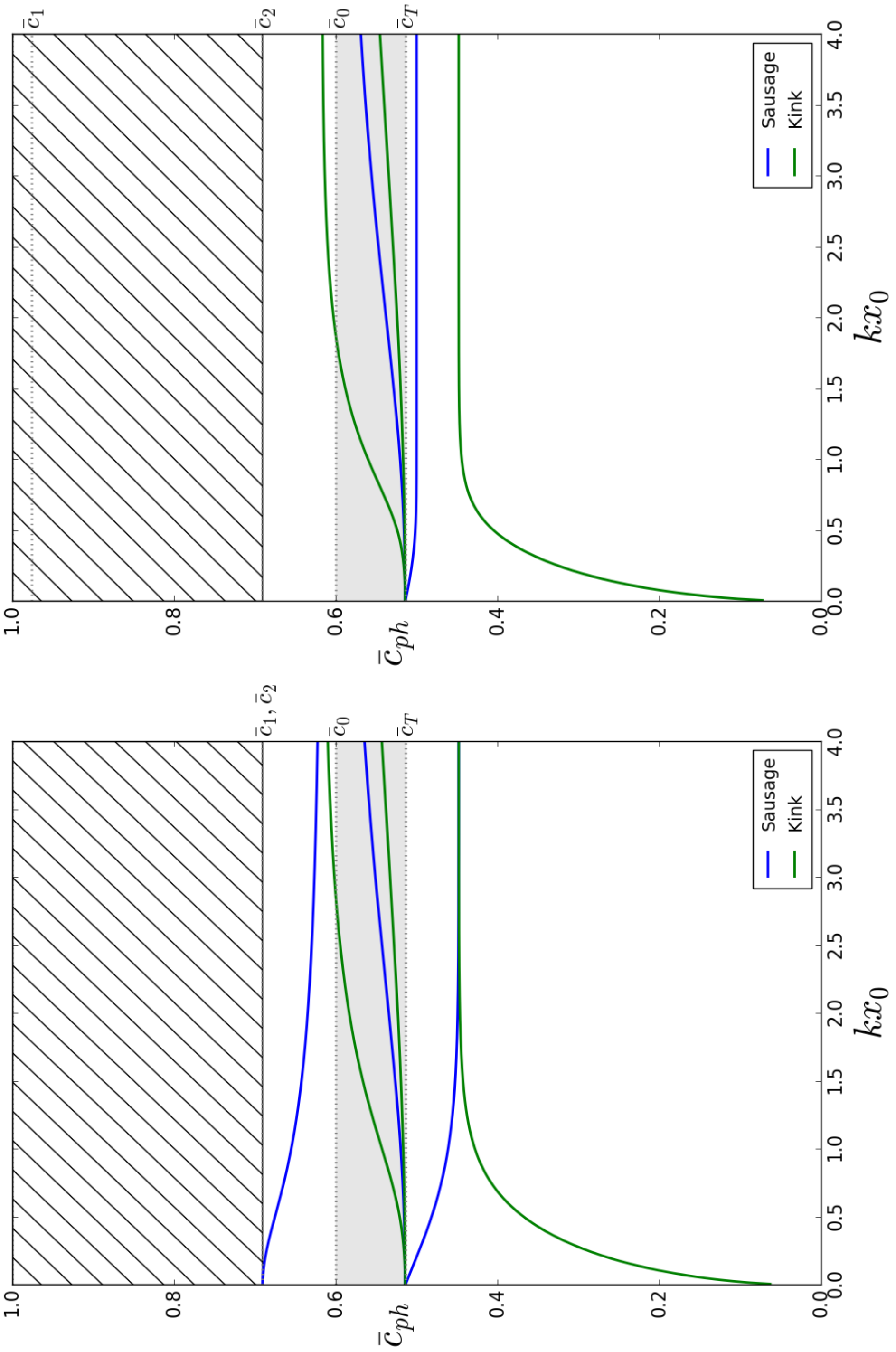

(a) $\bar{c}_0 = 0.6, \rho_1/\rho_0 = \rho_2/\rho_0 = 2.5.$

(b) $\bar{c}_0 = 0.6, \rho_1/\rho_0 = 1.25, \rho_2/\rho_0 = 2.5.$

Figure 2.4: The dispersion diagrams considering an interior that is dense, and no background flow ($M_A = 0$). Panel (a) illustrates the solutions obtained for symmetric exterior density profiles, while (b)illustrates the effects of breaking this symmetry. The shaded areas represent regions for which body modes propagate. The hatched regions contain no stable trapped solutions ($m_1^2 < 0$ or $m_2^2 < 0$).

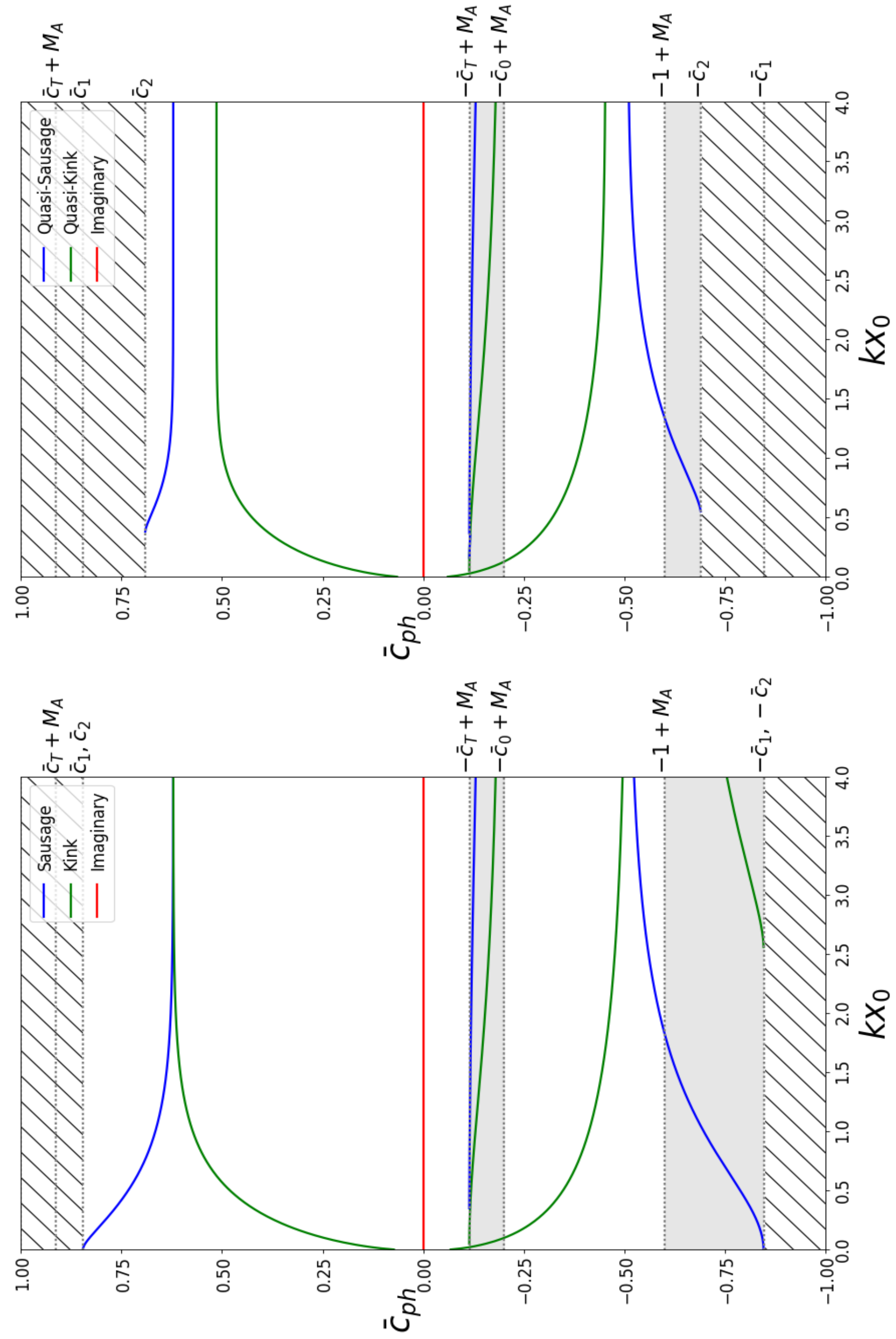

(a) $\bar{c}_0 = 0.6, \rho_1/\rho_0 = \rho_2/\rho_0 = 5/3$.

(b) $\bar{c}_0 = 0.6, \rho_1/\rho_0 = 5/3, \rho_2/\rho_0 = 5/2$.

Figure 2.5: The same as Figure 2.4, but including a background flow of Alfvén Mach number $M_A = 0.4$. The flow has removed the forward propagating fast surface modes, and slow body modes.

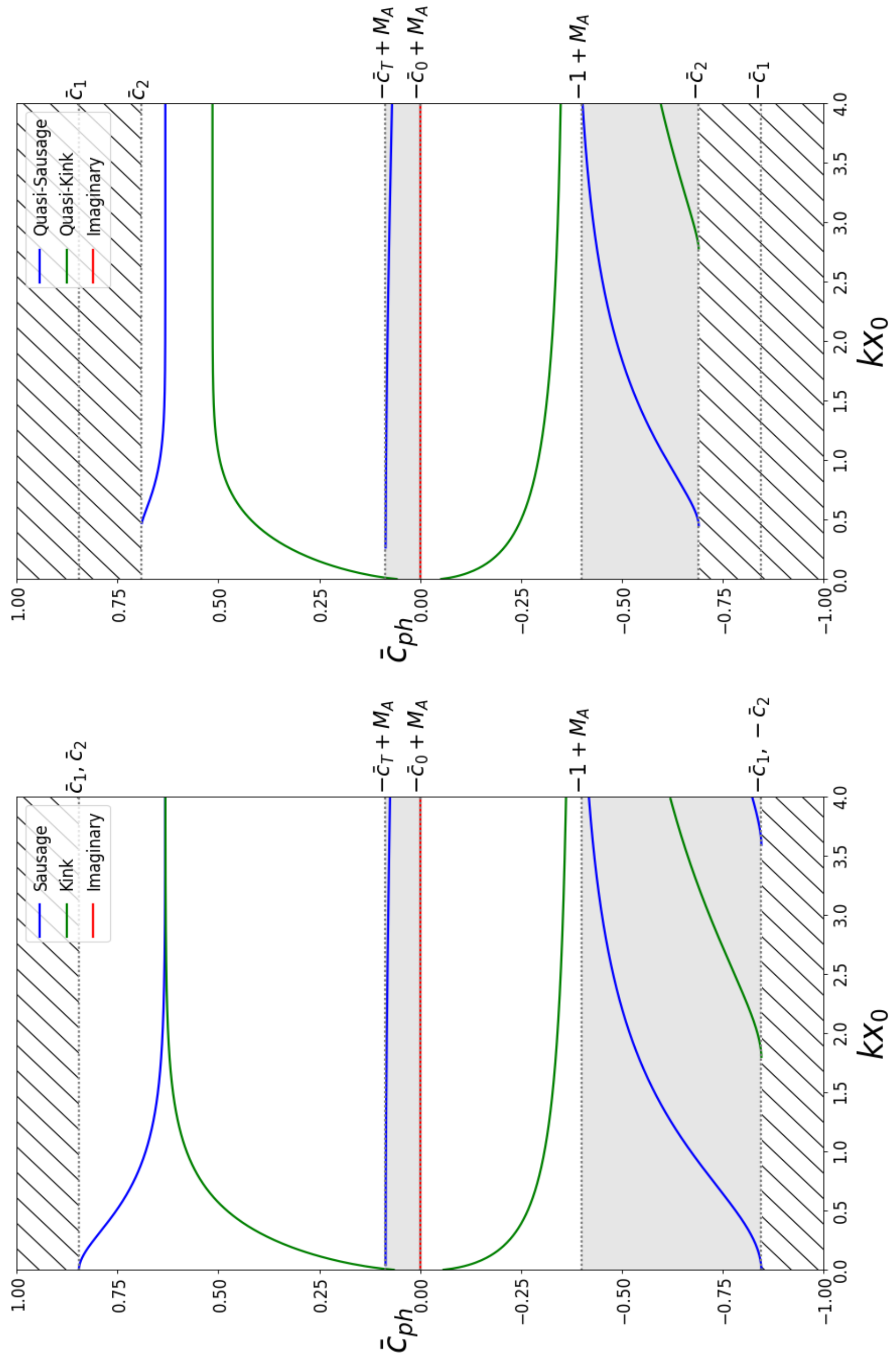

(a) $\bar{c}_0 = 0.6, \rho_1/\rho_0 = \rho_2/\rho_0 = 5/3$.

(b) $\bar{c}_0 = 0.6, \rho_1/\rho_0 = 5/3, \rho_2/\rho_0 = 5/2$.

Figure 2.6: The same as Figure 2.4, but including a background flow of Alfvén Mach number $M_A = 0.6$. The bulk flow is now strong enough to have caused the backward propagating slow body modes to become forward propagating. The asymmetric density profile does not affect the threshold value at which this happens.

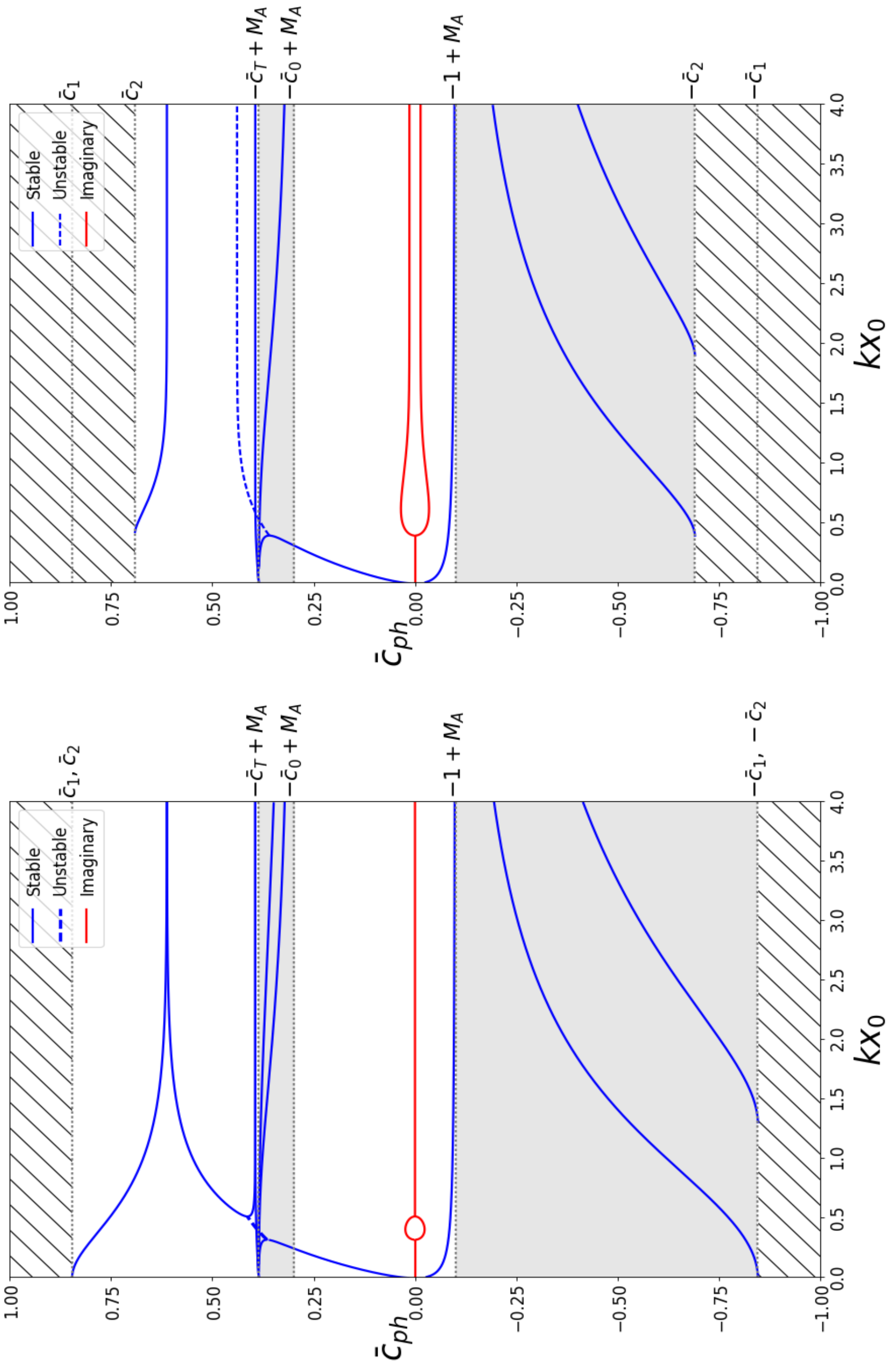

(a) $\bar{c}_0 = 0.6, \rho_1/\rho_0 = \rho_2/\rho_0 = 5/3$.

(b) $\bar{c}_0 = 0.6, \rho_1/\rho_0 = 5/3, \rho_2/\rho_0 = 5/2$.

Figure 2.7: The same as Figure 2.4, but including background flows of Alfvén Mach number $M_A = 0.9$. In the symmetric case, the KHI occurs for a small interval of kx_0. If the exterior density profile is sufficiently asymmetric, the slow kink mode becomes KH unstable for any value of kx_0 greater than some threshold value.

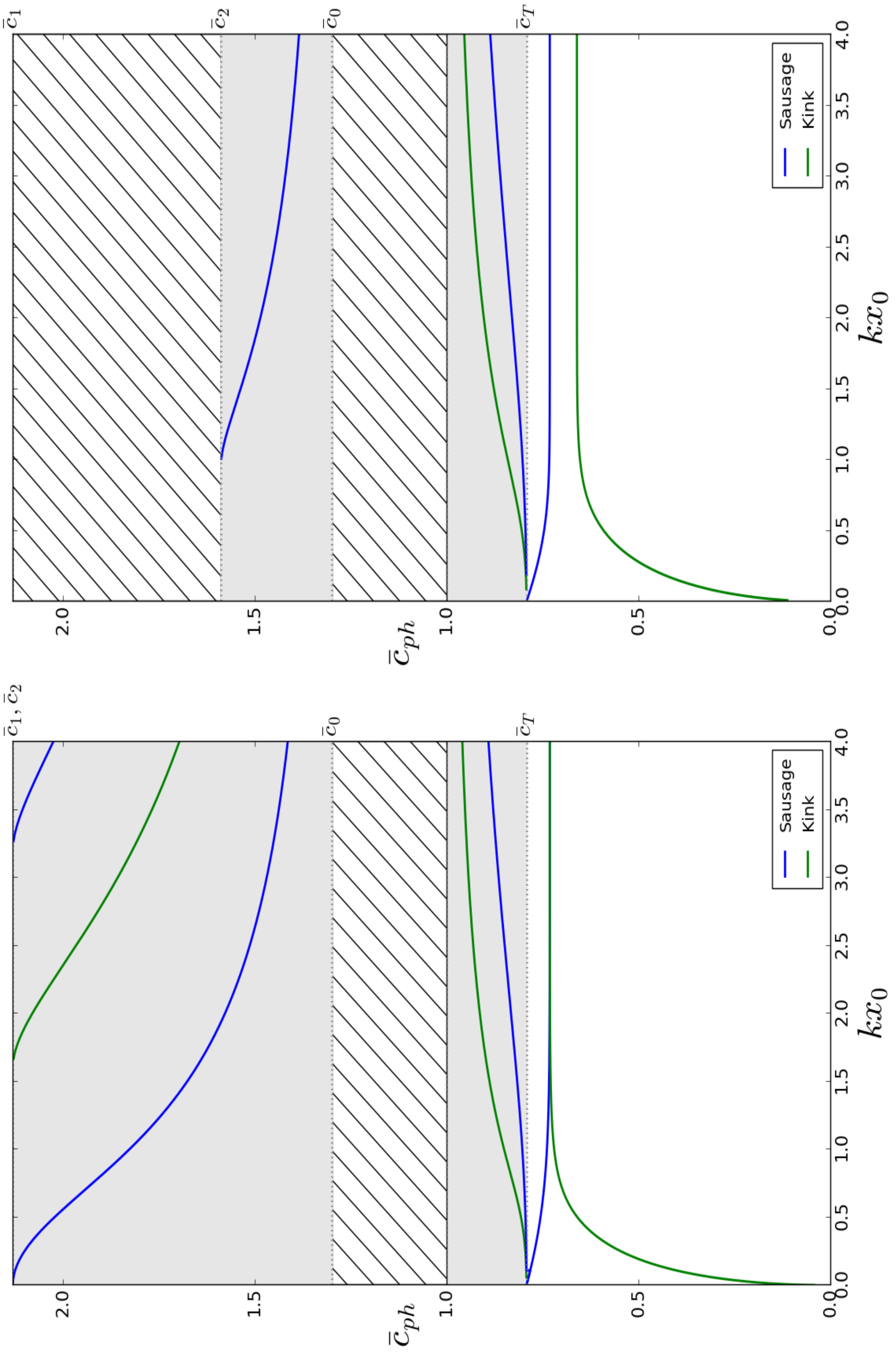

(a) $\bar{c}_0 = 1.3, \rho_1/\rho_0 = \rho_2/\rho_0 = 5/9$.

(b) $\bar{c}_0 = 1.3, \rho_1/\rho_0 = 5/9, \rho_2/\rho_0 = 1$.

Figure 2.8: The dispersion diagrams considering an interior that is sparse, and no background flow ($M_A = 0$). Panel (a) illustrates the solutions obtained for a symmetric exterior density profile, while (b) illustrates the effects of breaking this symmetry. The shaded areas represent regions for which body modes propagate. The hatched regions contain no stable trapped solutions ($m_1^2 < 0$ or $m_2^2 < 0$).

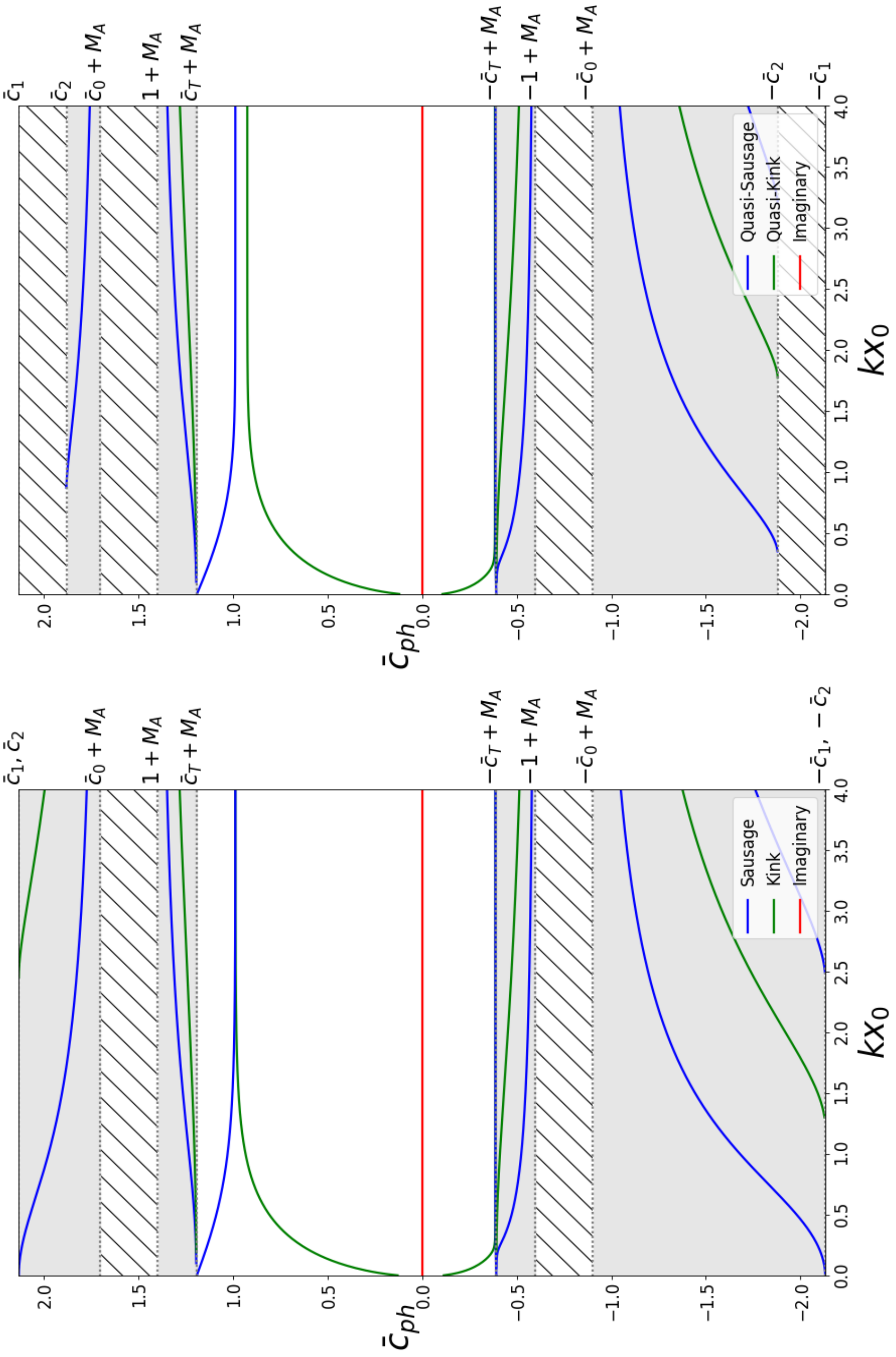

(a) $\bar{c}_0 = 1.3, \rho_1/\rho_0 = \rho_2/\rho_0 = 5/9$.

(b) $\bar{c}_0 = 1.3, \rho_1/\rho_0 = 5/9, \rho_2/\rho_0 = 5/7$.

Figure 2.9: The same as Figure 2.8, but including background flows of Alfvén Mach number $M_A = 0.4$. The flow has shifted the phase speed, but unlike in Figure 2.5 where the interior is dense, it has not removed any of the forward propagating modes.

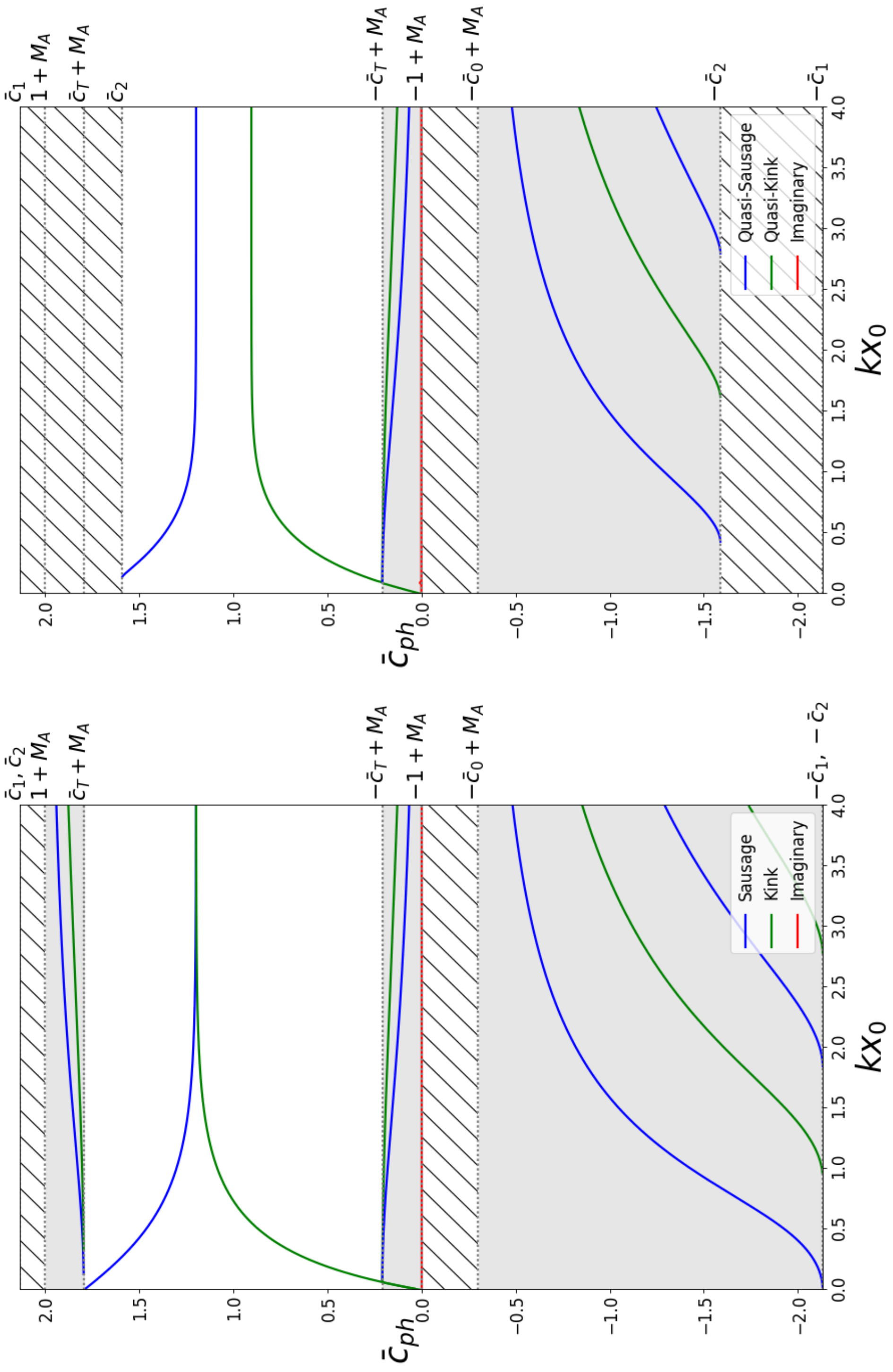

(a) $\bar{c}_0 = 1.3, \rho_1/\rho_0 = \rho_2/\rho_0 = 5/9$.

(b) $\bar{c}_0 = 1.3, \rho_1/\rho_0 = 5/9, \rho_2/\rho_0 = 1$.

Figure 2.10: The same as Figure 2.8, but including background flows of Alfvén Mach number $M_A = 1$. The bulk flow is now strong enough to have caused the backward propagating slow body modes to become forward propagating. As in the case of the dense interior, the asymmetric density profile does not affect the threshold value at which this happens.

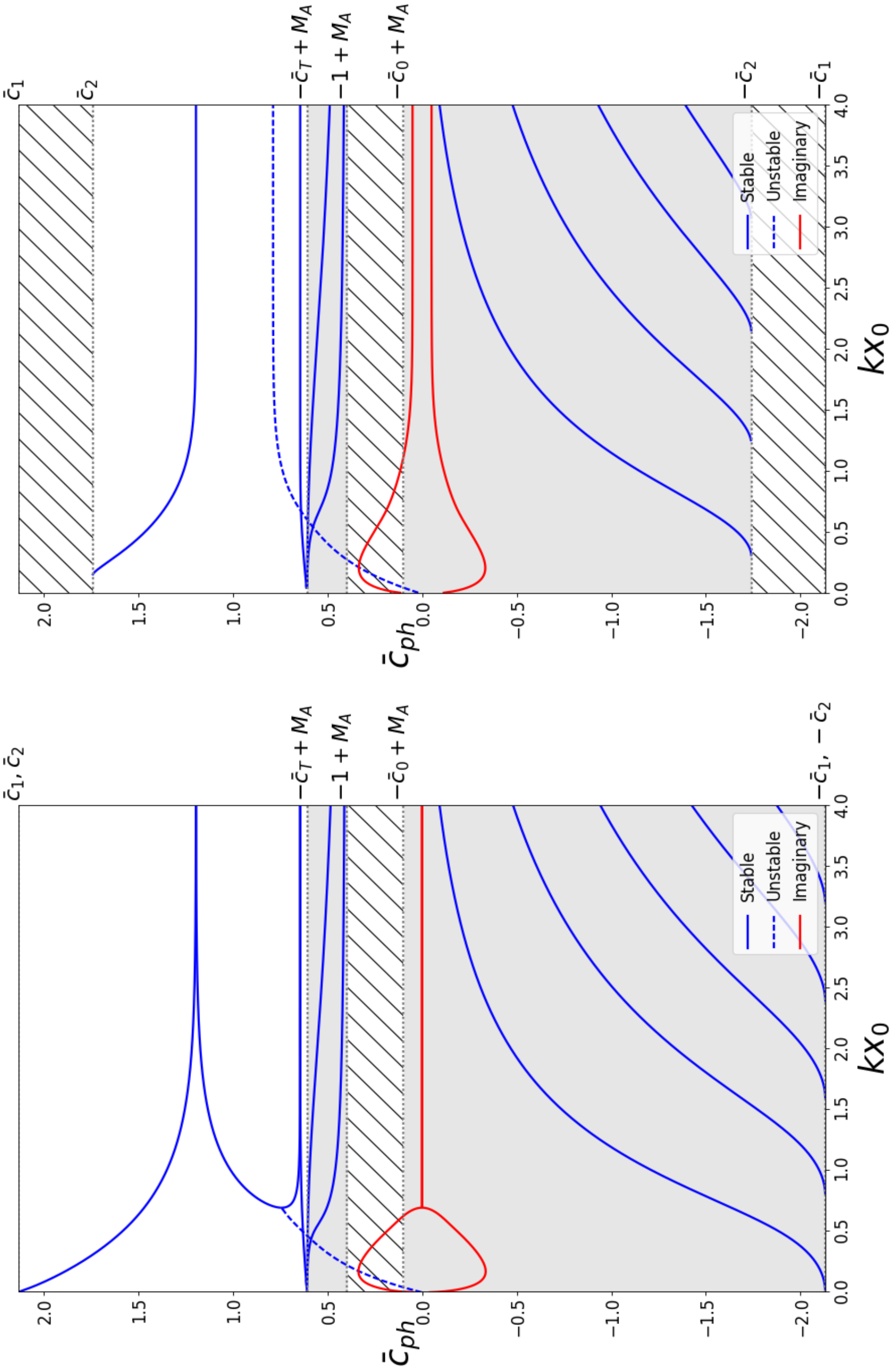

(a) $\bar{c}_0 = 1.3, \rho_1/\rho_0 = \rho_2/\rho_0 = 5/9$.

(b) $\bar{c}_0 = 1.3, \rho_1/\rho_0 = 5/9, \rho_2/\rho_0 = 5/6$.

Figure 2.11: The same as Figure 2.8, but including background flows of Alfvén Mach number $M_A = 1.4$. In the symmetric case, the KHI occurs for a small interval of kx_0. If the exterior density profile is sufficiently asymmetric, the slow kink mode becomes KH unstable for any value of kx_0.

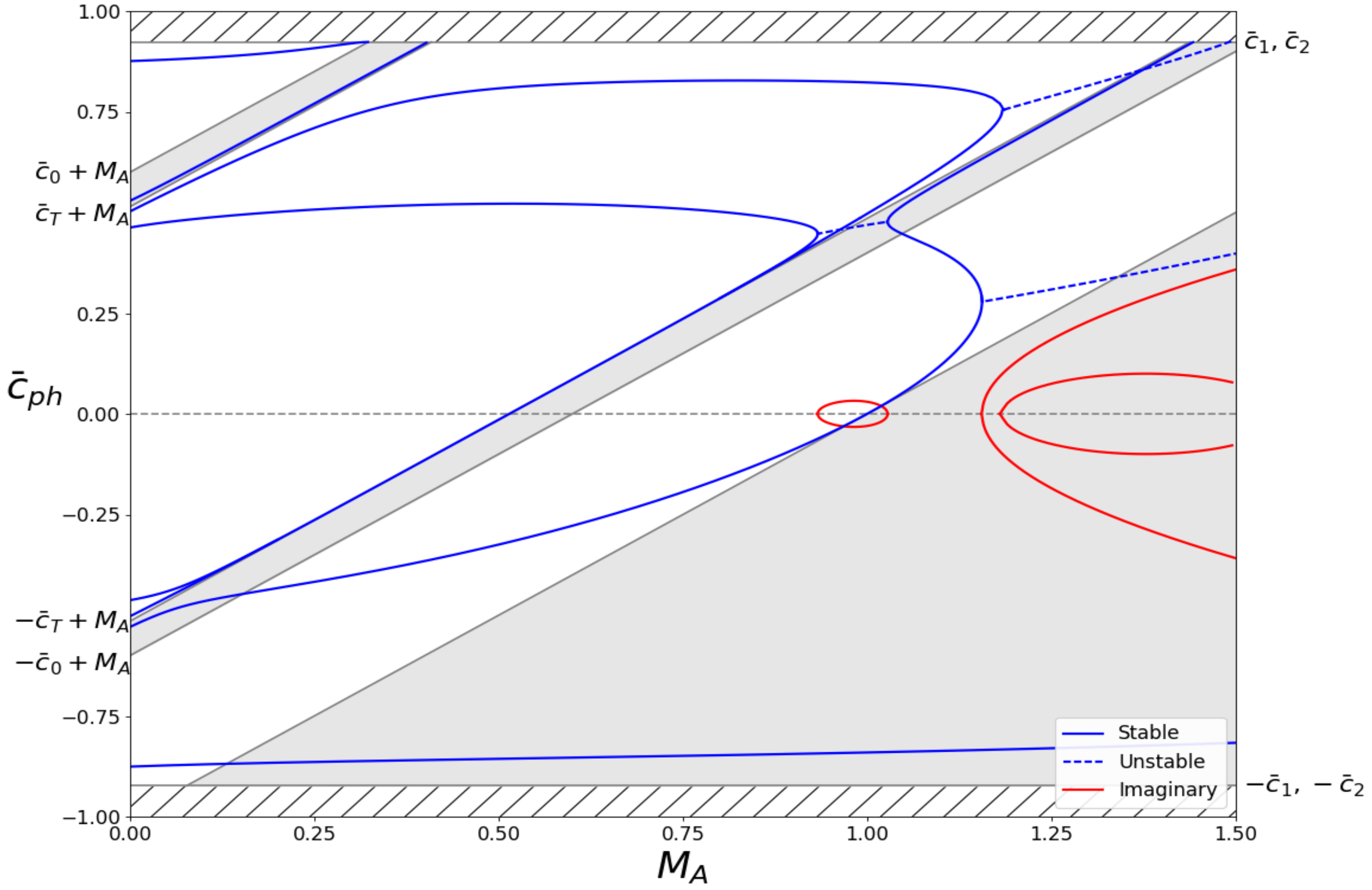

(a) $\bar{c}_0 = 0.6, \rho_1/\rho_0 = \rho_2/\rho_0 = 1.4.$

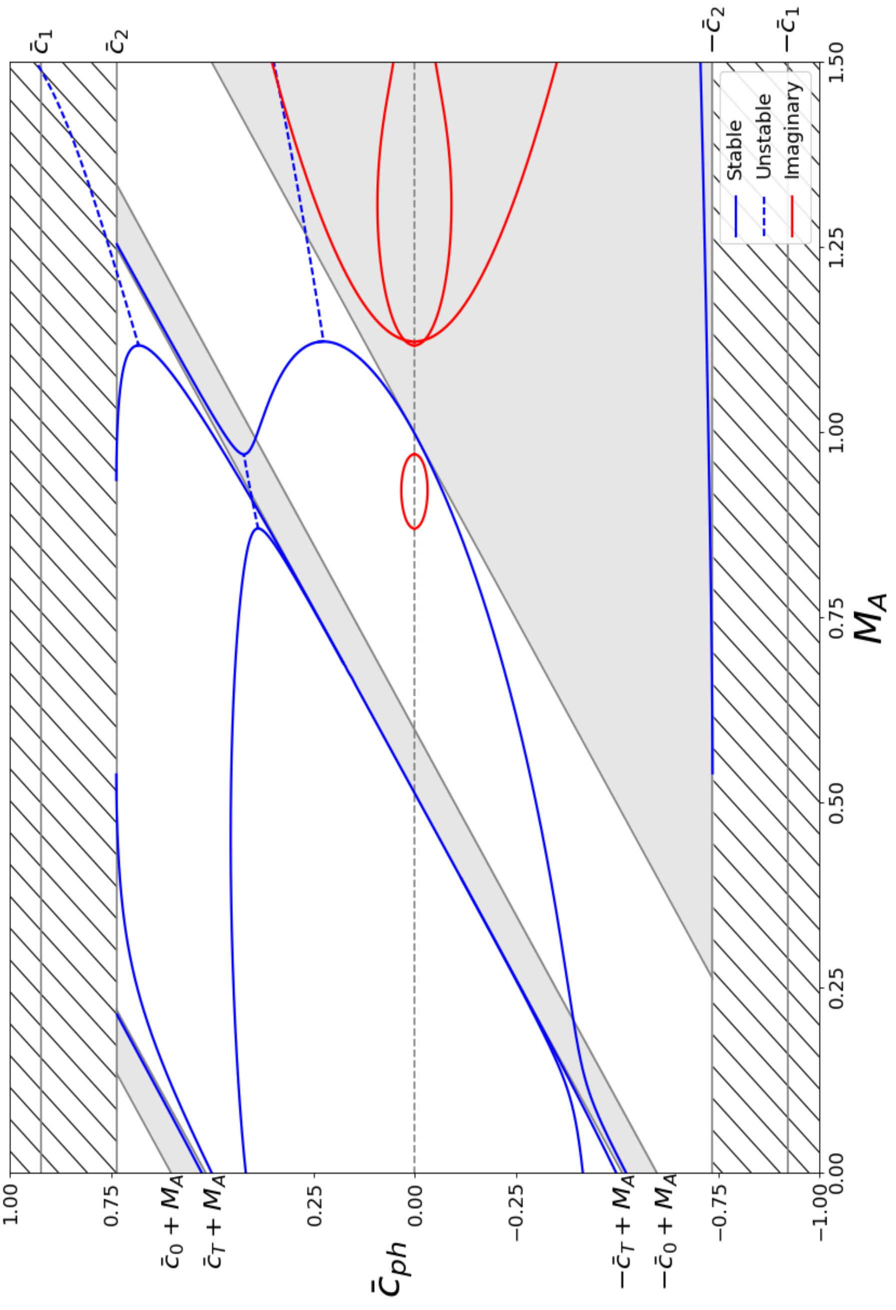

(b) $\bar{c}_0 = 0.6, \rho_1/\rho_0 = 1.4, \rho_2/\rho_0 = 3.4$.

Figure 2.12: The normalised phase speed, $\bar{c}_{ph}$, plotted with respect to the Alfvén Mach number M_A, for $kx_0 = 0.5$. The density profile is symmetric in Panel (a), and asymmetric in Panel (b). The shaded areas represent regions where body modes propagate. The hatched regions contain no stable trapped solutions ($m_1^2 < 0$ or $m_2^2 < 0$). Increasing the density on just one side of the slab decreases the KH threshold and lowers cut-off speeds.

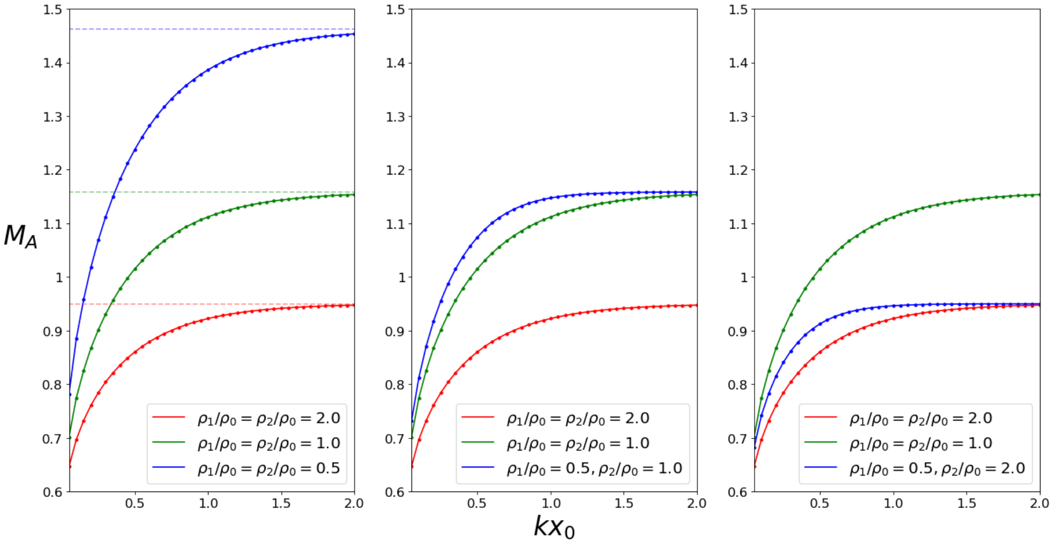

Figure 2.13: The KHI threshold values of M_A, calculated for values of kx_0 from 0.05 to 2, for symmetric and asymmetric density profiles. The dashed lines represent the threshold values of a single interface and correspond to the density ratios of their respective colour.

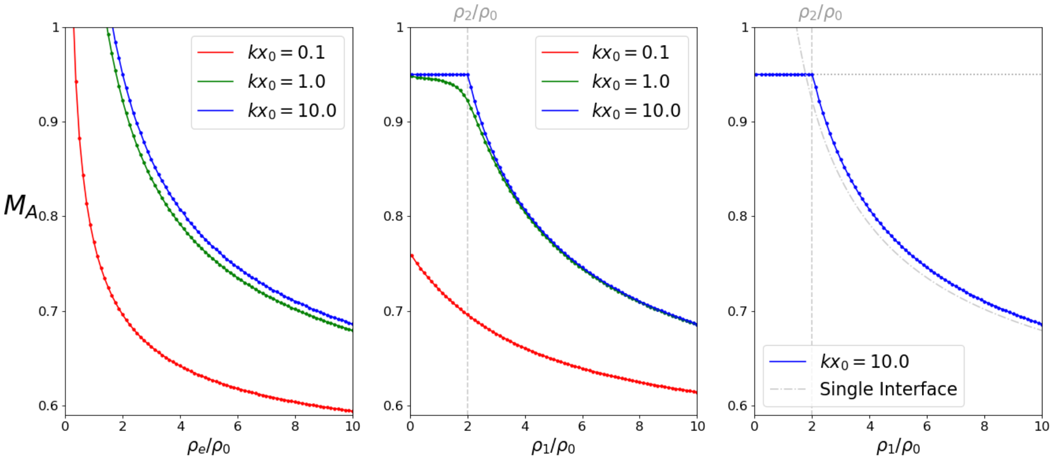

Figure 2.14: The KHI threshold values of M_A, calculated for symmetric (left) and asymmetric density profiles (center, $\rho_2/\rho_0 = 2$). The panel on the right compares the threshold values obtained for the wide asymmetric slab to that of two non-interacting interfaces. The dotted horizontal line and the dot-dashed curve represent the threshold values for the interfaces with constant and variable density ratios, respectively.

2.5 Applications

In the previous sections, we have derived the dispersion relation for a steady slab embedded in an asymmetric environment and obtained approximate and general solutions. We now wish to discuss possible applications of this model and how it compares to previous formulations.

We will primarily focus on the observations described in Foullon et al. (2011) of a KHI at a CME flank. The event observed by the Atmospheric Imaging Assembly on board the *Solar Dynamics Observatory* on November 3, 2010 was described as a series of Kelvin-Helmholtz vortices propagating at the flank of a CME. The region including the flank may be interpreted as a three-layer waveguide, with the dense CME core on one side, the CME flank in the middle, and the low density solar corona on the other side, as in Figure 2.15. Since the core ejecta is much slower than the flank on the time scale of the instability, it is reasonable to approximate it as being static.

Using the parameters measured by Foullon et al. (2011) and Equation 2.48 we wish to estimate the densities of the CME core and flank in relation to the coronal background density. We begin by assuming a background Alfvén speed $v_A = 800$ km s^{-1}, and sound speed $c_0 = 0.6 v_A$. The speeds of the ejecta flow and of the perturbations at the interface were measured to be $U_0 = 833 \pm 5\,\mathrm{km\,s^{-1}}$, and $c_{ph} = 417 \pm 7\,\mathrm{km\,s^{-1}}$, respectively. Using these values, we calculate the Alfvén Mach number of the flow, $M_A \approx 1.05$, and the non-dimensionalised phase speed, $\bar{c}_{ph} = 0.521 + \pm 0.009$. The wavenumber is measured as $k \approx 0.35$ Mm, and the width of the shear layer is estimated to be $2x_0 \approx 2.25 \pm 1.5$ Mm, making $kx_0 \approx 0.394 \pm 0.263$. Since $kx_0 < 1$, there will be interactions between the boundaries of the shear layer, meaning that the density asymmetry will play an important roll in the formation of the KHI.

Before we start our analysis, we must first note that when the density contrast between the three regions is such that $\min\{\bar{c}_1, \bar{c}_2\} < \min\{\bar{c}_0 + M_A, 1 + M_A\}$, there exist no trapped fast modes (as is the case in Figure 2.12). Since we expect this to be the case, we immediately discount the fast modes. We interpret the observation as that of a slow kink mode propagating along a highly asymmetric steady slab. It has been shown by Allcock and Erdélyi (2017) that, for both slow and fast modes, the transverse component of the displacement is highly sensitive to the density asymmetry. The slow mode interpretation is therefore reasonable despite the fact that one would expect little transverse displacement in the low-beta coronal plasma.

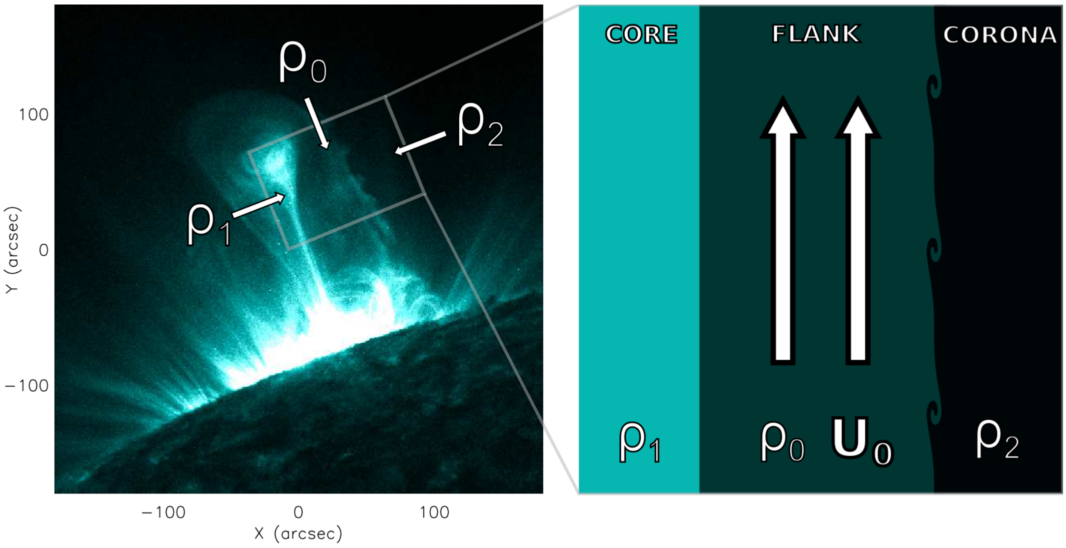

Figure 2.15: The KHI detected on the flank of the CME is displayed on the *left*. The *box on the right* is a schematic representation of the unstable region. For more details about the spatial and temporal evolution of this event, see Foullon et al. (2011).

The results of the numerical analysis are presented in Figure 2.16, where we assumed density ratios of $\rho_1/\rho_0 = 1.7$, and $\rho_2/\rho_0 = 10^{-6}$. For $M_A \approx 1.05$, we obtain $\bar{c}_{ph} = 0.526$, which matches the observed phase speed estimate of $\bar{c}_{ph} = 0.521 + \pm 0.009$. The growth rate of the instability, *i.e.* the imaginary part of ω, is calculated to be $\gamma \approx 0.023$ s^{-1}, which compares reasonably well with the observed growth rate of $\gamma = 0.05 \pm 0.03$ s^{-1}.

We note that the choice of density ratios is significantly more sensitive on the interface separating the core from the flank. We were able to obtain values of $\bar{c}_{ph}$ and γ in close agreement with the observations for values of ρ_1/ρ_0 in the range $(1.6, 1.8)$. On the other hand, ρ_2/ρ_0 may be as high 10^{-3}, with values lower than 10^{-6} having very little further effect. Our model is, therefore, in good agreement with the observations, and estimates the density of the CME ejecta to be at least 6 orders of magnitude higher than the background coronal density of $\approx 10^{-12}$ kg m^{-3}.

Our interpretation is significantly more accurate than one by means of a single interface model. In such a model, one would have to assume an unrealistically low Alfvén speed in order to match the observed phase speed with a high density contrast. Otherwise, assuming a realistic Alfvén speed $v_A = 800$ km s^{-1} would yield a density ratio of $\rho_2/\rho_0 = 1/3$ between the flank and the corona, which would significantly underestimate the density of the CME. Similarly, the high density contrast could also not be obtained from a

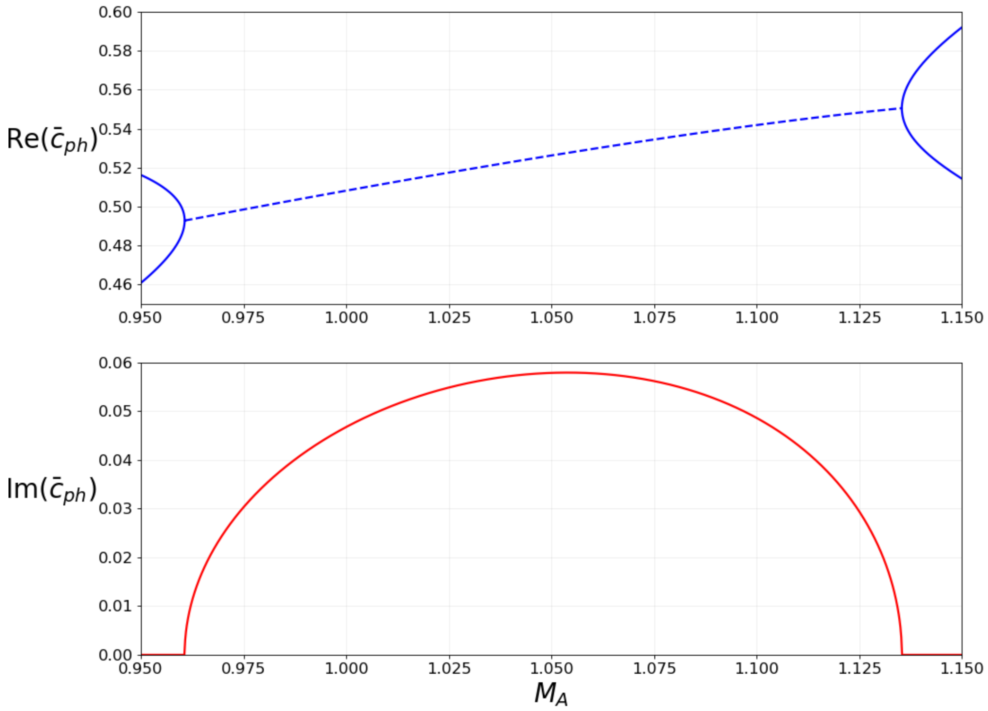

Figure 2.16: The slow kink mode plotted for $c_0 = 0.6v_A$, $\rho_1/\rho_0 = 1.7$, $\rho_2/\rho_0 = 10^{-6}$, and $kx_0 = 0.5$. The *upper* and *lower* panels contains the real and imaginary parts of the non-dimensionalised phase speed, respectively.

model of a slab in a symmetric environment.

One limitation of our model is that it does not adequately explain the absence of the KHI on the inner interface, between the core and the flank. It is likely that the core is permeated by a strong magnetic field which inhibits the formation of the instability. This effect would have to be included in a more realistic interpretation.

2.6 Summary and Discussion

In this Chapter, we studied the effects of a steady flow on the propagation of magnetoacoustic waves in a magnetic slab in an asymmetric environment, and we examined the effects of the asymmetry on the KHI threshold value. In order to accomplish this, we derived the dispersion relation, Equation (2.48), from the ideal MHD equations (Subsections 2.2.1, 2.2.2 and 2.2.3). Since our analysis is only concerned with trapped mode solutions, we first obtained necessary and sufficient conditions for their existence. We, then, classified them as surface or body, quasi-sausage or quasi-kink modes (Subsection 2.2.5), and obtained analytical solutions using the incompressible, thin slab , and wide slab approximations (Section 2.3). We also obtained general solutions to the dispersion relation and values for the KHI threshold under various parameter regimes (Section 2.4). Finally, we present an application for the model with the aim of estimating the magnetic field strength of a KH unstable CME flank in Section 2.5.

The general numerical results, including the dispersion diagrams and KHI threshold values, are presented in Figures 2.4 to 2.14. We found that the flow causes the symmetry between forward propagating ($c_{ph} > 0$) and backward propagating ($c_{ph} < 0$) modes to break, causing various modes to no longer be trapped. Furthermore, it causes backward propagating modes to become forward propagating after some threshold value particular to the mode. Finally, flow speeds past a critical value will cause the KHI to occur. In terms of the solutions to Equation (2.48), this occurs when $\omega^2 < 0$, where the imaginary part of the solution acts as the growth rate in the time evolution of the wave, causing it to steepen.

We wish to establish the qualitative effects of the asymmetry on the KHI in order to generalise the results of Allcock and Erdélyi (2017) on wave propagation. The authors found that asymmetry in the density profile asymmetrically modifies the amplitudes of the sausage and kink modes. In a symmetric slab, these modes would have anti-symmetric and symmetric amplitudes about the z-axis, respectively. However, the asymmetric density profile causes the quasi-sausage mode to increase in amplitude about the interface separating the interior from the lower density region, and decrease in amplitude about the other. The converse is true for the quasi-kink mode.

While it is clear that the slab is asymmetrically unstable for $kx_0 \gg 1$, as shown by the analysis of Subsection 2.3.3, we should consider the asymmetry for intermediate and low values of kx_0 as well. Considering the results of Allcock and Erdélyi (2017) described above, we suggest that for asymmetric density profiles and for intermediate or large values of kx_0, the slab may become asymmetrically unstable. A quasi-sausage wave would render KH unstable the boundary separating the sparser region from the interior, while the converse would be true for the quasi-kink due to the asymmetry in the wave amplitude (see also Figure 2.1). It is unlikely that this is true for thin slabs since the boundaries interact strongly for both quasi-kink and quasi-sausage modes. This hypothesis should be checked by performing a more detailed analysis of the eigenfunctions which is beyond the scope of this Thesis.

Highly asymmetric systems, such as the CME flank in Foullon et al. (2011), are likely prone to KHIs as long as the boundaries of the slab interact. In that example, the low density of the corona stabilises the CME flank, while the high density core destabilises it, and we observe the KHI. Due to this configuration of CMEs not being uncommon, we suggest that the limited number of observations are not indicative of the number of instances of the KHI in these phenomena. Further study is need in order to determine its prevalence. Applications of this model are in no way limited to CME flanks, even though they received much attention in this Chapter. Any analysis of a steady configuration, whether solar or magnetospheric, that may be modelled using the ideal MHD equations and approximated by a slab geometry, would likely benefit from the inclusion of asymmetry.

CHAPTER 3

An Analytical Model of the Kelvin-Helmholtz Instability of Transverse Coronal Loop Oscillations

Abstract

Recent numerical simulations have demonstrated that transverse coronal loop oscillations are susceptible to the Kelvin-Helmholtz (KH) instability due to the counter-streaming motions at the loop boundary. We present the first analytical model of this phenomenon. The region at the loop boundary where the shearing motions are the greatest is treated as a plane interface separating time-periodic counter-streaming flows. In order to consider a twisted tube, the magnetic field at one side of the interface is inclined. We show that the evolution of the displacement at the interface is governed by Mathieu's equation and we use this equation to study the stability of the interface. We prove that the interface is always unstable, and that, under certain conditions, the magnetic shear may reduce the instability growth rate. The result, that the magnetic shear cannot stabilise the interface, explains the numerically found fact that the magnetic twist does not prevent the onset of the KH instability at the boundary of an oscillating magnetic tube. We also make use of the notion of the loop σ-stability. We say that a transversally oscillating loop is σ-stable if the KH instability growth time is larger than the damping time of the kink oscillation. We show that even relatively weakly twisted loops are σ-stable.

This chapter is based on the following accepted manuscript:

- Barbulescu, M., Ruderman, M.S., Van Doorsselaere, T., Erdélyi, R.; An Analytical Model of the Kelvin-Helmholtz Instability of Transverse Coronal Loop Oscillations, *Astrophys. J.*, accepted.

3.1 Introduction

Transverse oscillations of coronal loops have been a subject of extensive study since their original observation on 14 July 1998 by the *Transition Region and Coronal Explorer* (TRACE) (Aschwanden et al., 1999; Nakariakov et al., 1999). For a review of the theory of these oscillations see Ruderman and Erdélyi (2009).

In particular, the damping mechanism of transverse loop oscillations has received much attention (e.g. Ruderman and Roberts, 2002; Goossens et al., 2002; Van Doorsselaere et al., 2004; Dymova and Ruderman, 2006; Williamson and Erdélyi, 2014), with the caveat that many studies have relied on the assumption that the oscillations are in the linear regime. The nonlinear damping of transverse coronal loop oscillations has also been studied, both analytically (Ruderman et al., 2010; Ruderman and Goossens, 2014; Ruderman, 2017), as well as numerically (e.g. Terradas and Ofman, 2004; Magyar and Van Doorsselaere, 2016*a*). The numerical studies revealed important effects, such as that of the ponderomotive force, and the presence of the Kelvin-Helmholtz instability (KHI) at the loop boundaries. More recently, Goddard and Nakariakov (2016) carried out a statistical study of observations of the damping of coronal loop kink oscillations.

Terradas et al. (2008) suggested that a kink oscillation may render a flux tube unstable due to the shear motions at the boundaries. The authors found that, for a smooth transition layer, the instability developed rapidly where the difference between the internal and external flow amplitudes was the greatest. However, increasing the thickness of the transitional layer significantly decreased the growth rate of the instability. It is worth noting that the KHI in smooth transition layers via other mechanisms (e.g. phase mixing, resonant absorption) had also received attention previously (see, for example, Heyvaerts and Priest, 1983; Ofman et al., 1994; Poedts et al., 1997). For a recent review on modelling the KHI see, e.g. Zhelyazkov (2015).

The topic of the transverse wave induced Kelvin-Helmholtz (TWIKH) instability was subsequently investigated by Antolin et al. (2014), who suggested that this phenomenon may be responsible for the fine strand-like structure observed in some coronal loops. The TWIKH instability has since been studied by Antolin et al. (2016); Magyar and Van Doorsselaere (2016*a*,*b*); Karampelas et al. (2017); Howson et al. (2017*b*,*a*); Karampelas and Van Doorsselaere

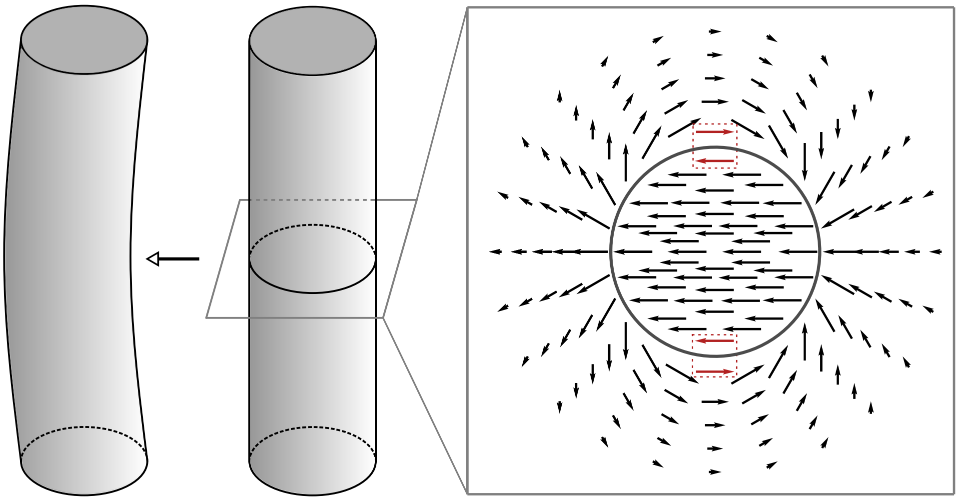

Figure 3.1: Sketch of a straight magnetic flux tube with stationary footpoints undergoing transverse (kink) motion. The panel on the right represents the velocity field in a cross section of the tube, at half the length of the tube. The greatest shearing occurs between the vectors coloured in red, highlighted by the dashed boxes.

(2018), who considered aspects of the instability onset, growth rate and observational properties.

The configuration of the equilibrium magnetic field is an important aspect of TWIKH instabilities. It was suggested by Terradas et al. (2008) that a twisted magnetic field may suppress the instability. The effect of twist on the stability of transverse loop transverse oscillations was studied numerically by Howson et al. (2017*a*) who investigated the energetics of the instability of a magnetically twisted coronal loop and found that its evolution is affected by the strength of the azimuthal component of the magnetic field. The authors also found that, when magnetic twist is present, the KHI leads to greater Ohmic dissipation as a result of the production of larger currents. Furthermore, Terradas et al. (2018) studied the evolution of the instability and found that the magnetic twist increases the instability growth time.

Numerical simulations have provided some insight into the development of the KHI, but have not thoroughly established what the conditions are needed for its onset. In this Chapter, we find these requirements analytically by modelling the boundary of the flux tube where the shearing is greatest as a single interface separating regions of different densities and magnetic fields, and performing a local stability analysis. We emulate the effect of the transverse oscillation by subjecting each region to temporally periodic counter-streaming flows.

The Chapter is organised as follows: in Section 3.2, we introduce a Cartesian model of the boundary of a twisted flux tube, and derive the governing equation for the displacement. The stability of the flow is analysed in Section 3.3, followed by applications to transverse coronal loop oscillations in Section 3.4. Section 3.5 contains the summary of the obtained results and our conclusions.

3.2 The Governing Equation

It is well established that a magnetic flux tube undergoing transverse oscillation is prone to the Kelvin-Helmholtz instability due to the shearing motions at the boundaries (Terradas et al., 2008). Considering only the fundamental mode of oscillation, we wish to obtain the TWIKH instability criterion. We start by considering a magnetically twisted flux tube of length L. The amplitude of a fundamental transverse oscillation is greatest at the half-length of the tube, $L/2$, so that is where the shearing is the greatest. We consider a plane Π orthogonal to the tube axis and crossing it at its half-length. The intersection of this plane with the tube boundary is a circle. We introduce the angle φ in the plane Π, measured from the direction of the oscillation velocity in the counter-clockwise direction. Then, the shear velocity at the tube boundary takes its maximum at $\varphi = \pi/2$ and $\varphi = 3\pi/2$, i.e. at the two points where it is parallel to the oscillation velocity (see Figure 3.1).

In order to study the effect of the shearing motions around this region, we model it as a single interface separating temporally periodic counter-streaming flows. We introduce the Cartesian coordinate system x, y, z with the x-axis parallel to the direction of the polarisation of the kink oscillation, and the z-axis parallel to the tube axis. The interior and exterior of the tube are represented by the regions $y < 0$ and $y > 0$, respectively. The equilibrium quantities in these regions are denoted by the subscripts i and e, respectively.

We assume that the equilibrium magnetic field is in the xz-plane. Since we wish to obtain the stability criteria both for straight and twisted tubes, we assume that the equilibrium magnetic field is parallel to the z-axis in the region $y > 0$, and makes an angle θ with respect to the z-axis in the region $y < 0$. Here, θ corresponds to the degree of twist (Figure 3.2a), which should be small since highly twisted magnetic flux tubes are prone to other types of instabilities, such as the kink instability, with which we are not concerned in

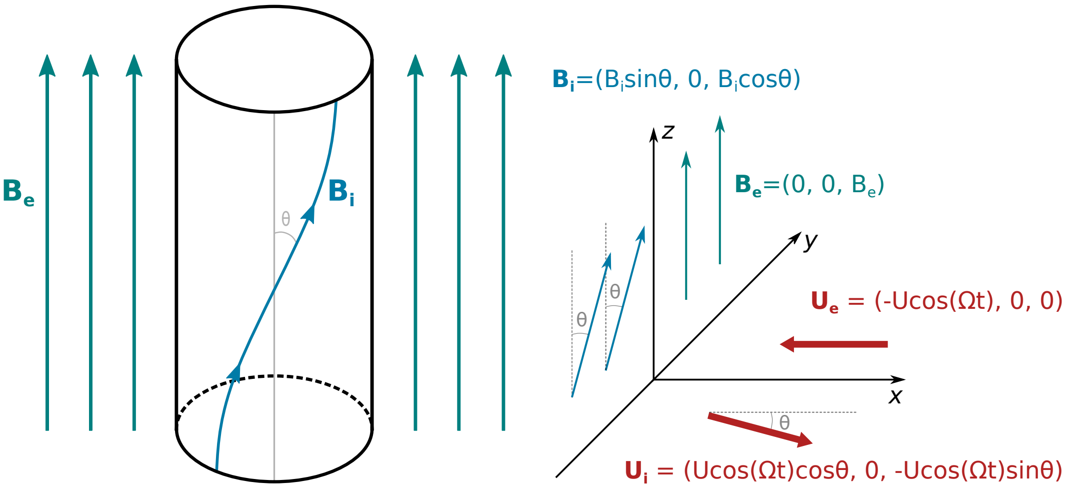

(a) A twisted magnetic flux tube embedded in a straight magnetic field.

(b) The magnetic fields and flows at the interface.

Figure 3.2: Sketch of a twisted magnetic tube, (a), and a diagram of the flows on each side of the boundary during transverse oscillation (b).

the present study (e.g. Shafranov, 1958; Kruskal et al., 1958; Hood and Priest, 1979). In the case of a non-twisted flux tube, $\theta = 0$.

In the present model, the background flows are similar to the velocity field at the boundary of a cylindrical flux tube undergoing a transverse oscillation. In transverse oscillations of coronal loops, the displacement of the flux tube's boundary is almost perpendicular to the background magnetic field in the low-beta plasma approximation (see, e.g. Ruderman, 2007), therefore, we consider unperturbed magnetic fields and flow velocities, in Cartesian coordinates, of the form

$$\begin{aligned}
\mathbf{B_i} &= (B_i \sin\theta, 0, B_i \cos\theta),\\
\mathbf{B_e} &= (0, 0, B_e),\\
\mathbf{U_i} &= (U\cos(\Omega t)\cos\theta, 0, -U\cos(\Omega t)\sin\theta),\\
\mathbf{U_e} &= (-U\cos(\Omega t), 0, 0),
\end{aligned} \tag{3.1}$$

as illustrated in Figure 3.2b. Here, the period of the oscillatory flow, $2\pi/\Omega$, corresponds to the period of oscillation of the flux tube.

It is worth noting that the problem of oscillatory counter-streaming flows has been previously studied by, e.g. Kelly (1965) and Roberts (1973). Our model is an improvement since we do not only consider parallel flows. Furthermore, our model differs from that of Roberts (1973) since we consider magnetic fields perpendicular to the flows on each side of the interface.

We study the dynamics of the outlined problem in the framework of linear ideal MHD. Since, for transverse loop oscillations, the effects of compressibility are not significant (Ruderman and Erdélyi, 2009), we may use the approximation of incompressible plasma in order to simplify the analysis. The set of governing equations is, thus, Equations (1.44) – (1.46), which we rewrite here as

$$\frac{\mathrm{D}\mathbf{v}}{\mathrm{D}t} = -\frac{1}{\rho_{i,e}}\nabla p_T + \frac{1}{\mu_0 \rho_{i,e}}(\mathbf{B_{i,e}}\cdot\nabla)\mathbf{b}, \tag{3.2}$$

$$\frac{\mathrm{D}\mathbf{b}}{\mathrm{D}t} = (\mathbf{B_{i,e}}\cdot\nabla)\mathbf{v}, \tag{3.3}$$

$$\nabla\cdot\mathbf{v} = 0, \tag{3.4}$$

$$\nabla\cdot\mathbf{b} = 0, \tag{3.5}$$

where $\mathbf{v}, \mathbf{b}$ and p_T are the perturbations of the velocity, magnetic field, and total pressure (magnetic plus plasma), $\rho_{i,e}$ are the background internal and external densities, and μ_0 is the magnetic permeability of free space. Taking into account Equation (3.1), the material derivative, $\mathrm{D}/\mathrm{D}t$, may be written as

$$\frac{\mathrm{D}}{\mathrm{D}t} = \begin{cases} \dfrac{\partial}{\partial t} + U\cos(\Omega t)\cos\theta\dfrac{\partial}{\partial x} - U\cos(\Omega t)\sin\theta\dfrac{\partial}{\partial z}, & y < 0, \\ \dfrac{\partial}{\partial t} - U\cos(\Omega t)\cos\theta\dfrac{\partial}{\partial x}, & y > 0. \end{cases} \tag{3.6}$$

Applying the material derivative to Equation (3.2) yields

$$\frac{\mathrm{D}^2\mathbf{v}}{\mathrm{D}t^2} = -\frac{1}{\rho_{i,e}}\frac{\mathrm{D}}{\mathrm{D}t}\nabla p_T + \frac{1}{\mu_0\rho_{i,e}}(\mathbf{B_{i,e}}\cdot\nabla)\frac{\mathrm{D}\mathbf{b}}{\mathrm{D}t}, \tag{3.7}$$

since the differential operators $\mathbf{B_{i,e}}\cdot\nabla$ and $\mathrm{D}/\mathrm{D}t$ are independent of $\mathbf{x}$ and, thus, commute. Introducing Equation (3.3) into (3.7), one obtains

$$\frac{\mathrm{D}^2\mathbf{v}}{\mathrm{D}t^2} - \frac{1}{\mu_0\rho_{i,e}}(\mathbf{B_{i,e}}\cdot\nabla)^2\mathbf{v} = -\frac{1}{\rho_{i,e}}\frac{\mathrm{D}}{\mathrm{D}t}\nabla p_T. \tag{3.8}$$

We now introduce the Lagrangian displacement $\boldsymbol{\xi} = \boldsymbol{\xi}(\mathbf{x}, t)$, which is related to the velocity perturbation by $\mathbf{v}(\mathbf{x}, t) = \mathrm{D}\boldsymbol{\xi}/\mathrm{D}t$, as introduced in Equation (1.47). Equation (3.8) becomes

$$\frac{\mathrm{D}^3\boldsymbol{\xi}}{\mathrm{D}t^3} - \frac{1}{\mu_0\rho_{i,e}}(\mathbf{B_{i,e}}\cdot\nabla)^2\frac{\mathrm{D}\boldsymbol{\xi}}{\mathrm{D}t} = -\frac{1}{\rho_{i,e}}\frac{\mathrm{D}}{\mathrm{D}t}\nabla p_T, \tag{3.9}$$

which may be integrated to obtain

$$\frac{\mathrm{D}^2\boldsymbol{\xi}}{\mathrm{D}t^2} - \frac{1}{\mu_0\rho_{i,e}}(\mathbf{B_{i,e}}\cdot\nabla)^2\boldsymbol{\xi} = -\frac{1}{\rho_{i,e}}\nabla p_T. \tag{3.10}$$

The arbitrary functions of integration which should have been introduced when obtaining Equation (3.10) may safely be omitted since we are only concerned with solutions at $y = 0$, and taking into account that the displacement and total pressure must be continuous at the interface.

Taking into account Equation (1.49) and the fact that the divergence operator commutes with all other differential operators in Equation, we apply $\nabla\cdot$ on Equation (3.10). The result is Laplace's equation for the total pressure

$$\nabla^2 p_T = 0. \tag{3.11}$$

We Fourier-decompose the total pressure and write it in the form $p_T = \hat{p}_T \exp[i(k_x x + k_z z)]$, such that Equation (3.11) becomes

$$\left(\frac{\mathrm{d}^2}{\mathrm{d}y^2} - k_x^2 - k_z^2\right)\hat{p}_T = 0. \tag{3.12}$$

The solution to Equation (3.12), which satisfies the condition that the total pressure is continuous at $y = 0$, is

$$\hat{p}_T(y) = p_0 \begin{cases} \mathrm{e}^{ky}, & y \leq 0, \\ \mathrm{e}^{-ky}, & y \geq 0, \end{cases} \tag{3.13}$$

where p_0 is an arbitrary constant, $\mathbf{k} = (k_x, 0, k_z)$ is the wave vector, and $k = \sqrt{k_x^2 + k_z^2}$.

Introducing $\boldsymbol{\xi} = \hat{\boldsymbol{\xi}} \exp[i(k_x x + k_z z)]$, and using Equation (3.13), the y-component of Equation (3.10) may be written as

$$\begin{aligned}\left(\frac{\partial}{\partial t} + ik_x U\cos(\Omega t)\cos\theta - ik_z U\cos(\Omega t)\sin\theta\right)^2 \hat{\xi}_y \\ + v_{Ai}^2\left(k_x\sin\theta + k_z\cos\theta\right)^2\hat{\xi}_y = -p_0\frac{k}{\rho_i}\mathrm{e}^{ky},\end{aligned} \tag{3.14}$$

for $y \leq 0$, and

$$\left(\frac{\partial}{\partial t} - ik_x U\cos(\Omega t)\right)^2 \hat{\xi}_y + v_{Ae}^2 k_z^2 \hat{\xi}_y = p_0\frac{k}{\rho_e}\mathrm{e}^{-ky}, \tag{3.15}$$

for $y \geq 0$. Here, $v_{Ai,e}^2 = B_{i,e}^2/\mu_0\rho_{i,e}$ are the Alfvén speeds on either side of the interface. Considering Equations (3.14) and (3.15) at the boundary (i.e. at $y = 0$) allows us to eliminate p_0 and obtain a single equation for $\hat{\xi}_y(t)$,

$$\begin{aligned}\rho_i\left(\frac{\mathrm{d}}{\mathrm{d}t} + ik_x U\cos(\Omega t)\cos\theta - ik_z U\cos(\Omega t)\sin\theta\right)^2\hat{\xi}_y \\ + \rho_e\left(\frac{\mathrm{d}}{\mathrm{d}t} - ik_x U\cos(\Omega t)\right)^2\hat{\xi}_y \\ + \left[\rho_i v_{Ai}^2\left(k_x\sin\theta + k_z\cos\theta\right)^2 + \rho_e v_{Ae}^2 k_z^2\right]\hat{\xi}_y = 0.\end{aligned} \tag{3.16}$$

Equation (3.16) may be rearranged such that we obtain the governing equation for the displacement at the boundary,

$$\begin{aligned}
&\left\{\frac{\mathrm{d}^2}{\mathrm{d}t^2} + 2iA\cos(\Omega t)\frac{\mathrm{d}}{\mathrm{d}t} - i\Omega A\sin(\Omega t) - B\cos^2(\Omega t) + C\right\}\hat{\xi}_y = 0,\\
&\qquad A = \frac{U\left[\rho_i(k_x\cos\theta - k_z\sin\theta) - \rho_e k_x\right]}{\rho_i + \rho_e},\\
&\qquad B = \frac{U^2\left[\rho_i\left(k_x\cos\theta - k_z\sin\theta\right)^2 + \rho_e k_x^2\right]}{\rho_i + \rho_e},\\
&\qquad C = \frac{\rho_i v_{Ai}^2\left(k_x\sin\theta + k_z\cos\theta\right)^2 + \rho_e v_{Ae}^2 k_z^2}{\rho_i + \rho_e}.
\end{aligned} \tag{3.17}$$

In order to be able to study the stability of Equation (3.17), we write $\hat{\xi}_y$ as

$$\hat{\xi}_y(t) = g(t)\eta(t), \tag{3.18}$$

which may be introduced into Equation (3.17), such that it becomes

$$\begin{aligned}
\frac{\mathrm{d}^2 g}{\mathrm{d}t^2}\eta + 2\frac{\mathrm{d}g}{\mathrm{d}t}\frac{\mathrm{d}\eta}{\mathrm{d}t} + g\frac{\mathrm{d}^2\eta}{\mathrm{d}t^2} + 2iA\cos(\Omega t)\left(\frac{\mathrm{d}g}{\mathrm{d}t}\eta + g\frac{\mathrm{d}\eta}{\mathrm{d}t}\right)\\
-i\Omega A\sin(\Omega t)g\eta - B\cos^2(\Omega t)g\eta + Cg\eta = 0.
\end{aligned} \tag{3.19}$$

In order to simplify Equation (3.19), we must find an appropriate condition for g such that the first order derivatives of η vanish. From Equation (3.19), we deduce that for there to be no first order derivatives of η in Equation (3.17), we require

$$\frac{\mathrm{d}g}{\mathrm{d}t}\frac{\mathrm{d}\eta}{\mathrm{d}t} + iA\cos(\Omega t)g\frac{\mathrm{d}\eta}{\mathrm{d}t} = 0. \tag{3.20}$$

The solution of Equation (3.19) is

$$g(t) = \exp\left\{-\frac{iA}{\Omega}\sin(\Omega t)\right\}. \tag{3.21}$$

Note that $|g(t)| = 1$, meaning that it does not affect our local stability analysis. Introducing Equation (3.21) into Equation (3.19) and simplifying the extra terms, we obtain

$$\frac{\mathrm{d}^2\eta}{\mathrm{d}t^2} + [(A^2 - B)\cos^2(\Omega t) + C]\eta = 0, \tag{3.22}$$

which may be rewritten as

$$\frac{\mathrm{d}^2\eta}{\mathrm{d}\tau^2} + [a - 2q\cos(2\tau)]\eta = 0, \tag{3.23}$$

where $\tau = \Omega t$, and

$$\begin{aligned} a &= \frac{1}{2}(A^2 - B) + C, \\ q &= \frac{1}{4}(B - A^2). \end{aligned} \tag{3.24}$$

It is now convenient to rewrite the wave vector in terms of its magnitude, k, and the angle between the wave vector and the x-axis, ϕ. Thus,

$$k_x = k \cos\phi, \quad k_z = k \sin\phi. \tag{3.25}$$

Considering Equations (3.17), (3.25) and the angle sum formulae, Equation (3.24) becomes

$$\begin{aligned} q &= \frac{r\kappa^2 M_A^2[\cos(\theta+\phi)+\cos\phi]^2}{4(1+r)^2}, \\ \alpha &= \frac{\kappa^2[\sin^2(\theta+\phi)+r\bar{v}_A^2\sin^2\phi]}{1+r}, \\ a &= \alpha - 2q, \end{aligned} \tag{3.26}$$

where $\tau = \Omega t$, $r = \rho_e/\rho_i$ is the density ratio, $M_A = U/v_{Ai}$ is the Alfvén Mach number, $\bar{v}_A = v_{Ae}/v_{Ai}$ is the ratio of Alfvén speeds, and $\kappa = kv_{Ai}/\Omega$ is the dimensionless wavenumber. From Equation (3.26), it is straightforward to see that q and a are invariant with respect to the substitution $\phi + \pi \to \phi$. This enables us to only consider values of ϕ in the interval $[-\pi/2, \pi/2]$ when studying the stability of Equation (3.23).

It is important to note that, since $|g(t)| = 1$, the variable substitution does not affect the stability analysis. Hence, unstable perturbations of the boundary correspond to unstable solutions of Equation (3.23). Equation (3.23) is known as Mathieu's equation (McLachlan, 1946). Mathieu's equation also arises in other MHD problems, namely, it describes the amplification of MHD waves by periodic external forcing (e.g. Zaqarashvili, 2000; Zaqarashvili et al., 2002, 2005), and the Rayleigh-Taylor instability of a magnetic interface in the presence of oscillating gravity (Ruderman, 2018).

3.3 Investigation of Stability

In this section, we use Equation (3.23) to study the stability of the tangential discontinuity with an oscillating shear velocity. For comparison, we first briefly outline the well-known results related to the stability of a tangential discontinuity separating steady flows. To the best of our knowledge, these results were first obtained by Syrovatskii (1957) (see also Chandrasekhar, 1961).

3.3.1 Stability of Steady Flows

Before analysing the fully time dependent governing Equation (3.23), we return to Equation (3.17) and set $\Omega = 0$, in order to perform the analysis of the configuration in the presence of steady flows. Equation (3.17) becomes

$$\left\{\frac{\mathrm{d}^2}{\mathrm{d}t^2} + 2iA\frac{\mathrm{d}}{\mathrm{d}t} - B + C\right\}\hat{\xi}_y = 0. \tag{3.27}$$

Since the coefficients in Equation (3.27) are independent of t, we can look for the solution to this equation proportional to $\mathrm{e}^{-i\omega t}$, where ω is the angular frequency of the perturbation. We obtain the dispersion relation

$$\begin{aligned}(1+r)\bar{c}_{ph}^2 - 2M_A[\cos(\theta+\phi) - r\cos\phi]\bar{c}_{ph} + M_A^2[\cos^2(\theta+\phi) + r\cos^2\phi]\\ - \sin^2(\theta+\phi) - r\bar{v}_A^2\sin^2\phi = 0,\end{aligned} \tag{3.28}$$

where $\bar{c}_{ph}^2 = \omega^2/k^2v_{Ai}^2$ is the non-dimensionalised phase speed.

We note that if the roots to Equation (3.28) are real, then $\hat{\xi}_y(t)$ is oscillatory and the system is neutrally stable. However, if complex conjugate roots exist, one of the roots has a positive imaginary part, meaning that $|\mathrm{e}^{-i\omega t}| \to \infty$ as $t \to \infty$, and the equilibrium configuration is unstable. Equation (3.28) has complex roots when its discriminant,

$$\begin{aligned}\Delta = {}& 4M_A^2\big[\cos(\theta+\phi) - r\cos\phi\big]^2\\ &- 4(1+r)\big\{M_A^2[\cos^2(\theta+\phi) + r\cos^2\phi] - \sin^2(\theta+\phi) - r\bar{v}_A^2\sin^2\phi\big\}\end{aligned} \tag{3.29}$$

is negative, which occurs when $M_A > M_{A0}$, where

$$M_{A0}^2 = \frac{(1+r)[\sin^2(\theta+\phi) + r\bar{v}_A^2\sin^2\phi]}{r[\cos(\theta+\phi) + \cos\phi]^2}. \tag{3.30}$$

Considering (3.29), the solutions of Equation (3.28) may be written as

$$\omega = \frac{kv_A}{2(1+r)}\left[2M_A\big(\cos(\theta+\phi) - r\cos\phi\big) \pm \sqrt{\Delta}\right]. \tag{3.31}$$

Equation (3.30) is singular for some specific values of ϕ and θ which are obtained by solving the equation

$$\cos\theta - \tan\phi\sin\theta + 1 = 0. \tag{3.32}$$

By inspection, we immediately find that

$$\theta = (2n+1)\pi, \tag{3.33}$$

satisfies Equation (3.32), where n is an integer, and ϕ is arbitrary. This is the case when the flows on either side of the interface are parallel and the system cannot be unstable since there is no velocity shear. Solving Equation (3.32) explicitly, we find a second solution

$$\phi = \arctan\left(\frac{1+\cos\theta}{\sin\theta}\right), \tag{3.34}$$

and by using the half angle formula, we find that

$$\frac{1+\cos\theta}{\sin\theta} = \frac{1-\cos\left((2n+1)\pi-\theta\right)}{\sin\left((2n+1)\pi-\theta\right)} = \tan\left(\frac{(2n+1)\pi-\theta}{2}\right).$$

Equation (3.34) may, thus, be written as

$$\theta = (2n+1)\pi - 2\phi. \tag{3.35}$$

Equations (3.33) and (3.35) define the lines in the $\phi\theta$-plane where solutions to Equation (3.28) are stable regardless of M_A.

The minimum value of M_{A0} in terms of θ may be obtained by differentiating Equation (3.30) with respect to ϕ and solving the resulting equation,

$$\tan\phi(\cos\theta + r\bar{v}_A^2) + \sin\theta = 0. \tag{3.36}$$

Equation (3.36) has the solution

$$\phi = \phi_0 \equiv -\arctan\left(\frac{\sin\theta}{\cos\theta + r\bar{v}_A^2}\right). \tag{3.37}$$

Substituting Equation (3.37) into Equation (3.30), yields the minimum value of M_{A0},

$$\min\{M_{A0}^2\} = \frac{\bar{v}_A^2(1+r)\tan^2(\theta/2)}{1+r\bar{v}_A^2}. \tag{3.38}$$

It follows that the system is stable for any value of M_A below $\min\{M_{A0}\}$, while there are always unstable perturbations when $M_A > \min\{M_{A0}\}$. The value of $\min\{M_{A0}^2\}$ is plotted with respect to θ in Figure 3.3. Although for applications to transverse loop oscillations we only consider $\theta \ll 1$, here we included a wider range of values for completeness.

The value of M_{A0} is illustrated as a contour plot with respect to ϕ and θ in Figure 3.4. Both the singular values obtained in Equations (3.33) and (3.35) are found in this figure. Furthermore, for the values of $\bar{v}_A = \sqrt{3}$ and $r = 1/3$, which were considered here, Equation (3.37) reduces to $\phi_0 = (2n+1)\pi - \theta/2$.

One final remark must be made regarding the stability of solutions of Equation (3.28). Since ω is proportional to k, as shown in Equation (3.31), it follows

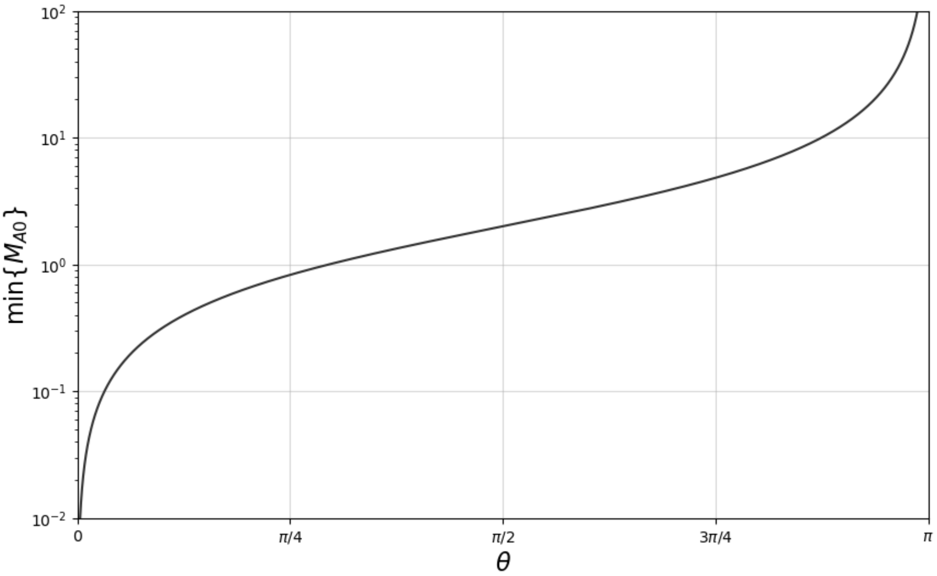

Figure 3.3: The minimum value of M_{A0} with respect to θ, for $\bar{v}_A^2 = r^{-1} = 3$.

that the instability growth rate is also proportional to k. This implies that the growth rate tends to infinity as $k \to \infty$. Since the growth rate of the instability is unbounded, we say that the initial value problem describing the evolution of the boundary is *ill-posed*. If the growth rate were bounded as $k \to \infty$, we would have said that the initial value problem were *well-posed*. In the case of the stability of Equation (3.23) for the oscillatory flows defined in Equation (3.1), the question of whether the initial value problem is well- or ill-posed is discussed in Subsection 3.3.3.

3.3.2 Stability of Oscillating Flows

We now use Equation (3.23) to study the stability for arbitrary values of the equilibrium quantities. Floquet's theorem states that Equation (3.23) has a solution of the form

$$\eta_+(\tau) = \mathrm{e}^{\mu\tau} P(a, q, \tau),$$

where $\mu = \mu(a, q)$ is the characteristic exponent, and $P(a, q, \tau)$ is a periodic function in τ, with period π (see, e.g., McLachlan, 1946; Abramowitz and Stegun, 1965). Since Equation (3.23) is invariant with respect to the substitution $-\tau \to \tau$ it follows that $\eta_-(\tau) = \mathrm{e}^{-\mu\tau} P(a, q, -\tau)$ is also a solution to this equation. Then, the general solution to Equation (3.23) is the linear combination of $\eta_+(\tau)$ and $\eta_-(\tau)$ unless $i\mu$ is an integer number.

The parameter μ determines the nature of solutions to Mathieu's equation. We may always assume that $\Re(\mu) > 0$, unless μ is purely imaginary, where $\Re$

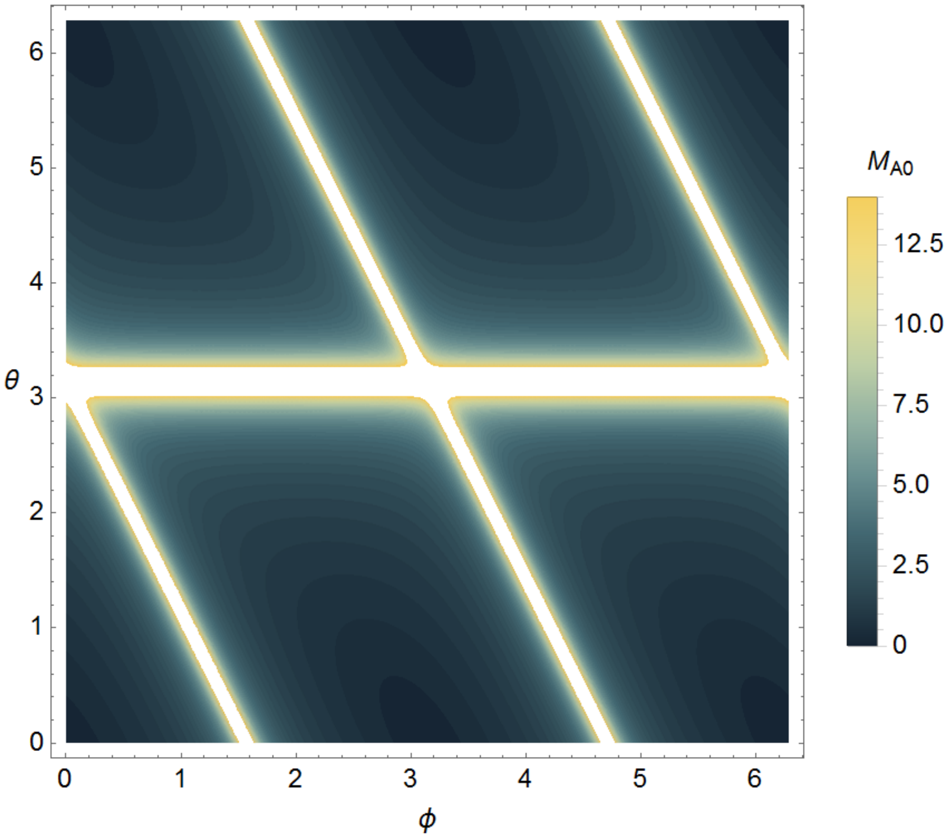

Figure 3.4: Contour plot of M_{A0} with respect to ϕ and θ, for $\bar{v}_A^2 = r^{-1} = 3$.

indicates the real part of a quantity. Since we may write

$$\mathrm{e}^{\mu\tau} = \exp(\Re(\mu)\Omega t)\exp(i\Im(\mu)\Omega t),$$

where $\Im$ indicates the imaginary part of a quantity, it follows that purely imaginary values of μ correspond to neutrally stable solutions, while real and complex values correspond to unstable solutions. Hence, $\Re(\mu) > 0$ corresponds to an unstable perturbation. Unfortunately, μ cannot be easily computed analytically, and, for this reason, we perform a numerical analysis to gain further insight.

Following McLachlan (1946), we plot the stability diagram of Equation (3.23) in the qa-plane (Figure 3.5a). In accordance with the definition of q in Equation (3.26), we only consider $q > 0$. The white and hatched regions correspond to purely imaginary and real/complex values of μ, respectively, and thus, to stable and unstable solutions to Equation (3.23). The contours bounding the regions are defined by the condition that $i\mu$ is an integer number, so that Equation (3.23) has either π or 2π-periodic solutions when the point (q, a) is on one of these contours. These contours are called the characteristic curves,

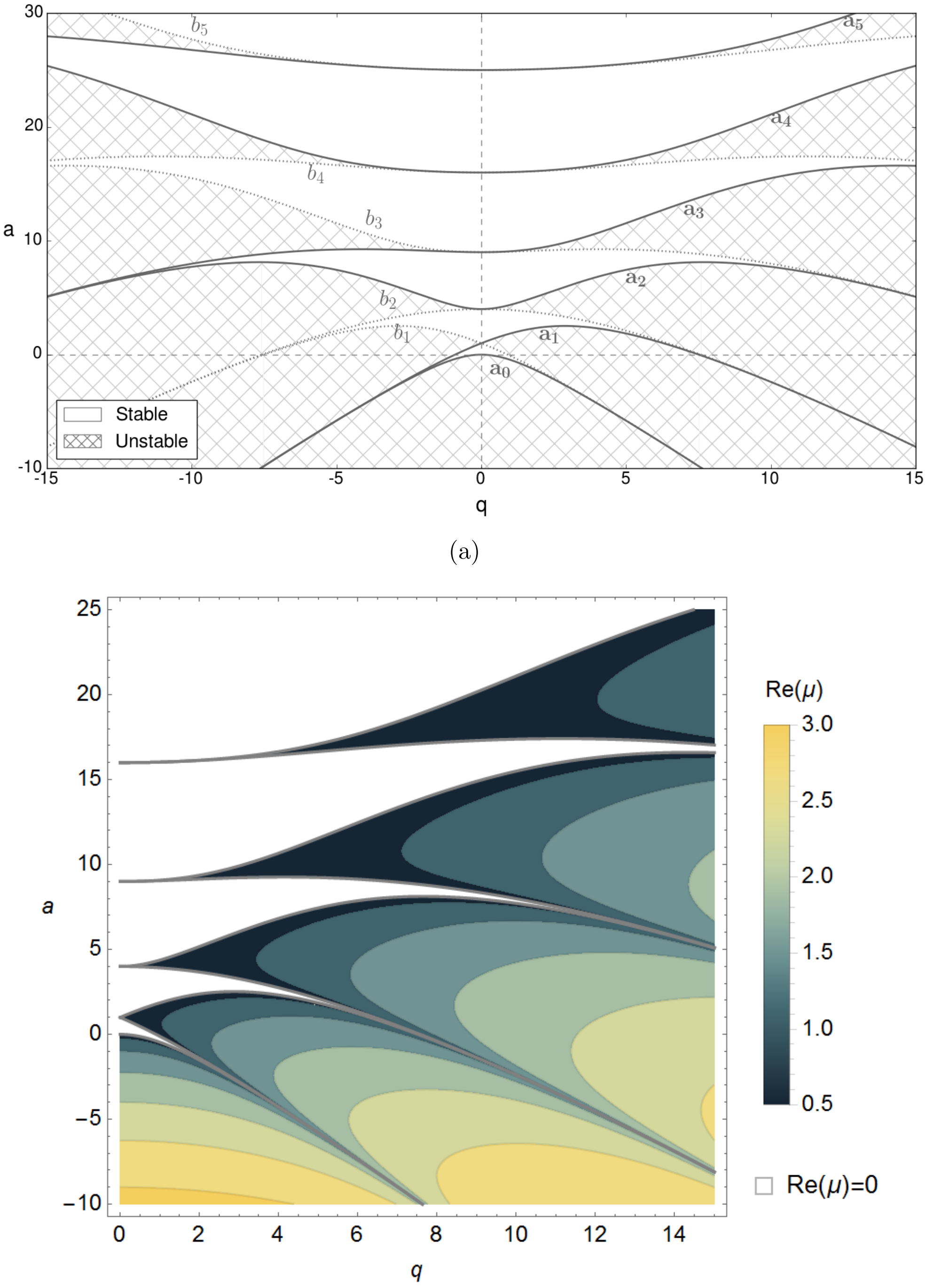

(a)

(b)

Figure 3.5: The stability diagram for solutions to Mathieu's equation (a). Solutions are stable/unstable for (q, a) in the white/hatched region. In (b), the real part of μ is plotted for $q > 0$.

and are defined by the equations $a = a_j(q)$ and $a = b_j(q)$. These functions satisfy the inequalities $a_j < b_{j+1} < a_{j+1}$, where $j = 0, 1, 2, \ldots$. The curves $a_j(q)$ and $b_j(q)$ are shown by solid and dotted lines, respectively, in Figure 3.5a. The asymptotic behaviour of $a_j(q)$ and $b_{j+1}(q)$ for large q is given

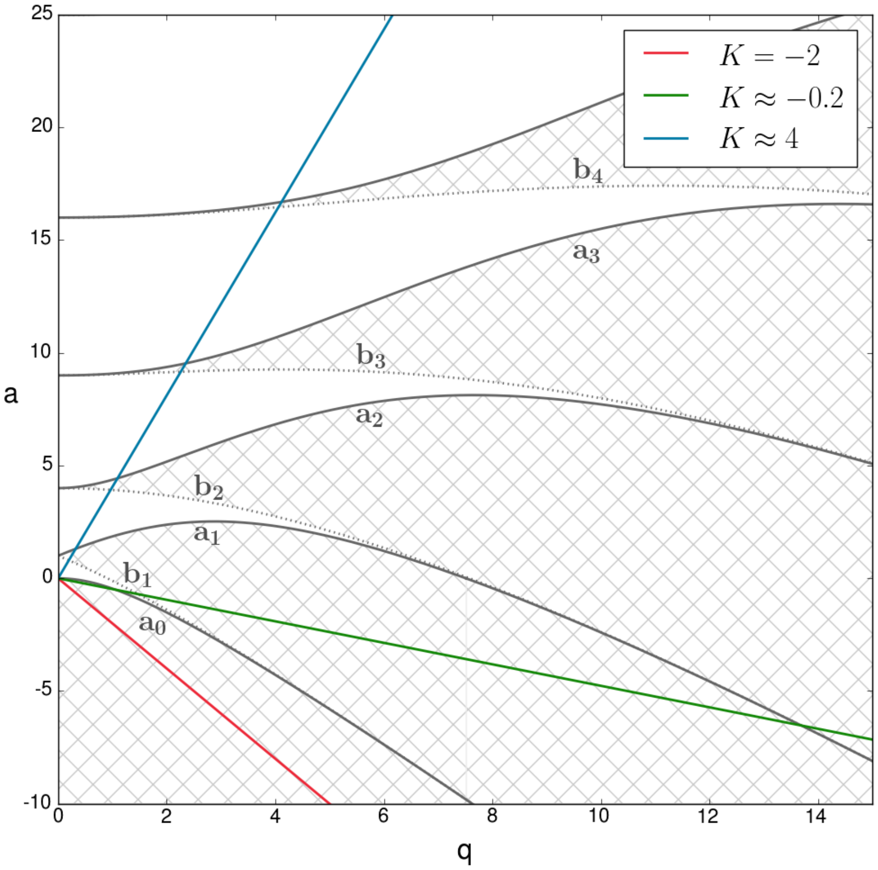

Figure 3.6: The stability diagram for solutions to Mathieu's equation, for three possible values of K. The curves $a = a_j(q)$ and $a = b_j(q)$ are shown by solid and dotted lines, respectively, as in Figure 3.5a. The blue, green, and red straight lines correspond to $K \approx 4$, $K \approx -0.2$, and $K = -2$, respectively.

by $a_j(q) \sim b_{j+1}(q) \sim -2q$ (Abramowitz and Stegun, 1965).

Complementary to the above, Figure 3.5b shows the values of the characteristic exponent μ. Purely imaginary solutions are plotted in white, and are separated from real/complex solutions by the characteristic curves, while the real part of μ is plotted in contours in the unstable regions.

The coefficients in Equation (3.23) depend on six dimensionless parameters. Four of these parameters, r, θ, M_A, and $\bar{v}_A$, are only dependent on the equilibrium quantities, while the other two, κ, and ϕ, are related to particular perturbations, and are thus arbitrary. Hence, we must study the behaviour of solutions to Equation (3.23) for all possible values of these two parameters. When ϕ is fixed and κ varies from 0 to ∞, Equations (3.26) describe a straight line in the qa-plane. The equation of this line may be written as

$$a = Kq, \quad K = \frac{4M_{A0}^2}{M_A^2} - 2. \tag{3.39}$$

From Equations (3.30) and (3.39), we note that $K > -2$ for any $\theta \neq 0$ and any values of the other parameters. Considering the asymptotic behaviours of the characteristic curves, it follows that the line $a = Kq$ always intersects all curves $a = a_j(q)$ and $a = b_{j+1}(q)$, for $j = 0, 1, \dots$. Hence, there always exist some values of κ and ϕ for which perturbations are unstable, regardless of the values of the other parameters. This implies that the tangential discontinuity separating oscillating flows is unstable for any value of M_A, which is qualitatively different from the discontinuity separating steady flows considered in Subsection 3.3.1. In the case of no magnetic shearing, i.e. when $\theta = 0$, perturbations with $\phi = \phi_0 = 0$ and any κ are unstable since the line $a = Kq$ will always be under the curve $a_0(q)$. This is illustrated by the red line in Figure 3.6. The green and blue lines in Figure 3.6 correspond to $\theta = 0.5°$ and $\theta = 1°$, respectively, and $\phi = \phi_0$. The straight lines in Figure 3.6 are further discussed in Subsection 3.4.1.

3.3.3 The Initial Value Problem

In Subsection 3.3.2, it was demonstrated that all solutions of Equation (3.23), with q and a satisfying Equation (3.26), are unstable for arbitrary k. Recall from the definition in Subsection 3.3.1 that the *initial value problem* for Equation (3.23) is said to be *well-posed* if the growth rate of the instability is bounded as $k \to \infty$, and *ill-posed* if the growth rate is unbounded as $k \to \infty$. The unbounded growth problem as $k \to \infty$ consequence of neglected dissipation, which scales like k^2.

In Subsection 3.3.1 it was shown that, if the flows on each side of the boundary are steady, the configuration is unstable for $M_A > \min\{M_{A0}\}$ and stable for $M_A < \min\{M_{A0}\}$. Furthermore, the initial value problem for $M_A > \min\{M_{A0}\}$ was shown to be ill-posed. In the current Subsection, we prove that the initial value problem for Equation (3.23), with q and a satisfying Equation (3.26), is ill-posed for $M_A > \min\{M_{A0}\}$, and well-posed for $M_A < \min\{M_{A0}\}$.

In order to prove that the initial value problem is ill-posed for $M_A > \min\{M_{A0}\}$, we use the comparison theorem for second order linear ordinary differential equations, also called the Sturm-Picone comparison theorem (e.g. Coddington and Levinson, 1955). This theorem states that, given two equations of the form

$$\frac{\mathrm{d}^2 f}{\mathrm{d}t^2} + g_{1,2}(t) f = 0, \tag{3.40}$$

where $g_{1,2}(t)$ are piecewise continuous functions on an interval $[t_0, t_1]$, with $g_1 \geq g_2$, it may be shown that $f_1 \geq f_2$, where $f_{1,2}(t)$ are the solutions of the two Equations (3.40). This theorem is only valid if the two Equations (3.40) have identical initial conditions.

Consider $M_A > M_{A0}$, such that $K < 2$, as may be seen from Equation (3.39). The scaled variables $\tilde{a} = \kappa^{-2}a$, $\tilde{q} = \kappa^{-2}q$, and $\tilde{\tau} = \kappa\tau$ are introduced, and Equation (3.23) is rewritten as

$$\frac{\mathrm{d}^2\eta}{\mathrm{d}\tilde{\tau}^2} + [\tilde{a} - 2\tilde{q}\cos(2\tilde{\tau}/\kappa)]\eta = 0. \tag{3.41}$$

It is important to note that $\tilde{a}$ and $\tilde{q}$ are independent of κ, and also that $\tilde{a} = K\tilde{q}$. The aim, now, is to find some Equation of the form

$$\frac{\mathrm{d}^2\eta}{\mathrm{d}\tilde{\tau}^2} + g\eta = 0. \tag{3.42}$$

such that

$$\tilde{a} - 2\tilde{q}\cos(2\tilde{\tau}/\kappa) \geq g, \tag{3.43}$$

on the interval $\tilde{\tau} \in [0, \tilde{\tau}_0]$, where $\tilde{\tau}_0$ is to be determined.

Let $g = -4h^2\tilde{q}$. For $\tilde{\tau} = 0$, the inequality

$$2 - K > 4h^2, \tag{3.44}$$

should be satisfied, which means that we may write

$$h = \frac{1}{2}\sqrt{1 - K/2}. \tag{3.45}$$

For $\tilde{\tau} = \tilde{\tau}_0$, the equality

$$\tilde{a} - 2\tilde{q}\cos(2\tilde{\tau}/\kappa) = -4h^2\tilde{q}, \tag{3.46}$$

should be satisfied. Equation (3.46) may be rearranged as

$$\tilde{\tau}_0 = \frac{1}{2}\kappa \arccos(1/2 + K/4) = \kappa \arcsin h \tag{3.47}$$

From Equations (3.44), (3.45), (3.46), and (3.47) it follows that

$$\tilde{a} - 2\tilde{q}\cos(2\tilde{\tau}/\kappa) \geq -4h^2\tilde{q}, \tag{3.48}$$

for $\tilde{\tau} \in [0, \tilde{\tau}_0]$, where $\tilde{\tau}_0 = \kappa \arcsin h$. Both the left-hand and right-hand sides of Equation (3.48) are continuous on the interval $[0, \tilde{\tau}_0]$.

In order to be able to use the comparison theorem, the equation

$$\frac{\mathrm{d}^2\eta}{\mathrm{d}\tilde{\tau}^2} - 4h^2\tilde{q}\eta = 0, \tag{3.49}$$

is considered. A solution to Equation (3.49) is

$$\eta_1 = \eta_0 \exp(2h\tilde{q}^{1/2}\tilde{\tau}) = \eta_0 \exp\left(\tau\sqrt{q(1-K/2)}\right), \tag{3.50}$$

where η_0 is an arbitrary constant. From Equation (3.50) and the definition of q in Equation (3.26), it follows that η_1 is unbounded as $\kappa \to \infty$. The solution in Equation (3.50) satisfies the initial conditions

$$\eta_1 = \eta_0, \quad \frac{\mathrm{d}\eta_1}{\mathrm{d}\tilde{\tau}} = 2h\eta_0\tilde{q}^{1/2} \quad \text{at} \;\; \tilde{\tau} = 0. \tag{3.51}$$

We also consider a solution η_2 to Equation (3.41) satisfying the same initial conditions. Then, it follows from Equation (3.48) and the comparison theorem that $\eta_2 \geq \eta_1$ for $\tilde{\tau} \in [0, \tilde{\tau}_0]$. The initial conditions, Equation (3.51), may be rewritten for η_2 as

$$\eta_2 = \eta_0, \quad \frac{\mathrm{d}\eta_2}{\mathrm{d}\tau} = 2h\eta_0\kappa^{-1}q^{1/2} \quad \text{at} \;\; \tilde{\tau} = 0. \tag{3.52}$$

Considering Equation (3.52), it is straightforward that η_2 is bounded at $\tau = 0$ for $\kappa \in (0, \infty)$. From the definition of $\mathrm{d}\eta_2/\mathrm{d}\tau$ in Equation (3.52) and the definition of q in Equation (3.26), it follows that $\mathrm{d}\eta_2/\mathrm{d}\tau$ is also bounded at $\tau = 0$ for $\kappa \in (0, \infty)$. Then, it follows from the inequality $\eta_2 \geq \eta_1$ and Equation (3.50) that, for any $\tau \in (0, \arcsin h)$, there is such a solution to Equation (3.41) that it is bounded together with its first derivative at $\tau = 0$ for any value of κ, but it is unbounded at $\tau = \tau_0$ as $\kappa \to \infty$. Hence, the instability growth rate is unbounded and the initial value problem describing the evolution of the perturbed discontinuity is ill-posed when $M_A > \min\{M_{A0}\}$.

Now, we assume that $M_A < M_{A0}(\phi)$, so that, in accordance with Equation (3.39), $K > 2$ and $a > 2q$. We calculate the instability growth rate for $\kappa \gg 1$. Let $\bar{\eta}(\tau)$ be the solution to Equation (3.23), satisfying the initial conditions

$$\bar{\eta} = 1, \quad \frac{\mathrm{d}\bar{\eta}}{\mathrm{d}\tau} = 0 \quad \text{at} \quad \tau = 0. \tag{3.53}$$

Then, the characteristic exponent is defined by the equation (Abramowitz and Stegun, 1965)

$$\cosh(\pi\mu) = \bar{\eta}(\pi). \tag{3.54}$$

We use the WKB method and look for a solution to Equation (3.23) in the form $\eta_+ = \mathrm{e}^{\kappa\Theta}$. Substituting this expression into Equation (3.23) we obtain

$$\kappa^{-1}\frac{\mathrm{d}^2\Theta}{\mathrm{d}\tau^2} + \left(\frac{\mathrm{d}\Theta}{\mathrm{d}\tau}\right)^2 + \tilde{a} - 2\tilde{q}\cos(2\tau) = 0. \tag{3.55}$$

From Equation (3.53), it follows that the initial conditions for Equation (3.55) are

$$\Theta = 0, \quad \frac{\mathrm{d}\Theta}{\mathrm{d}\tau} = 0 \quad \text{at} \quad \tau = 0. \tag{3.56}$$

We look for the solution of Equation (3.55) as the perturbation expansion

$$\Theta = \Theta_1 + \kappa^{-1}\Theta_2 + \dots \tag{3.57}$$

Substituting this expansion into Equation (3.55) and collecting terms of the order of unity we obtain

$$\left(\frac{\mathrm{d}\Theta_1}{\mathrm{d}\tau}\right)^2 = 2\tilde{q}\cos(2\tau) - \tilde{a}. \tag{3.58}$$

The solution to this equation satisfying the condition $\Theta_1 = 0$ at $\tau = 0$ is

$$\Theta_1(\tau) = i\int_0^\tau \sqrt{\tilde{a} - 2\tilde{q}\cos(2\tau')}\,\mathrm{d}\tau', \tag{3.59}$$

where we chose the plus sign of the square root. It is clear that the function being integrated in Equation (3.59) is even, meaning that its integral over the interval $(0, x)$ is odd. Therefore, $\Theta_1(\tau)$ is an odd function.

In the next order approximation we collect terms of the order of κ^{-1} in Equation (3.55) to obtain

$$\frac{\mathrm{d}^2\Theta_1}{\mathrm{d}\tau^2} + \frac{\mathrm{d}\Theta_1}{\mathrm{d}\tau}\frac{\mathrm{d}\Theta_2}{\mathrm{d}\tau} = 0. \tag{3.60}$$

Using Equation (3.59) we find that the solution to this equation satisfying the condition $\Theta_2 = 0$ at $\tau = 0$ is

$$\Theta_2(\tau) = -\frac{1}{2}\ln\left(\frac{\tilde{a} - 2\tilde{q}\cos(2\tau)}{\tilde{a} - 2\tilde{q}}\right). \tag{3.61}$$

Since the function inside the natural logarithm in Equation (3.61) is even and the logarithm does not affect the parity, it follows that $\Theta_2(\tau)$ is an even function.

Recall that $\eta_-(\tau) = \eta_+(-\tau)$ is also a solution to Equation (3.23). Then, since $\Theta_1(\tau)$ is an odd function and $\Theta_2(\tau)$ is an even function, it follows that

$$\bar{\eta} = \frac{\eta_+ + \eta_-}{2} = \mathrm{e}^{\Theta_2}\cos(\kappa\Theta_1) + \mathcal{O}\big(\kappa^{-1}\big). \tag{3.62}$$

Introducing the notation $\chi = \Theta_1(\pi)$ and $\gamma = \Theta_2(\pi)$ we transform Equation (3.23) to

$$\cosh(\pi\mu) = \mathrm{e}^{\gamma}\cos(\kappa\chi). \tag{3.63}$$

When the absolute value of the right-hand side of this equation does not exceed unity the two values of μ satisfying this equation are purely imaginary and the corresponding wave mode is neutrally stable. When the absolute value of the right-hand side is larger than unity one of the two values of μ satisfying this equation has positive real part and the corresponding wave mode grows exponentially. However, we can observe that the right-hand side of Equation (3.63) is bounded for any κ. This implies that the real part of μ is also bounded, and the same is true for the growth rate. We made this conclusion for a particular value of ϕ and $M_A < M_{A0}(\phi)$. If we now assume that $M_A < \min\{M_{A0}\}$, then the growth rate of any wave mode is bounded. This means that the initial value problem describing the evolution of the discontinuity is well-posed when $M_A < \min\{M_{A0}\}$. From Equation (3.38) we see that this condition may be written in the approximate form as

$$M_A < \frac{\bar{v}_A \theta}{2} \sqrt{\frac{1 + r}{1 + r\bar{v}_A^2}}, \tag{3.64}$$

since, typically, $\theta \ll 1$.

3.4 Application to Transverse Coronal Loop Oscillations

The aim of this section is twofold. First, we further elaborate the analysis of Section 3.3 by considering the σ-stability of Equation (3.23). Afterwards, we apply some of the results obtained in Subsections 3.3.2 and 3.3.3 to the stability of coronal loop oscillations.

3.4.1 The σ-stability

We, now, use the concept of σ-stability, first introduced by Goedbloed and Sakanaka (1974) and Sakanaka and Goedbloed (1974). This concept is used in studies of thermonuclear plasma confinement where it is necessary that perturbation amplitudes remain sufficiently small on some relevant time scale. An equilibrium is σ-stable if the amplitudes of unstable perturbations grow at most like $\exp(\sigma t)$.

We apply the concept of σ-stability to the analysis of the KH instability induced by transverse oscillations of solar coronal loops. We say that a transverse coronal loop oscillation is σ-stable if the growth time of the KH instability exceeds the damping time due to resonant absorption. Let $t_D = \alpha P$ be the damping time, where $P = 2\pi/\Omega$ is the oscillation period, and α varies from 1 to 5 (see, e.g., Goddard and Nakariakov, 2016). It follows from our definition that $\sigma = 1/\Omega t_D$, or

$$\sigma = \frac{1}{2\pi\alpha}. \tag{3.65}$$

When α varies from 1 to 5, σ decreases from approximately 0.16 to 0.03. We see that, in any case, the interface cannot be σ-stable if the maximum growth rate exceeds 0.16, which implies that if the interface is σ-stable then the increment is much less than unity. It is shown in Appendix A that, in this case, the maximum growth rate for fixed ϕ is approximately equal to $1/2K$. Then, the maximum growth rate for all values of ϕ is $1/2K_m$, where $K_m = \min_\phi K$. Hence, the σ-stability condition reads

$$K_m \geq \frac{1}{2\sigma}, \quad K_m = \frac{4\min\{M_{A0}^2\}}{M_A^2} - 2. \tag{3.66}$$

To estimate K_m we take as typical values $r = 1/3$ and $\bar{v}_A^2 = 3$. Then, using Equations (3.38) and (3.66), and taking into account the fact that, typically, $\theta \ll 1$, we reduce the σ-stability criterion to

$$\theta \geq \frac{M_A}{2}\sqrt{4 + \frac{1}{\sigma}}. \tag{3.67}$$

The typical displacement of a kink-oscillating coronal loop is of the order of the loop radius. Then, the ratio of the velocity to v_{Ai} is of the order of the loop radius and length. Hence, the typical value is $M_A = 0.01$. Now, it follows from Equation (3.67) that the interface is σ-stable if $\theta \gtrsim 1°$ for $\alpha = 1$, and σ-stable if $\theta \gtrsim 2°$ for $\alpha = 5$. Even the maximum value $\theta = 2°$ corresponds to only about a half-turn of magnetic field lines from one loop footpoint to the other. Hence, the loop boundary is σ-stable for a very moderate magnetic twist.

In Figure 3.7, we present the values of μ associated with the three straight lines in Figure 3.5. We assumed that $r = 1/3$, $\bar{v}_A^2 = 3$, $M_A = 0.01$, and $\phi = \phi_0$ so that $K = K_m$. For $\theta = 0$, μ is a monotonically increasing function of κ, and perturbations with any q are unstable. The green curve corresponds to $\theta = 0.5°$, and is unbounded as $\kappa \to \infty$ since $\min M_{A0} \approx 0.0062 < M_A$. Finally, the blue curve, which corresponds to $\theta = 1°$, is bounded for $\kappa \in (0, \infty)$ since $\min M_{A0} \approx 0.0123 > M_A$. The equation of the dashed line is $\mu = 0.16$, and we see that the loop with $\theta = 1°$ is σ-stable for σ defined in Equation (3.65) with $\alpha = 1$.

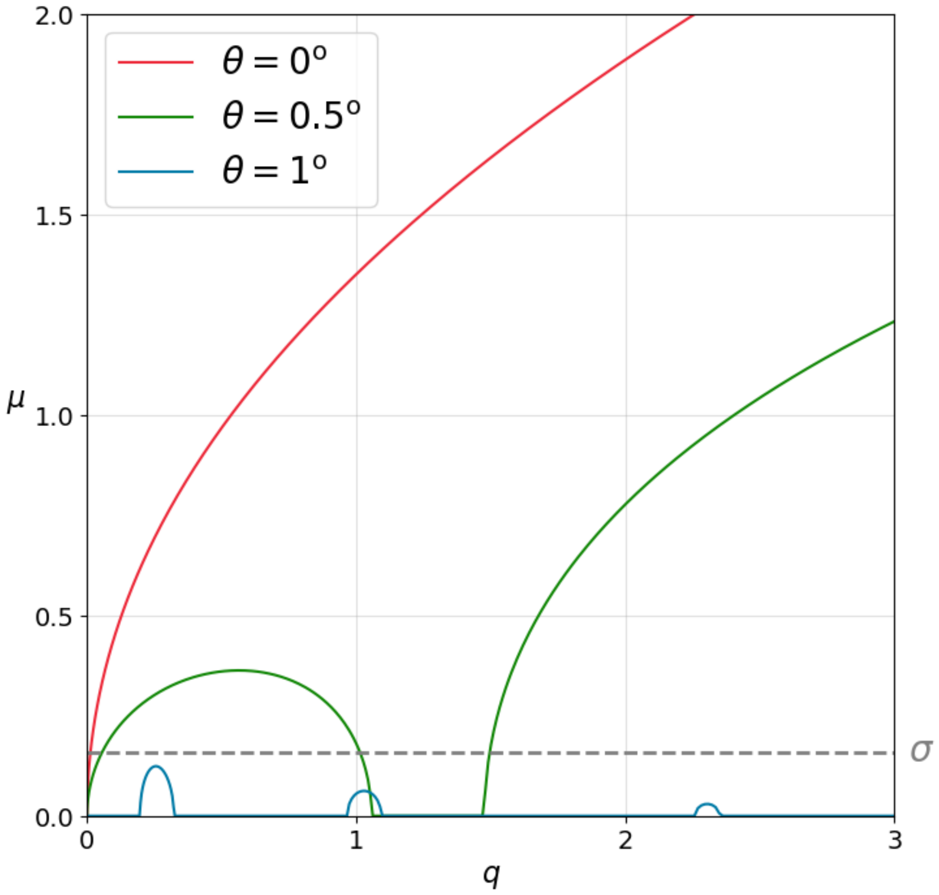

Figure 3.7: The growth rate of the instability, μ, plotted with respect to q. The red, green, and blue lines correspond to the lines in Figure 3.5a

We note that if a magnetic loop is σ-stable, then the initial value problem describing the evolution of its boundary perturbation is well-posed. However, the converse is not always true. The initial value problem is well-posed if the growth rate is bounded, but it may still be very large. On the other hand, a magnetic loop is σ-stable when the maximum growth rate is below a definite and, usually, sufficiently small number.

3.4.2 Coronal Loop Parameters

The model that we outlined in the previous sections can be only applied for the local analysis of the stability of the boundary of an oscillating magnetic tube. In this analysis, we can consider oscillations with the characteristic scale in the azimuthal direction that is much smaller than the tube radius R, and the characteristic scale in the axial direction that is much smaller than the

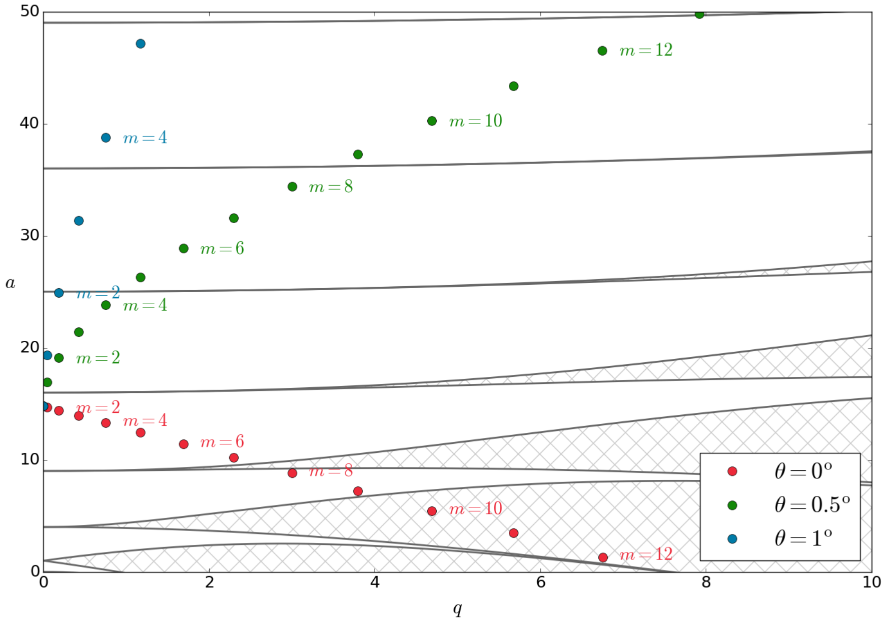

(a) $n = 1$

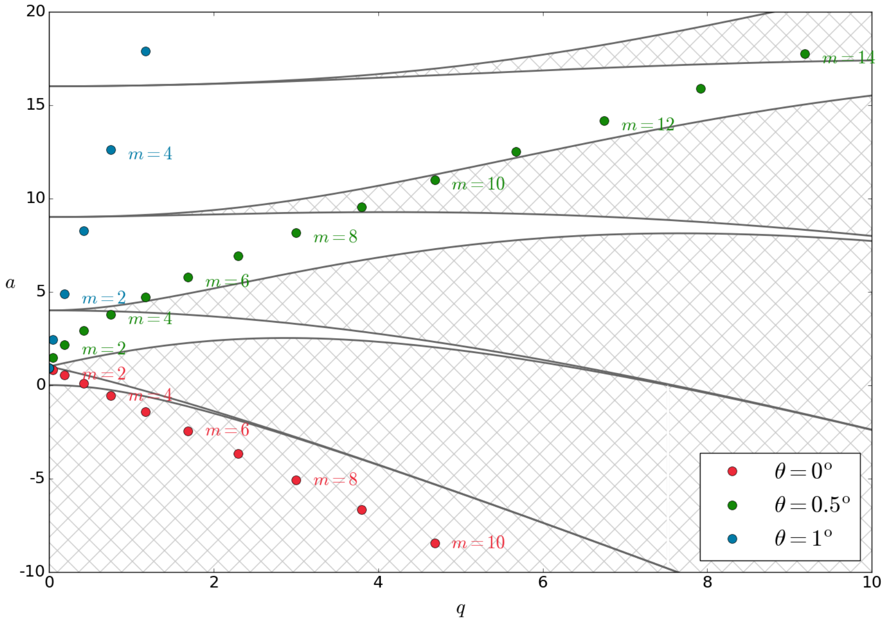

(b) $n = 4$

Figure 3.8: The dependence of the solutions on m in the qa-plane, for $M_A = 0.01$, $r = 1/3$, $\bar{v}_A^2 = 3$, $n = 1$ (top) and $n = 4$ (bottom). The red, green and blue dots correspond to increasing degrees of twist.

tube length L. Hence, we take

$$k_x = \frac{m}{R}, \quad k_z = \frac{\pi n}{L}, \tag{3.68}$$

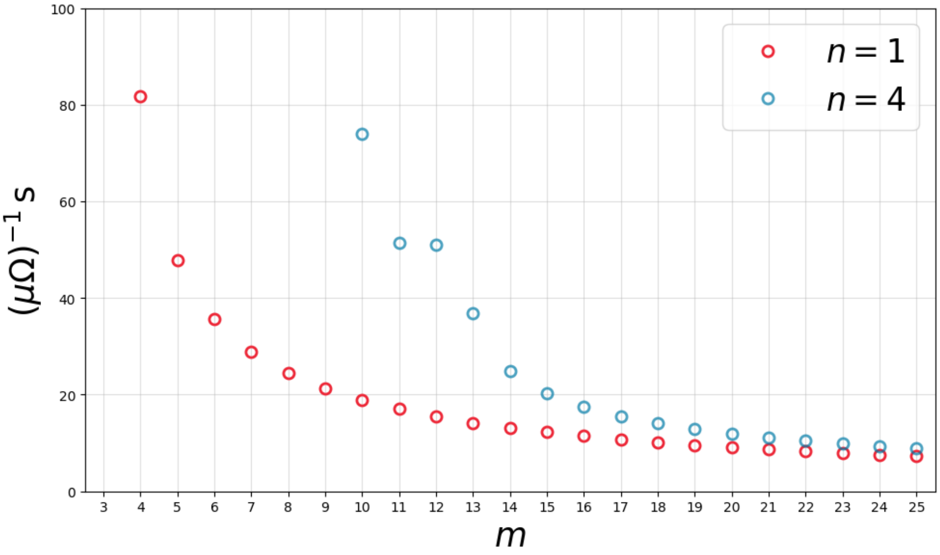

(a) $\theta = 0°$

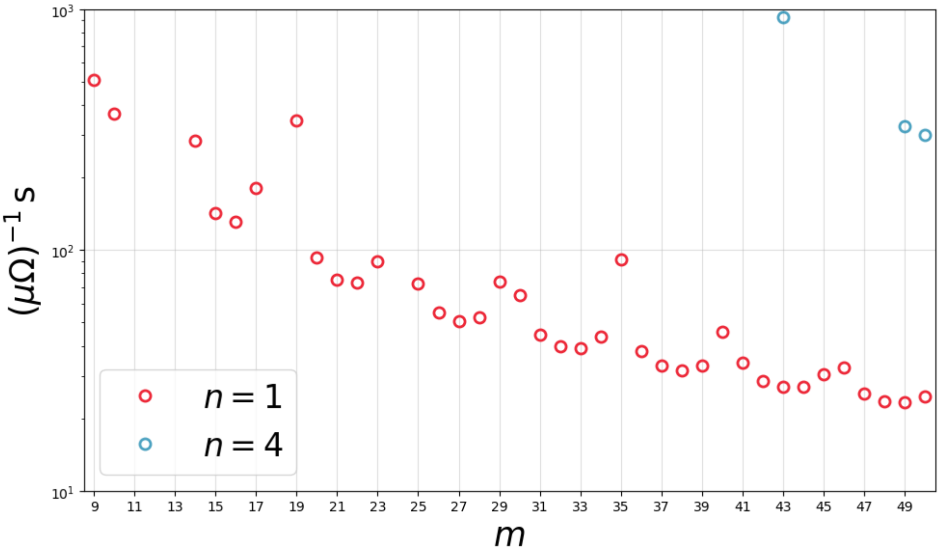

(b) $\theta = 0.5°$

Figure 3.9: The dependence of the growth rate on m for $M_A = 0.01$, $r = 1/3$, $\bar{v}_A^2 = 3$, $\theta = 0°$ (top) and $\theta = 0.5°$ (bottom). The red and blue dots correspond to $n = 1$ and $n = 4$, respectively.

where m and n are sufficiently large integer numbers. Using Equations (3.25) and (3.68) we obtain

$$k^2 = \frac{m^2}{R^2} + \frac{\pi^2 n^2}{L^2}, \quad \tan\phi = \frac{\pi n R}{mL}. \tag{3.69}$$

We assume that $n \lesssim |m|$. Since in coronal magnetic loops $R \ll L$, it follows that we may use the approximate expressions

$$k \approx \frac{|m|}{R}, \quad \phi \approx \frac{\pi n R}{mL}. \tag{3.70}$$

Throughout this section we assume that $\bar{v}_A^2 = r^{-1}$. This assumption holds if the magnitudes of the interior and exterior magnetic fields are equal, which is typically true for coronal loops. We also assume that $\theta \ll 1$. Then, we obtain the approximate expressions

$$M_{A0}^2 = \frac{1+r}{4r}\left[\left(\theta + \frac{\pi n R}{mL}\right)^2 + \frac{\pi^2 n^2 R^2}{m^2 L^2}\right], \tag{3.71}$$

$$\min\{M_{A0}^2\} = \frac{(1+r)\theta^2}{8r}. \tag{3.72}$$

The condition $M_A < \min\{M_{A0}^2\}$ gives

$$\theta > M_A\sqrt{\frac{8r}{1+r}}. \tag{3.73}$$

If we take $r = 1/3$, the right-hand side of this inequality is approximately equal to M_A, that is it is of the order of 0.01. Hence, the inequality (3.73) can be satisfied even for quite moderated twist. If the inequality is satisfied, then the IVP describing the evolution of the tube boundary is well-posed and the growth rate of perturbations is bounded.

In Figures 3.8 and 3.9, we show the dependence of the growth rate on m for $n = 1$ (left) and $n = 4$ (right), $M_A = 0.01$, $r = 1/3$, $\bar{v}_A^2 = 3$, $R/L = 200$, and $\theta = 0°$ (red), $\theta = 0.5°$ (green) and $\theta = 1°$ (blue). We note that, obviously, $n = 1$ does not satisfy the condition that n is large, so we considered $n = 1$ only for comparison. While, for $n = 1$, the points in the qa-plane corresponding to $\theta = 0°$ are virtually unchanged as compared to the line in Figure 3.6, for $n = 4$ they are shifted upwards considerably. This is also the case for $\theta = 0.5°$. We see that for $n = 1$ there are some modes which are unstable in the range selected, for $n = 4$ there are no such modes. There may be unstable modes for $\theta = 0.5°$ and $n = 4$, but only for very large m. In terms of the IVP, for $\theta = 1°$, corresponding to a well-posed solution, no value of m corresponds to an unstable solution in the qa-plane. In general, well-posed solutions seem to be unstable only for very large m. These results are significant since they suggest that very localised longitudinal perturbations of the flux tube are generally more stable.

3.5 Summary and Discussion

In this work, we performed the first analytical study of the transverse wave induced Kelvin-Helmholtz instability of solar coronal loops. We modelled the region on the loop boundary where the shear flows are the greatest as a tangential discontinuity separating time-periodic counter-streaming flows. To model the magnetic twist in coronal loops we assumed that the equilibrium magnetic fields on either side of the discontinuity are not parallel. The flow velocities at the two sides of the discontinuity have opposite directions and equal magnitudes oscillating harmonically. For the sake of mathematical simplicity, we assumed that the plasma on both sides of the interface is incompressible. Using the linearised set of ideal MHD equations, we derived the governing equation describing the evolution of the shape of the tangential discontinuity, known as Mathieu's equation.

We employed Mathieu's equation to study the stability of the discontinuity. For comparison, we first presented the results of the stability analysis in the case of steady flows, which we obtained by setting the flow oscillation frequency to zero. In this case, the stability of the discontinuity is determined by the Alfvén Mach number, which is defined as the ratio of the background velocity magnitude to the Alfvén speed at one side of the interface. The discontinuity is unstable when the Alfvén Mach number exceeds a critical value, and the instability growth rate is proportional to the wavenumber, and thus unbounded. This implies that the initial value problem describing the evolution of the perturbed discontinuity is ill-posed. We note that the critical Alfvén number is zero when there is no magnetic shear.

In contrast to the interface separating steady flows, the tilted magnetic field cannot stabilise the discontinuity if the flows oscillate. A similar result was obtained by Roberts (1973) in the case of MHD tangential discontinuity with the magnetic field having the same direction at both sides and the flow velocity parallel to the magnetic field.

Even though the interface is always unstable, the critical Alfvén Mach number still plays an important role in the stability properties. We showed that the growth rate of the instability is unbounded when the Alfvén Mach number exceeds the instability threshold, and thus the initial value problem is ill-posed. Hence, in this case the stability properties are qualitatively the same as in the case of steady flows. On the other hand, when the Alfvén Mach number is below its critical value, the instability increment is bounded, and the initial value problem is well-posed.

In Section 3.4.1, we applied the concept of σ-stability to kink oscillating coronal loops, which states that the loop is σ-stable if the growth time of the instability exceeds the resonant damping time of the transverse oscillation.

We obtained the criterion for the σ-stability and showed that, for parameters typical for transverse coronal loop oscillations, even moderate magnetic twist makes the loop boundary σ-stable.

In Section 3.4.2, we used our model to perform a local stability analysis of the sections of the loop boundary where the amplitudes of the shear flows are the greatest (see Figures 3.1 and 3.2). The local analysis is only valid for perturbations with the azimuthal wavelength much smaller than the radius of the loop cross-section R, and the axial wavelength much smaller than the loop length L. In accordance with these latter assumptions, we took $k_x = m/R$ and $k_z = \pi n/L$, where k_x is the component of the wave vector in the azimuthal direction, and k_z is the component of the wave vector in the axial direction, and $|m|$ and n are positive integer numbers. We note that, while n is positive, m can be either positive or negative. We found that the nature of solutions is changed by this new definition of the parameters. While, previously, all solutions were unstable regardless of the background parameters, the discretisation of the parameter space has introduced the possibility that unstable solutions exist only for sufficiently large values of $|m|$.

Finally, we note that our study does not include the effects of strong shear induced by resonant absorption, which may be significant in the generation of the KHI, as suggested by Howson et al. (2017*a*) and Terradas et al. (2018).

CHAPTER 4

Conclusions

4.1 Overview of Thesis

This Thesis constitutes a study of magnetoacoustic waves and the magnetohydrodynamic Kelvin-Helmholtz instability of two novel equilibrium configurations. Chapter 1 introduces the background material needed to develop the new theory. The equations of ideal magnetohydrodynamics are derived from Maxwell's equations and the equations of gas dynamics. Subsequently, the basic theory of MHD waves is derived from the ideal linear MHD equations, and the Kelvin-Helmholtz instability and its possible applications to solar physics are introduced.

The first of the two novel models is studied in Chapter 2. The equilibrium configuration being investigated is that of a steady slab of magnetised plasma subject to a steady flow, embedded in a non-magnetic atmosphere, with different background parameters on each side of the slab. This configuration differs from those in previous models since it considers both a steady flow within the slab, as well as asymmetry of the exterior parameters. A dispersion relation for magnetoacoustic waves propagating along the slab is derived and its solutions are obtained in both approximate analytical form, and in general numerical form. Applications to solar physics are discussed in the context of determining the parameters of Kelvin-Helmholtz unstable flanks of coronal mass ejections.

The second model is investigated in Chapter 3. It involves the study of an interface separating temporally oscillating background plasmas in a magnetic environment. The analytical study of transient flows in MHD has been rather uncommon due to the difficulty of obtaining results in closed form. However, utilising the incompressible plasma approximation allowed us to obtain the governing equation of the stability of the boundary in the form of Mathieu's equation. We studied the general stability of its solutions as well as the nature of the initial value problem for the given form of the parameters. An applications to the transverse wave induced Kelvin-Helmholtz instability in coronal loops using this model is also presented in this Chapter.

4.2 Summary of Results

4.2.1 Chapter 2

The dispersion relation of waves propagating along a steady slab in an asymmetric environment was obtained in Subsection 2.2.3, and the possible modes of propagation are classified in terms of the characteristic speeds in Subsection 2.2.5. The analytical solutions of the dispersion relation in the incompressible plasma limit and the thin and wide slab approximations are obtained in Section 2.3. General numerical solutions are obtained in Section 2.4 and it is found that the modes are consistent with the classification in terms of the characteristic speeds from Subsection 2.2.5. The Kelvin-Helmholtz threshold value for the most unstable mode, the slow surface kink mode, is also obtained in Section 2.4 and it is found that the asymmetry in background density may significantly lower the threshold value for thin slabs. Finally, we estimate the densities of a Kelvin-Helmholtz unstable flank of a coronal mass ejection in Section 2.5. We find that the flank of the CME is at least three orders of magnitude denser than the background corona for the observed parameters of the KHI.

4.2.2 Chapter 3

The governing relation of the stability of a boundary separating temporally oscillating flows is found to be Mathieu's equation in Section 3.2. In order to better understand the stability of the boundary separating oscillating flows at an angle, we first study the stability of steady flows at an angle in Subsection 3.3.1. We find that the initial value problem in this case is ill-posed regardless of the magnitude of the flow. The stability of the transient configuration is studied in Subsection 3.3.2, and it is found that solutions are always unstable for some value of the wavenumber magnitude. The initial value problem is found to be ill-posed when the flow magnitude is above a certain threshold and well-posed when it is below this threshold. The application of the results of this model are applied to the study of the KHI of transverse coronal loop oscillations in Section 3.4. In Subsection 3.4.1 we introduce the concept of σ-stability and find the analytical condition for coronal loops to be σ-stable.

Finally, in Subsection 3.4.2 we introduce a new set of parameters which should generalise the local stability analysis to the three dimensional and cylindrical nature of coronal loops. We find that coronal loops are always unstable to the KHI, but may become σ-stable if there is magnetic twist present.

4.3 Future Work

A natural extension to the investigation performed in Chapter 2 would be to introduce parallel magnetic fields of different magnitudes in the exterior regions of the slab. This would significantly alter the classification of the modes of propagation with respect to the characteristic speeds since there would be two new Alfvén speeds.

A different possible direction would be to replace the boundaries of the slab with thin regions of linear density change. The slab would, therefore, no longer be delimited by tangential discontinuities, but by linear density transition regions. This would severely complicate the analysis since the linear change in density introduces a singularity in the Alfvén speed.

The model in Chapter 3 may be extended by including a linear decrease of the flow from one side of the interface to the other. Similarly, a linear decrease in density could also be considered, which would let us study the effects of resonant absorption on the instability. Incorporating both of the aforementioned modifications would yield a model closer to what we believe is the structure of a coronal loop. However, such a model is bound to be mathematically very complex and there is no assurance that a governing equation can be obtained analytically.

A different avenue of exploration is that of the application of the existing model, with only minor modifications, to other solar and magnetospheric phenomena. A potential application would be to kink oscillations of solar prominences. An important differences between solar prominences and coronal loops is that the plasma in the former may not be fully ionized. This effect would have to be taken into account in the model.

APPENDIX A

The Maximum Growth Rate

As we have already stated before, the characteristic exponent, μ, is determined by the equation

$$\cosh(\pi\mu) = \bar{\eta}(\pi), \tag{A.1}$$

where $\bar{\eta}(\tau)$ is the solution to the initial value problem to Equation (3.23) with

$$\bar{\eta} = 1, \quad \frac{\mathrm{d}\bar{\eta}}{\mathrm{d}t} = 0 \quad \text{at} \;\; \tau = 0, \tag{A.2}$$

(Abramowitz and Stegun, 1965). When a perturbation is unstable, its growth rate is given by $\gamma = \Re(\mu)$. In the context of the σ-stability analysis, we assume that the growth time of the instability is much larger than the oscillation period. In terms of dimensionless quantities, this condition is written as $\gamma \ll 1$. The numerical investigation shows that this condition is only satisfied for all values of q when $K \gg 1$. In accordance with this, we introduce the small parameter $\epsilon = 1/K$. Figure 3.5 shows that a is close to j^2 on parts of the line $a = Kq$ corresponding to unstable perturbations when $K \gg 1$, where $j = 1, 2, \dots$. We obtain $a = j^2$ taking $q = j^2\epsilon$, which implies that $q = \mathcal{O}(\epsilon)$.

First we study the case with $j = 1$. Using the expansion valid for small q (Abramowitz and Stegun, 1965),

$$a_1(q) = 1 + q + \mathcal{O}(q^2), \quad b_1(q) = 1 - q + \mathcal{O}(q^2), \tag{A.3}$$

we obtain that the line $a = Kq$ in Figure 3.5 intersects the curves $a = b_1(q)$ and $a = a_1(q)$ at $q \approx \epsilon - \mathcal{O}(\epsilon^2)$ and $q \approx \epsilon + \mathcal{O}(\epsilon^2)$, respectively. Then $q = \epsilon + \bar{q}\epsilon^2$ on the part of the curve $a = Kq$ between the intersection points, where $\bar{q}$ is a free parameter varying from approximately -1 to approximately 1. It follows that $q = \epsilon + \bar{q}\epsilon^2$ on the line $a = Kq$ between the intersection points, where $\bar{q}$ is a free parameter. The equation of the curve $a = Kq$ is now rewritten as $a = 1 + \bar{q}\epsilon$, and Equation (3.23) becomes

$$\frac{\mathrm{d}^2\eta}{\mathrm{d}\tau^2} + [1 + \bar{q}\epsilon - 2(\epsilon + \bar{q}\epsilon^2)(\cos(2\tau)]\eta = 0. \tag{A.4}$$

To calculate the increment we need to find the solution $\bar{\eta}(\tau)$ to this equation satisfying the initial conditions Equation (A.2). To do this we use the regular perturbation method with

$$\bar{\eta} = \bar{\eta}^{(0)} + \bar{\eta}^{(1)} + \bar{\eta}^{(2)} + \dots. \tag{A.5}$$

Substituting Equation (A.5) into Equations (A.2) and (A.4), and collecting the terms of the order of unity, we obtain

$$\frac{\mathrm{d}^2\bar{\eta}^{(0)}}{\mathrm{d}\tau^2} + \bar{\eta}^{(0)} = 0, \tag{A.6}$$

and the associated initial conditions

$$\bar{\eta}^{(0)} = 1, \quad \frac{\mathrm{d}\bar{\eta}^{(0)}}{\mathrm{d}\tau} = 0 \quad \text{at} \ \ \tau = 0. \tag{A.7}$$

The solution to this initial value problem is

$$\bar{\eta}^{(0)} = \cos\tau. \tag{A.8}$$

Collecting term of the order of ϵ yields

$$\frac{\mathrm{d}^2\bar{\eta}^{(1)}}{\mathrm{d}\tau^2} + \bar{\eta}^{(1)} = [2\cos(2\tau) - \bar{q}]\cos\tau, \tag{A.9}$$

$$\bar{\eta}^{(1)} = 0, \quad \frac{\mathrm{d}\bar{\eta}^{(1)}}{\mathrm{d}\tau} = 0 \quad \text{at} \ \ \tau = 0. \tag{A.10}$$

After straightforward calculation we obtain

$$\bar{\eta}^{(1)} = \frac{1-\bar{q}}{2}\tau\sin\tau - \frac{1}{8}\cos(3\tau) + \frac{1}{8}\cos\tau. \tag{A.11}$$

Finally we collect terms of the order of ϵ^2 to obtain

$$\frac{\mathrm{d}^2\bar{\eta}^{(2)}}{\mathrm{d}\tau^2} + \bar{\eta}^{(2)} = [2\cos(2\tau) - \bar{q}]\eta_1^{(1)} + 2\bar{q}\cos(2\tau)\cos\tau, \tag{A.12}$$

$$\bar{\eta}^{(2)} = 0, \quad \frac{\mathrm{d}\bar{\eta}^{(2)}}{\mathrm{d}\tau} = 0 \quad \text{at} \ \ \tau = 0. \tag{A.13}$$

The solution to this initial value problem is given by

$$\begin{aligned} \bar{\eta}^{(2)} &= \frac{1-\bar{q}^2}{8}\tau^2\cos\tau + \frac{2\bar{q}^2 + 7\bar{q} - 2}{16}\tau\sin\tau - \frac{1-\bar{q}}{16}\tau\sin(3\tau) \\ &+ \frac{\cos(5\tau)}{192} - \frac{2+3\bar{q}}{32}\cos(3\tau) + \frac{11+18\bar{q}}{192}\cos\tau. \end{aligned} \tag{A.14}$$

Using Equations (A.8), (A.11), and (A.14) we obtain

$$\bar{\eta}(\pi) = -1 - \frac{1-\bar{q}^2}{8}\pi^2\epsilon^2 + \mathcal{O}(\epsilon^3). \tag{A.15}$$

It follows from this equation that

$$\mu = i \pm \frac{\epsilon}{2}\sqrt{1-\bar{q}^2} + \mathcal{O}(\epsilon^2). \tag{A.16}$$

This result implies that

$$\gamma = \frac{\epsilon}{2}\sqrt{1-\bar{q}^2} + \mathcal{O}(\epsilon^2), \quad \gamma_m = \frac{\epsilon}{2}, \tag{A.17}$$

where γ_m is the maximum value of the instability increment when the point (a, q) is on the part of line $a = Kq$ that is between the curves $a = b_1(q)$ and $a = a_1(q)$.

Now we consider the part of line $a = Kq$ that is between the curves $a = b_j(q)$ and $a = a_j(q)$, $j = 2, 3, \dots$ For $q \ll 1$ we have $b_1(q) = n^2 + \mathcal{O}(q^2)$ and $a_1(q) = n^2 + \mathcal{O}(q^2)$ (Abramowitz and Stegun, 1965). Since $K = \epsilon^{-1}$, it follows that $q = n^2\epsilon(1 + \bar{q}\epsilon^2)$ and $a = n^2(1 + \bar{q}\epsilon^2)$, where $\bar{q}$ is again a free parameter. Substituting these expressions in Eq. (A.1) we transform it to

$$\frac{\mathrm{d}^2\eta}{\mathrm{d}\tau^2} + j^2[1 + \bar{q}\epsilon^2 - 2(\epsilon + \bar{q}\epsilon^3)(\cos(2\tau)]\eta = 0. \tag{A.18}$$

Then we again look for the solution in the form of the expansion given by Eq. (A.5). Substituting this expansion in Equations (3.23) and (A.2), and collecting terms of the order of unity we obtain

$$\frac{\mathrm{d}^2\bar{\eta}^{(0)}}{\mathrm{d}\tau^2} + j^2\bar{\eta}^{(0)} = 0, \tag{A.19}$$

$$\bar{\eta}^{(0)} = 1, \quad \frac{\mathrm{d}\bar{\eta}^{(0)}}{\mathrm{d}\tau} = 0 \quad \text{at} \quad \tau = 0. \tag{A.20}$$

The solution to this initial value problem is

$$\bar{\eta}^{(0)} = \cos(j\tau). \tag{A.21}$$

Collecting terms of the order of ϵ yields

$$\frac{\mathrm{d}^2\bar{\eta}^{(1)}}{\mathrm{d}\tau^2} + j^2\bar{\eta}^{(1)} = 2j^2\cos(2\tau)\cos(j\tau), \tag{A.22}$$

$$\bar{\eta}^{(1)} = 0, \quad \frac{\mathrm{d}\bar{\eta}^{(1)}}{\mathrm{d}\tau} = 0 \quad \text{at} \quad \tau = 0. \tag{A.23}$$

After straightforward calculation we obtain

$$\bar{\eta}^{(1)} = 1 - \frac{1}{3}\cos(4\tau) - \frac{2}{3}\cos(2\tau) \tag{A.24}$$

for $j = 2$, and

$$\bar{\eta}^{(1)} = \frac{j^2\cos[(j-2)\tau]}{4(j-1)} - \frac{j^2\cos[(j+2)\tau]}{4(j+1)} - \frac{n^2\cos(j\tau)}{2(j^2-1)} \tag{A.25}$$

for $j > 2$. Collecting terms of the order of ϵ^2 we obtain

$$\frac{\mathrm{d}^2\bar{\eta}^{(2)}}{\mathrm{d}\tau^2} + \bar{\eta}^{(2)} = 2j^2\bar{\eta}^{(1)}\cos(2\tau) - j^2\bar{q}\cos(j\tau), \tag{A.26}$$

$$\bar{\eta}^{(2)} = 0, \quad \frac{\mathrm{d}\bar{\eta}^{(2)}}{\mathrm{d}\tau} = 0 \quad \text{at} \ \ \tau = 0. \tag{A.27}$$

The solution to this initial value problem is given by

$$\bar{\eta}^{(2)} = \left(\frac{5}{3} - \bar{q}\right)\tau\sin(2\tau) + \frac{\cos(6\tau)}{24} + \frac{2}{9}\cos(4\tau) + \frac{29}{72}\cos(2\tau) - \frac{2}{3} \tag{A.28}$$

for $j = 2$, and by

$$\begin{aligned} \bar{\eta}^{(2)} &= \frac{j}{4}\left(\frac{j^2}{j^2-1}\right)\tau\sin(j\tau) + \frac{j^4\cos[(j+4)\tau]}{32(j+1)(j+2)} + \frac{j^4\cos[(j+2)\tau]}{8(j+1)(j^2-1)} \\ &- \frac{j^4(j^4-3j^2+16)\cos(j\tau)}{16(j^2-1)^2(j^2-4)} - \frac{j^4\cos[(j-2)\tau]}{8(j-1)(j^2-1)} + \frac{j^4\cos[(j+4)\tau]}{32(j-1)(j-2)} \end{aligned} \tag{A.29}$$

for $j > 2$. Using Eqs. (A.21), (A.24), (A.25), (A.28), and (A.29), we obtain

$$\bar{\eta}(\pi) = (-1)^n + \mathcal{O}(\epsilon^3). \tag{A.30}$$

It follows from this equation that $\mu = \mathcal{O}(\epsilon^3)$ for even j and $\mu = i + \mathcal{O}(\epsilon^3)$ for odd j, and thus $\gamma = \mathcal{O}(\epsilon^{3/2})$, that is $\gamma \ll \gamma_m$. Hence, $\gamma_m = 1/2K$ is the maximum value of the instability increment with respect to q when $K = \epsilon^{-1}$.

Bibliography

Abramowitz, M. and Stegun, I. A. (1965), *Handbook of mathematical functions with formulas, graphs, and mathematical tables.*

Allcock, M. and Erdélyi, R. (2017), 'Magnetohydrodynamic waves in an asymmetric magnetic slab', *Solar Physics* **292**(2), 35.

Allcock, M. and Erdélyi, R. (2018), 'Solar Magnetoseismology with Magnetoacoustic Surface Waves in Asymmetric Magnetic Slab Waveguides', *Astrophys. J.* **855**, 90.

Anfinogentov, S. A., Nakariakov, V. M. and Nisticò, G. (2015), 'Decayless low-amplitude kink oscillations: a common phenomenon in the solar corona?', *Astron. Astrophys.* **583**, A136.

Anfinogentov, S., Nisticò, G. and Nakariakov, V. M. (2013), 'Decay-less kink oscillations in coronal loops', *Astron. Astrophys.* **560**, A107.

Antolin, P., De Moortel, I., Van Doorsselaere, T. and Yokoyama, T. (2016), 'Modeling Observed Decay-less Oscillations as Resonantly Enhanced Kelvin-Helmholtz Vortices from Transverse MHD Waves and Their Seismological Application', *Astrophys. J. Lett.* **830**, L22.

Antolin, P., Yokoyama, T. and Van Doorsselaere, T. (2014), 'Fine Strand-like Structure in the Solar Corona from Magnetohydrodynamic Transverse Oscillations', *Astrophys. J. Lett.* **787**, L22.

Aschwanden, M. J. (2004), *Physics of the Solar Corona. An Introduction.*

Aschwanden, M. J., Fletcher, L., Schrijver, C. J. and Alexander, D. (1999), 'Coronal Loop Oscillations Observed with the Transition Region and Coronal Explorer', *Astrophys. J.* **520**, 880–894.

Avrett, E. H. and Loeser, R. (2008), 'Models of the Solar Chromosphere and Transition Region from SUMER and HRTS Observations: Formation of the Extreme-Ultraviolet Spectrum of Hydrogen, Carbon, and Oxygen', *The Astrophysical Journal Supplement Series* **175**.

Barbulescu, M. and Erdélyi, R. (2018), 'Magnetoacoustic waves and the kelvin–helmholtz instability in a steady asymmetric slab', *Solar Physics* **293**(6), 86.

Bennett, K., Roberts, B. and Narain, U. (1999), 'Waves in Twisted Magnetic Flux Tubes', *Solar Phys.* **185**, 41–59.

Berger, T. E., Slater, G., Hurlburt, N., Shine, R., Tarbell, T., Title, A., Lites, B. W., Okamoto, T. J., Ichimoto, K., Katsukawa, Y., Magara, T., Suematsu, Y. and Shimizu, T. (2010), 'Quiescent Prominence Dynamics Observed with the Hinode Solar Optical Telescope. I. Turbulent Upflow Plumes', *The Astrophysical Journal* **716**, 1288–1307.

Blaauwgeers, R., Eltsov, V. B., Eska, G., Finne, A. P., Haley, R. P., Krusius, M., Ruohio, J. J., Skrbek, L. and Volovik, G. E. (2002), 'Shear Flow and Kelvin-Helmholtz Instability in Superfluids', *Phys. Rev. Lett.* **89**, 155301.

Bloecker, T. (1995), 'Stellar evolution of low and intermediate-mass stars. I. Mass loss on the AGB and its consequences for stellar evolution.', *Astron. Astrophys.* **297**, 727.

Bogdanova, M., Zhelyazkov, I., Joshi, R. and Chandra, R. (2018), 'Solar jet on 2014 April 16 modeled by Kelvin-Helmholtz instability', *New Astronomy* **63**, 75–87.

Bouvier, A. and Wadhwa, M. (2010), 'The age of the Solar System redefined by the oldest Pb-Pb age of a meteoritic inclusion', *Nature Geoscience* **3**, 637–641.

Boyd, T. J. M. and Sanderson, J. J. (2003), *The Physics of Plasmas*.

Braginskii, S. I. (1965), 'Transport Processes in a Plasma', *Reviews of Plasma Physics* **1**, 205.

Browning, P. K. and Priest, E. R. (1984), 'Kelvin-Helmholtz instability of a phased-mixed Alfven wave', *Astron. Astrophys.* **131**, 283–290.

Cairns, R. A. (1979), 'The role of negative energy waves in some instabilities of parallel flows', *Journal of Fluid Mechanics* **92**(1), 1–14.

Capitaine, N., Klioner, S. and McCarthy, D. (2012), The re-definition of the astronomical unit of length:reasons and consequences, *in* 'IAU Joint Discussion 7: Space-Time Reference Systems for Future Research at IAU General Assembly-Beijing.', Vol. 7.

Chandrasekhar, S. (1961), *Hydrodynamic and hydromagnetic stability.*

Chapman, S. and Cowling, T. G. (1970), *The mathematical theory of non-uniform gases. an account of the kinetic theory of viscosity, thermal conduction and diffusion in gases.*

Coddington, E. A. and Levinson, N. (1955), *Theory of ordinary differential equations*, Tata McGraw-Hill Education.

Cram, L. E. and Wilson, P. R. (1975), 'Hydromagnetic Waves in Structured Magnetic Fields', *Solar Phys.* **41**, 313–327.

De Moortel, I. and Nakariakov, V. M. (2012), 'Magnetohydrodynamic waves and coronal seismology: an overview of recent results', *Philosophical Transactions of the Royal Society of London Series A* **370**, 3193–3216.

Defouw, R. J. (1976), 'Wave Propagation Along a Magnetic Tube', *The Astrophysical Journal* **209**, 266–269.

Drazin, P. (2015), DYNAMICAL METEOROLOGY — Kelvin–Helmholtz Instability, *in* G. R. North, J. Pyle and F. Zhang, eds, 'Encyclopedia of Atmospheric Sciences (Second Edition)', second edition edn, Academic Press, Oxford, pp. 343 – 346.

Duckenfield, T., Anfinogentov, S. A., Pascoe, D. J. and Nakariakov, V. M. (2018), 'Detection of the Second Harmonic of Decay-less Kink Oscillations in the Solar Corona', *Astrophys. J. Lett.* **854**, L5.

Dymova, M. V. and Ruderman, M. S. (2006), 'Resonantly damped oscillations of longitudinally stratified coronal loops', *Astron. Astrophys.* **457**, 1059–1070.

Edwin, P. M. and Roberts, B. (1982), 'Wave Propagation in a Magnetically Structured Atmosphere - Part Three - the Slab in a Magnetic Environment', *Solar Phys.* **76**, 239–259.

Edwin, P. M. and Roberts, B. (1983), 'Wave Propagation in a Magnetic Cylinder', *Solar Physics* **88**, 179–191.

Erdélyi, R. and Fedun, V. (2006), 'Sausage MHD Waves in Incompressible Flux Tubes with Twisted Magnetic Fields', *Solar Phys.* **238**, 41–59.

Erdélyi, R. and Fedun, V. (2007), 'Linear MHD Sausage Waves in Compressible Magnetically Twisted Flux Tubes', *Solar Phys.* **246**, 101–118.

Erdélyi, R. and Fedun, V. (2010), 'Magneto-Acoustic Waves in Compressible Magnetically Twisted Flux Tubes', *Solar Phys.* **263**, 63–85.

Foullon, C., Verwichte, E., Nakariakov, V. M., Nykyri, K. and Farrugia, C. J. (2011), 'Magnetic Kelvin-Helmholtz Instability at the Sun', *The Astrophysical Journal Letters* **729**, L8.

Foullon, C., Verwichte, E., Nykyri, K., Aschwanden, M. J. and Hannah, I. G. (2013), 'Kelvin-Helmholtz Instability of the CME Reconnection Outflow Layer in the Low Corona', *The Astrophysical Journal* **767**, 170.

Goddard, C. R. and Nakariakov, V. M. (2016), 'Dependence of kink oscillation damping on the amplitude', *Astron. Astrophys.* **590**, L5.

Goedbloed, J. P. (2009*a*), 'New construction of the magnetohydrodynamic spectrum of stationary plasma flows. I. Solution path and alternator', *Physics of Plasmas* **16**(12), 122110.

Goedbloed, J. P. (2009*b*), 'New construction of the magnetohydrodynamic spectrum of stationary plasma flows. II. Rayleigh-Taylor and Kelvin-Helmholtz instability', *Physics of Plasmas* **16**(12), 122111.

Goedbloed, J. P. (2018*a*), 'The Spectral Web of stationary plasma equilibria. I. General theory', *Physics of Plasmas* **25**, 032109.

Goedbloed, J. P. (2018*b*), 'The Spectral Web of stationary plasma equilibria. II. Internal modes', *Physics of Plasmas* **25**, 032110.

Goedbloed, J. P. H. and Poedts, S. (2004), *Principles of Magnetohydrodynamics*.

Goedbloed, J. P. and Sakanaka, P. H. (1974), 'New approach to magnetohydrodynamic stability: I. A practical stability concept', *Physics of Fluids* **17**, 908–918.

Goossens, M. (2003), *An introduction to plasma astrophysics and magnetohydrodynamics*, Vol. 294.

Goossens, M., Andries, J. and Aschwanden, M. J. (2002), ‘Coronal loop oscillations. An interpretation in terms of resonant absorption of quasi-mode kink oscillations’, *Astron. Astrophys.* **394**, L39–L42.

Goossens, M., Erdélyi, R. and Ruderman, M. S. (2011), ‘Resonant MHD Waves in the Solar Atmosphere’, *Space Sci. Rev.* **158**, 289–338.

Haberreiter, M., Schmutz, W. and Kosovichev, A. G. (2008), ‘Solving the Discrepancy between the Seismic and Photospheric Solar Radius’, *Astrophys. J.* **675**.

Hasegawa, H., Fujimoto, M., Phan, T.-D., Reme, H., Balogh, A., Dunlop, M., Hashimoto, C. and TanDokoro, R. (2004), ‘Transport of solar wind into Earth’s magnetosphere through rolled-up Kelvin-Helmholtz vortices’, *Nature* **430**(7001), 755.

Hetherington, B. (1996), *A chronicle of pre-telescopic astronomy.*

Heyvaerts, J. and Priest, E. R. (1983), ‘Coronal heating by phase-mixed shear Alfven waves.’, *Astron. Astrophys.* **117**, 220–234.

Hindman, B. W. and Jain, R. (2014), ‘An Interpretation of Flare-induced and Decayless Coronal-loop Oscillations as Interference Patterns’, *Astrophys. J.* **784**, 103.

Hollweg, J. V. and Yang, G. (1988), ‘Resonance absorption of compressible magnetohydrodynamic waves at thin “surfaces”’, *Journal of Geophysical Research* **93**, 5423–5436.

Hood, A. W. and Priest, E. R. (1979), ‘Kink instability of solar coronal loops as the cause of solar flares’, *Solar Phys.* **64**, 303–321.

Howson, T. A., De Moortel, I. and Antolin, P. (2017*a*), ‘Energetics of the Kelvin-Helmholtz instability induced by transverse waves in twisted coronal loops’, *Astron. Astrophys.* **607**, A77.

Howson, T. A., De Moortel, I. and Antolin, P. (2017*b*), ‘The effects of resistivity and viscosity on the Kelvin- Helmholtz instability in oscillating coronal loops’, *Astron. Astrophys.* **602**, A74.

Joarder, P. S., Nakariakov, V. M. and Roberts, B. (1997), ‘A Manifestation of Negative Energy Waves in the Solar Atmosphere’, *Solar Physics* **176**, 285–297.

Karampelas, K. and Van Doorsselaere, T. (2018), 'Simulations of fully deformed oscillating flux tubes', *Astron. Astrophys.* **610**, L9.

Karampelas, K., Van Doorsselaere, T. and Antolin, P. (2017), 'Heating by transverse waves in simulated coronal loops', *Astron. Astrophys.* **604**, A130.

Kelly, R. E. (1965), 'The stability of unsteady Kelvin-Helmholtz flow', *Journal of Fluid Mechanics* **22**, 547–560.

Klimchuk, J. A., Antiochos, S. K. and Norton, D. (2000), 'Twisted Coronal Magnetic Loops', *Astrophys. J.* **542**, 504–512.

Kruskal, M. D., Johnson, J. L., Gottlieb, M. B. and Goldman, L. M. (1958), 'Hydromagnetic Instability in a Stellarator', *Physics of Fluids* **1**, 421–429.

Kuridze, D., Zaqarashvili, T. V., Henriques, V., Mathioudakis, M., Keenan, F. P. and Hanslmeier, A. (2016), 'Kelvin-Helmholtz Instability in Solar Chromospheric Jets: Theory and Observation', *The Astrophysical Journal* **830**, 133.

Lodders, K. (2003), 'Solar System Abundances and Condensation Temperatures of the Elements', *Astrophys. J.* **591**, 1220–1247.

Magyar, N. and Van Doorsselaere, T. (2016*a*), 'Damping of nonlinear standing kink oscillations: a numerical study', *Astron. Astrophys.* **595**, A81.

Magyar, N. and Van Doorsselaere, T. (2016*b*), 'The Instability and Non-existence of Multi-stranded Loops When Driven by Transverse Waves', *Astrophys. J.* **823**, 82.

Malanushenko, A., Longcope, D. W. and McKenzie, D. E. (2009), 'Reconstructing the Local Twist of Coronal Magnetic Fields and the Three- Dimensional Shape of the Field Lines from Coronal Loops in Extreme-Ultraviolet and X-Ray Images', *Astrophys. J.* **707**, 1044–1063.

Malanushenko, A., Yusuf, M. H. and Longcope, D. W. (2011), 'Direct Measurements of Magnetic Twist in the Solar Corona', *Astrophys. J.* **736**, 97.

Mamajek, E. E., Prsa, A., Torres, G., Harmanec, P., Asplund, M., Bennett, P. D., Capitaine, N., Christensen-Dalsgaard, J., Depagne, E., Folkner, W. M., Haberreiter, M., Hekker, S., Hilton, J. L., Kostov, V., Kurtz, D. W., Laskar, J., Mason, B. D., Milone, E. F., Montgomery, M. M., Richards,

M. T., Schou, J. and Stewart, S. G. (2015), 'IAU 2015 Resolution B3 on Recommended Nominal Conversion Constants for Selected Solar and Planetary Properties', *ArXiv e-prints* .

Masters, A., Achilleos, N., Kivelson, M., Sergis, N., Dougherty, M., Thomsen, M., Arridge, C., Krimigis, S., McAndrews, H., Kanani, S. et al. (2010), 'Cassini observations of a Kelvin-Helmholtz vortex in Saturn's outer magnetosphere', *Journal of Geophysical Research: Space Physics* **115**(A7).

McLachlan, N. W. (1946), 'Mathieu functions and their classification', *Journal of Mathematics and Physics* **25**(1-4), 209–240.

Montmerle, T., Augereau, J.-C., Chaussidon, M., Gounelle, M., Marty, B. and Morbidelli, A. (2006), 'From Suns to Life: A Chronological Approach to the History of Life on Earth 3. Solar System Formation and Early Evolution: the First 100 Million Years', *Earth Moon and Planets* **98**, 39–95.

Möstl, U. V., Temmer, M. and Veronig, A. M. (2013), 'The Kelvin-Helmholtz Instability at Coronal Mass Ejection Boundaries in the Solar Corona: Observations and 2.5D MHD Simulations', *The Astrophysical Journal Letters* **766**, L12.

Murdin, P. (2001), *Encyclopedia of astronomy and astrophysics*.

Nakariakov, V. M., Melnikov, V. F. and Reznikova, V. E. (2003), 'Global sausage modes of coronal loops', *Astron. Astrophys.* **412**, L7–L10.

Nakariakov, V. M., Ofman, L., Deluca, E. E., Roberts, B. and Davila, J. M. (1999), 'TRACE observation of damped coronal loop oscillations: Implications for coronal heating', *Science* **285**, 862–864.

Nakariakov, V. M. and Roberts, B. (1995), 'Magnetosonic Waves in Structured Atmospheres with Steady Flows, I', *Solar Physics* **159**, 213–228.

Nakariakov, V. M. and Verwichte, E. (2005), 'Coronal Waves and Oscillations', *Living Reviews in Solar Physics* **2**.

Nisticò, G., Nakariakov, V. M. and Verwichte, E. (2013), 'Decaying and decayless transverse oscillations of a coronal loop', *Astron. Astrophys.* **552**, A57.

Ofman, L., Davila, J. M. and Steinolfson, R. S. (1994), 'Nonlinear studies of coronal heating by the resonant absorption of Alfvén waves', *Geophys. Res. Lett.* **21**, 2259–2262.

Ofman, L. and Thompson, B. J. (2011), 'SDO/AIA Observation of Kelvin-Helmholtz Instability in the Solar Corona', *The Astrophysical Journal Letters* **734**, L11.

Parker, E. N. (1958), 'Dynamics of the Interplanetary Gas and Magnetic Fields.', *Astrophys. J.* **128**, 664.

Poedts, S., Toth, G., Belien, A. J. C. and Goedbloed, J. P. (1997), 'Nonlinear MHD Simulations of Wave Dissipation in Flux Tubes', *Solar Phys.* **172**, 45–52.

Priest, E. (2014), *Magnetohydrodynamics of the Sun*.

Roberts, B. (1973), 'On the hydromagnetic stability of an unsteady Kelvin-Helmholtz flow', *Journal of Fluid Mechanics* **59**, 65–76.

Roberts, B. (1981*a*), 'Wave propagation in a magnetically structured atmosphere. I: Surface waves at a magnetic interface.', *Solar Physics* **69**, 27–38.

Roberts, B. (1981*b*), 'Wave Propagation in a Magnetically Structured Atmosphere. II: Waves in a Magnetic Slab', *Solar Physics* **69**, 39–56.

Roberts, B. and Webb, A. R. (1978), 'Vertical motions in an intense magnetic flux tube.', *Solar Phys.* **56**, 5–35.

Roberts, B. and Webb, A. R. (1979), 'Vertical Motions in an Intense Magnetic Flux Tube - Part Three - on the Slender Flux Tube Approximation', *Solar Phys.* **64**, 77–92.

Ruderman, M. S. (2007), 'Nonaxisymmetric Oscillations of Thin Twisted Magnetic Tubes', *Solar Phys.* **246**, 119–131.

Ruderman, M. S. (2015), 'Propagating kink waves in thin twisted magnetic tubes with continuous equilibrium magnetic field', *Astron. Astrophys.* **575**, A130.

Ruderman, M. S. (2017), 'Nonlinear Generation of Fluting Perturbations by Kink Mode', *Solar Phys.* **292**, 111.

Ruderman, M. S. (2018), 'Rayleigh-Taylor instability of a magnetic tangential discontinuity in the presence of oscillating gravitational acceleration', *Astron. Astrophys.* **in press**.

Ruderman, M. S. and Erdélyi, R. (2009), 'Transverse Oscillations of Coronal Loops', *Space Sci. Rev.* **149**, 199–228.

Ruderman, M. S. and Goossens, M. (2014), 'Nonlinear Kink Oscillations of Coronal Magnetic Loops', *Solar Phys.* **289**, 1999–2020.

Ruderman, M. S., Goossens, M. and Andries, J. (2010), 'Nonlinear propagating kink waves in thin magnetic tubes', *Physics of Plasmas* **17**, 082108.

Ruderman, M. S. and Roberts, B. (2002), 'The Damping of Coronal Loop Oscillations', *Astrophys. J.* **577**, 475–486.

Ruderman, M. S. and Terradas, J. (2015), 'Standing kink oscillations of thin twisted magnetic tubes with continuous equilibrium magnetic field', *Astron. Astrophys.* **580**, A57.

Ryutova, M. (2015), *Physics of Magnetic Flux Tubes.*

Ryutova, M., Berger, T., Frank, Z., Tarbell, T. and Title, A. (2010), 'Observation of Plasma Instabilities in Quiescent Prominences', *Solar Physics* **267**, 75–94.

Sakanaka, P. H. and Goedbloed, J. P. (1974), 'New approach to magnetohydrodynamic stability: II. Sigma-stable diffuse pinch configurations', *Physics of Fluids* **17**, 919–929.

Sakurai, T., Goossens, M. and Hollweg, J. V. (1991), 'Resonant Behaviour of Magnetohydrodynamic Waves on Magnetic Flux Tubes - Part One', *Solar Phys.* **133**, 227–245.

Schröder, K. P. and Connon Smith, R. (2008), 'Distant future of the Sun and Earth revisited', *Mon. Not. Roy. Astron. Soc.* **386**, 155–163.

Shafranov, V. D. (1958), 'On Magnetohydrodynamical Equilibrium Configurations', *Soviet Journal of Experimental and Theoretical Physics* **6**, 545.

Smyth, W. D. and Moum, J. N. (2012), 'Ocean Mixing by Kelvin-Helmholtz Instability', *Oceanography* **25**.

Soler, R., Terradas, J., Oliver, R., Ballester, J. L. and Goossens, M. (2010), 'Kelvin-Helmholtz Instability in Coronal Magnetic Flux Tubes due to Azimuthal Shear Flows', *The Astrophysical Journal* **712**, 875–882.

Somasundaram, K., Venkatraman, S. and Sengottuvel, M. P. (1999), ‘Hydromagnetic surface waves along compressible cylindrical flux tubes with steady flows’, *Plasma Physics and Controlled Fusion* **41**, 1421–1428.

Spiegel, E. A. and Zahn, J. P. (1992), ‘The solar tachocline.’, *Astron. Astrophys.* **265**, 106–114.

Spruit, H. C. (1981), ‘Motion of magnetic flux tubes in the solar convection zone and chromosphere.’, *Astron. Astrophys.* **98**, 155–160.

Srivastava, A. K., Zaqarashvili, T. V., Uddin, W., Dwivedi, B. N. and Kumar, P. (2008), ‘Observation of multiple sausage oscillations in cool post-flare loop’, *Mon. Not. Roy. Astron. Soc.* **388**, 1899–1903.

Syrovatskii, S. (1957), ‘Magnetic hydrodynamics (in russian)’, *Uspekhi Fiz. Nauk* **62**(7), 247–303.

Taroyan, Y. and Erdélyi, R. (2002), ‘Resonant and Kelvin-Helmholtz instabilities on the magnetopause’, *Physics of Plasmas* **9**, 3121–3129.

Taroyan, Y. and Ruderman, M. S. (2011), ‘Mhd waves and instabilities in space plasma flows’, *Space Science Reviews* **158**(2), 505–523.

Terra-Homem, M., Erdélyi, R. and Ballai, I. (2003), ‘Linear and non-linear MHD wave propagation in steady-state magnetic cylinders’, *Solar Physics* **217**, 199–223.

Terradas, J., Andries, J., Goossens, M., Arregui, I., Oliver, R. and Ballester, J. L. (2008), ‘Nonlinear Instability of Kink Oscillations due to Shear Motions’, *Astrophys. J. Lett.* **687**, L115.

Terradas, J., Magyar, N. and Doorsselaere, T. V. (2018), ‘Effect of magnetic twist on nonlinear transverse kink oscillations of line-tied magnetic flux tubes’, *The Astrophysical Journal* **853**(1), 35.

Terradas, J. and Ofman, L. (2004), ‘Loop Density Enhancement by Nonlinear Magnetohydrodynamic Waves’, *Astrophys. J.* **610**, 523–531.

Thomson, W. (1871), ‘Hydrokinetic solutions and observations’, *The London, Edinburgh, and Dublin Philosophical Magazine and Journal of Science* **42**(281), 362–377.

Tirry, W. J., Cadez, V. M., Erdelyi, R. and Goossens, M. (1998), 'Resonant flow instability of MHD surface waves', *Astronomy and Astrophysics* **332**, 786–794.

Van Doorsselaere, T., Andries, J., Poedts, S. and Goossens, M. (2004), 'Damping of Coronal Loop Oscillations: Calculation of Resonantly Damped Kink Oscillations of One-dimensional Nonuniform Loops', *Astrophys. J.* **606**, 1223–1232.

Vasheghani Farahani, S., Nakariakov, V. M. and van Doorsselaere, T. (2010), 'Long-wavelength torsional modes of solar coronal plasma structures', *Astron. Astrophys.* **517**, A29.

Vernazza, J. E., Avrett, E. H. and Loeser, R. (1981), 'Structure of the solar chromosphere. III. Models of the EUV brightness components of the quiet sun.', *The Astrophysical Journal Supplement Series* **45**, 635–725.

Vietri, M., Ferrara, A. and Miniati, F. (1997), 'The survival of interstellar clouds against Kelvin-Helmholtz instabilities', *The Astrophysical Journal* **483**(1), 262.

von Helmholtz, H. (1868), *Über discontinuirliche Flüssigkeits-Bewegungen*, Monatsberichte der Königlichen Preussische Akademie der Wissenschaften zu Berlin.

Wang, C.-Y. and Chevalier, R. A. (2001), 'Instabilities and clumping in type ia supernova remnants', *The Astrophysical Journal* **549**(2), 1119.

Wentzel, D. G. (1979), 'Hydromagnetic surface waves on cylindrical fluxtubes.', *Astron. Astrophys.* **76**, 20–23.

Williamson, A. and Erdélyi, R. (2014), 'Resonant damping of propagating kink waves in time-dependent magnetic flux tube', *Solar Physics* **289**(11), 4105–4115.

Wilson, P. R. (1978), 'Wave modes in a magnetic flux sheath.', *Astrophys. J.* **221**, 672–676.

Wilson, P. R. (1979), 'Hydromagnetic wave modes in magnetic flux tubes.', *Astron. Astrophys.* **71**, 9–13.

Yi, S., Demarque, P., Kim, Y.-C., Lee, Y.-W., Ree, C. H., Lejeune, T. and Barnes, S. (2001), 'Toward Better Age Estimates for Stellar Populations: The Y¡SUP¿2¡/SUP¿ Isochrones for Solar Mixture', *The Astrophysical Journal Supplement Series* **136**, 417–437.

Zaqarashvili, T. V. (2000), 'Parametric resonance in ideal magnetohydrodynamics', *Phys. Rev. E* **62**, 2745–2753.

Zaqarashvili, T. V., Díaz, A. J., Oliver, R. and Ballester, J. L. (2010), 'Instability of twisted magnetic tubes with axial mass flows', *Astron. Astrophys.* **516**, A84.

Zaqarashvili, T. V., Oliver, R. and Ballester, J. L. (2002), 'Parametric Amplification of Magnetosonic Waves by an External, Transversal, Periodic Action', *Astrophys. J.* **569**, 519–530.

Zaqarashvili, T. V., Oliver, R. and Ballester, J. L. (2005), 'Parametric excitation of slow magnetoacoustic waves in the solar corona due to photospheric periodic motions', *Astron. Astrophys.* **433**, 357–364.

Zaqarashvili, T. V., Vörös, Z., Narita, Y. and Bruno, R. (2014), 'Twisted Magnetic Flux Tubes in the Solar Wind', *Astrophys. J.* **783**, L19.

Zaqarashvili, T. V., Vörös, Z. and Zhelyazkov, I. (2014), 'Kelvin-Helmholtz instability of twisted magnetic flux tubes in the solar wind', *Astron. Astrophys.* **561**, A62.

Zaqarashvili, T. V., Zhelyazkov, I. and Ofman, L. (2015), 'Stability of Rotating Magnetized Jets in the Solar Atmosphere. I. Kelvin-Helmholtz Instability', *Astrophys. J.* **813**, 123.

Zeilik, M. and Gregory, S. (1998), *Introductory Astronomy and Astrophysics.*

Zhelyazkov, I. (2015), 'On Modeling the Kelvin-Helmholtz Instability in Solar Atmosphere', *Journal of Astrophysics and Astronomy* **36**, 233–254.

Zhelyazkov, I., Zaqarashvili, T., Ofman, L. and Chandra, R. (2018), 'Kelvin–helmholtz instability in a twisting solar polar coronal hole jet observed by sdo/aia', *Advances in Space Research* **61**(2), 628 – 638. MHD Wave Phenomena in the Solar Interior and Atmosphere.

Zhelyazkov, I. and Zaqarashvili, T. V. (2012), 'Kelvin-Helmholtz instability of kink waves in photospheric twisted flux tubes', *Astron. Astrophys.* **547**, A14.

Zsámberger, N. K., Allcock, M. and Erdélyi, R. (2018), 'Magneto-acoustic Waves in a Magnetic Slab Embedded in an Asymmetric Magnetic Environment: The Effects of Asymmetry', *Astrophys. J.* **853**, 136.